DEVELOPMENT OF MATERIAL FLOW STRESS AND DAMAGE MODELS FOR 304 STAINLESS STEEL

A Thesis Submitted to
The Graduate School of
İzmir Institute of Technology
in Partial Fulfillment of the Requirements for the Degree of

MASTER OF SCIENCE

in Mechanical Engineering

by
İbrahim Berk AKDOĞAN

December 2024
İZMİR

We approve the thesis of **İbrahim Berk AKDOĞAN**

Examining Committee Members:

_____

Prof. Dr. Mustafa GÜDEN

Department of Mechanical Engineering, Izmir Institute of Technology

_____

Prof. Dr. Hasan YILDIZ

Department of Mechanical Engineering, Ege University

_____

Assist. Prof. Dr. Benay UZER YILMAZ

Department of Mechanical Engineering, Izmir Institute of Technology

11 December 2024

_____

Prof. Dr. Mustafa GÜDEN

Supervisor, Department of
Mechanical Engineering İzmir
Institute of Technology

_____   _____

Prof. Dr. M.İ. Can DEDE   **Prof. Dr. Mehtap EANES**

Head of the Department of   Dean of the Graduate School
Mechanical Engineering

ACKNOWLEDGEMENTS

ABSTRACT

DEVELOPMENT OF MATERIAL FLOW STRESS AND DAMAGE MODELS FOR 304 STAINLESS STEEL

Previous experimental and numerical studies on stainless steel (SS) 304 alloy have been mostly focused on the determination of the flow stress behaviour as function of the volume fraction of martensite. The failure behaviour of the alloy is equally important in the impact related applications. No systematic studies have been yet performed on the determination of the damage models of SS 304 alloy in order to simulate its dynamic loading behaviour. In this thesis, the parameters of the Johnson and Cook (JC) flow stress and JC damage equations were experimentally determined for an SS 304 alloy. The determined parameters were then verified and also calibrated by modelling the experimental tests used to extract these parameters. The numerical models were implemented in LS-Dyna. The experimental ballistics tests performed at 800 m s^{-1} on B4C coated and uncoated SS 304 plates were further simulated in Ls-Dyna using the determined model parameters. Finally, the microscopic studies have clearly indicated the martensitic transformation in the tested alloy and adiabatic heat at high strain rates reduced the extent of the martensite formation. Finally, the fraction of martensite was predicted analytically at different strain rates using the equations from the literature.

Keywords: MLR Correction, SS 304, Mechanical Properties, Johnson-Cook Strength Model, Johnson-Cook Damage Model, SHTB, Martensitic Transformation

ÖZET

304 PASLANMAZ ÇELİĞİ İÇİN AKMA GERİLME VE HASAR MODELLERİN GELİŞTİRİLMESİ

Paslanmaz çelik 304 alaşımı üzerine yapılan önceki deneysel ve sayısal çalışmalar çoğunlukla martensitin hacim kesrine bağlı akış gerilimi davranışının belirlenmesine odaklanmıştır. Alaşımın hasar davranışı darbe ile ilgili uygulamalarda eşit derecede önemlidir. SS 304 alaşımının dinamik yükleme davranışını simüle etmek amacıyla hasar modellerinin belirlenmesi konusunda henüz sistematik bir çalışma yapılmamıştır. Bu tezde, Johnson ve Cook (JC) akış gerilimi ve JC hasar denklemlerinin parametreleri bir paslanmaz çelik 304 alaşımı için deneysel olarak belirlenmiştir. Belirlenen parametreler daha sonra bu parametreleri çıkarmak için kullanılan deneysel testlerin modellenmesiyle doğrulanmış ve kalibre edilmiştir. Sayısal modeller LS-Dyna'da uygulanmıştır. B_4C kaplı ve kaplanmamış SS 304 plakalar üzerinde 800 m s^{-1}'de gerçekleştirilen deneysel balistik testler, belirlenen model parametreleri kullanılarak Ls-Dyna'da simüle edilmiştir. Son olarak, mikroskobik çalışmalar test edilen alaşımdaki martensitik dönüşümün ve yüksek gerinim oranlarındaki adiabatik ısının martensit oluşumunun kapsamını azalttığını açıkça göstermiştir. Son olarak, martensit fraksiyonu literatürdeki denklemler kullanılarak farklı gerinim oranlarında analitik olarak tahmin edilmiştir.

Anahtar Kelimeler: MLR Düzeltmesi, SS 304, Mekanik Özellikler, Johnson-Cook Mukavemet Modeli, Johnson-Cook Hasar Modeli, SHTB, Martensitik Dönüşüm

TABLE OF CONTENTS

LIST OF FIGURES

LIST OF TABLES

CHAPTER 1

INTRODUCTION

Stainless steel (SS) 304, known as 18/8 steel, is an austenitic steel, comprised of 18% chromium and 8% nickel at minimum. Other major alloying elements include carbon, manganese and silicon and small amounts of phosphorous and sulphur. Stainless steel 304 has an excellent corrosion resistance, making it one of the most preferred alloys for the application in which the corrosion resistance is a primary design criterion including the aviation, automotive and food industries. The crystal structure of SS 304 at room temperature is austenite γ(fcc), stabilized by nickel (8%). During plastic deformation, the austenitic phase undergoes a transformation into the martensitic α' phase (bcc), a phenomenon termed transformation-induced plasticity (TRIP). The degree of martensitic transformation is contingent upon factors such as chemical composition, imposed strain, strain rate, and thermal conditions. TRIP steels characteristically exhibit an elevated strain hardening rate, attributable to the embedding of a robust martensitic phase within the austenite matrix. The martensitic phase fraction also increases with increasing plastic strain. TRIP steels are also characterized with their exceptional high ductility. The relatively high ductility is due to delayed necking (necking occurs at relatively high strains), caused by the martensitic transformation. A high ductility combined with a high strength (hence a high toughness) makes TRIP steels potentially suitable for the impact load mitigation applications including armours that absorb the incoming energy of a bullet by the plastic deformation. Both high strength and high ductility in these applications contribute much to the energy absorption capability of armours.

In finite element (FE) models of plastic deformation, material deformation and failure behaviour are described by the material constitutive equations that are generally function of strain, strain rate and temperature. The Johnson-Cook (JC) flow stress and the JC failure strain/damage equations are among the most widely used flow stress and failure models for metallic alloys in the FE simulations of plastic deformation. Modelling the deformation of SS 304 and also other TRIP steels using the JC flow stress and failure equations are, however, seen to be problematic due to the following reason(s). It is well known that the extent of martensitic transformation is temperature dependent; that is, the

fraction of martensitic transformation decreases as the temperature increases or vice versa. At increasingly high deformation rates, a metallic alloy test specimen is heated, because the fast deformation prevents the heat dissipation from tested specimen. This phenomenon is called adiabatic heating, which is a well-known effect of high strain rate deformation. Hence, strain rate and temperature are coupled in the high strain rate deformation. Increasing strain rate, although, increases the flow stress due to the strain rate sensitive flow stress, adiabatic heating has a reverse effect, resulting in a thermal softening. Additionally, the increased temperature at high strain rates may result in a reduced extent of martensite transformation. The combined effect of both, that are the thermal softening and the reduced extend of martensite transformation, is that the flow stress at high strain rates becomes smaller than those at quasi-static strain rates at an earlier plastic strain than in the case of merely the adiabatic heating effect. This naturally makes it difficult to determine the strain rate sensitivity parameter of the JC flow stress and failure strain equation.

In this thesis, the parameters of the JC flow stress and JC damage equations were experimentally determined for an SS 304. The determined parameters were then verified and also calibrated by modelling the experimental tests used to extract these parameters. In the content of the thesis, two different groups of experimental tests were conducted. Quasi-static tensile experiments were executed at strain rates of 10^{-3}, 10^{-2} and 10^{-1} s^{-1}, while dynamic high-strain-rate tensile tests were carried out utilizing a Split Hopkinson Tension Bar (SHTB) apparatus at rates of 2100 and 2900 s^{-1}.

The numerical models of quasi-static and high strain rate tension tests were implemented in LS-Dyna. Finally, the experimental ballistic tests performed at 800 m s^{-1} on B$_4$C coated and uncoated SS 304 plates were also simulated in Ls-Dyna using the determined model parameters.

The contributions of the present thesis to current literature are as follows. Although, there have been many experimental studies on the quasi-static and high strain rate deformation behaviour and the flow stress equations of SS 304 alloy in the literature, no systematic studies have performed yet on the failure strain equations to simulate the damaging during dynamic loading. This study is, therefore, fill a gap in this field by providing the JC damage equation parameters for an SS 304 alloy.

CHAPTER 2

BACKGROUND

2.1. Literature Survey on the Deformation Behaviour of SS 304

The initiation of strain-induced martensitic transformation is intricately linked to the stacking fault energy (SFE). In FCC crystalline structures, stacking faults emerge due to the dissociation of a/2<110> full dislocations into leading and trailing Shockley partial dislocations a/6<211>, where a represents the lattice parameter. A reduced SFE value results in a significant spatial separation between the Shockley partials, impeding dislocation glide and thereby facilitating martensitic transformation. The reported SFE ranges for stainless steels are >45 mJ m^{-2} for dislocation slip, 20–45 mJ m^{-2} for twinning, and <20 mJ m^{-2} for martensitic transformation[2].

As previously highlighted, twin-induced plasticity (TWIP) supplants martensitic transformation at moderate stacking fault energies (SFEs). It has been demonstrated that SFE is inherently dependent on the alloy's chemical composition; the incorporation of elements such as cobalt, chromium, and molybdenum into nickel reduces the SFE of stainless steel alloys by approximately 1.8 mJ m^{-2} per at.%.[3] .

Martensitic transformation has been proposed to occur by two shearing processes (Figures 2.1(a) and (b)), known as the Bogers–Burgers–Olson–Cohen theory[4] [5-7]. A shear of T/3 slip on each $(11\bar{1})$ plane and a shear of 3T/8 slip on each (111) plane as seen in Figure 2.1(a) create an intersection when viewed in $[1\,\bar{1}\,0]$ direction as depicted in Figure 2.1(b). At the intersection of two ε-plates (hcp), α' (bcc) martensite phase is formed. Figure 2.1(c) presents a micrograph illustrating the emergence of α' martensite needles originating from ε-plates. In addition to shear band intersections, mechanical twins and densely packed arrays of stacking faults have been posited as critical loci for the nucleation of strain-induced martensite. The fraction of the martensitic transformation can be measured either by the Rietveld method on the XRD spectral analysis[3, 8], or using a Ferritescope[9] or through image analysis[10]. Figure 2.2 and Figure 2.3 show the microstructure and the XRD spectrum of a strained SS 304 specimen at a temperature of -50ºC. The intersections of ε-plate are the locations of α'-martensite as seen in Figure

2.2. The XRD spectrum of Figure 2.3 proves the presence of both phases, ε and α′, in the γ structure.
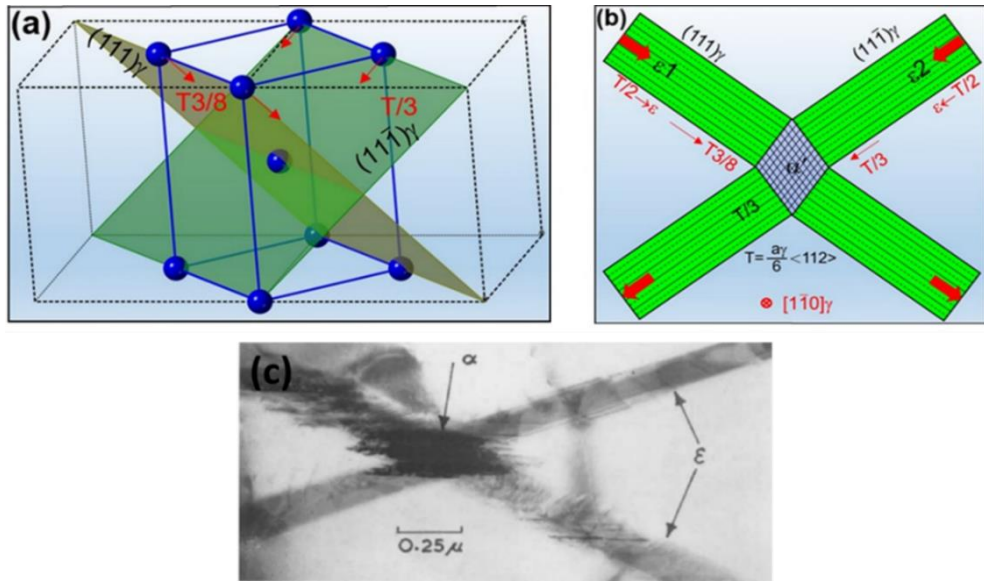
Figure 2.1. The schematic of the Bogers–Burgers–Olson–Cohen mode of γ(fcc) →ε(hcp) → α′(bcc) (a) T/3 shear on (11$\bar{1}$) plane and 3T/8 shear on (111) plane, (b) a view along [1$\bar{1}$0] and martensite formation occurs at the juncture where two ε-plates converge[11] and (c) the micrograph showing the formation of α′ martensite needles from ε-plates

(Source: Venables [12])
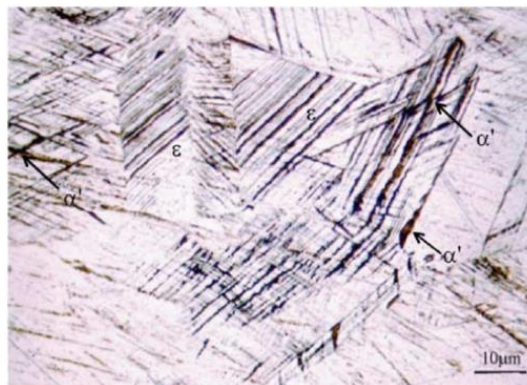
Figure 2.2. The microstructure of a coarse-grained SS 304 specimen strained to 10% at -50oC, showing ε(hcp)-plates and α′-martensite

(Source: De [13])

4
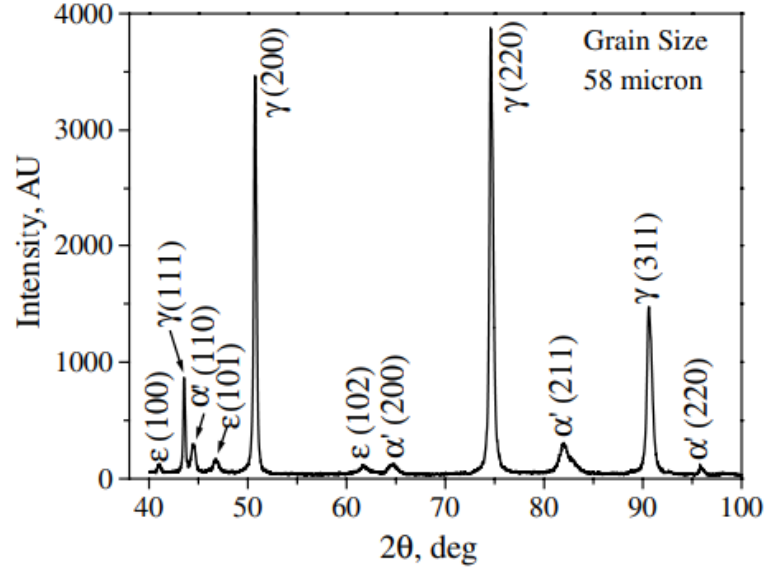
Figure 2.3.The XRD spectrum of the strained specimen at -50oC, showing the peaks of
ε(hcp), α′ (martensite) and γ (austenite)

(Source: De [13])

Olson and Cohen[14] proposed (1975) an equation for the volume fraction of martensitic transformation ($f^{\alpha'}$) in the total volume of alloy. The equation defines the volume fraction of plastically induced martensite as a function of plastic strain, incorporating the mechanics of shear-band formation, the likelihood of shear-band intersections, and the conditional probability of such intersections initiating a martensitic transformation. This equation is known as the Olson-Cohen Model[14] and based on the following relation

$$\frac{df^{\alpha'}}{(1-f^{\alpha'})} = \bar{v}^{\alpha'}dN_v^{\alpha'} \tag{2.1}$$

In above equation, $\bar{v}^{\alpha'}$ is the average volume of per martensite and $dN_v^{\alpha'}$ is the number of martensitic nuclei produced per unit volume of austenite. By integrating Equation 2.1, the evolution of the martensite volume fraction as a function of plastic strain. is obtained as

$$f^{\alpha'} = 1 - e^{\left\{-\beta\left[1-e^{(-\alpha\varepsilon)}\right]^n\right\}} \tag{2.2}$$

5

where, α and β are the temperature dependent constants; n is the temperature independent constant (~2 or higher) and ε is the applied strain. The value of β is

$$\beta = \frac{\bar{v}^{\alpha\prime} K}{(\bar{v}^{sb})^n} p \qquad (2.3)$$

Here, $\bar{v}^{sb}$ represents the mean volume per shear band, K is a geometric constant associated with shear band morphology, and p denotes the probability of a shear band inducing martensitic nucleation, which is governed by the chemical driving force. The parameter α in Equation 2.2 defines the shear band formation with strain and it is temperature dependent through SFE. The parameter β is related to the probability that is temperature dependent through chemical driving force. Equation 2.2 was fitted with experimental data on an SS 304 and the result is shown in Figure 2.4. As is seen in the same figure, Equation 2.2 exhibits a sigmoidal profile, with the martensite volume fraction asymptotically approaching a saturation threshold that remains below 100%. It is also noted in the same graph that the saturation fraction increases as the temperature decreases. Lower deformation temperatures result in higher volume fractions of martensite.
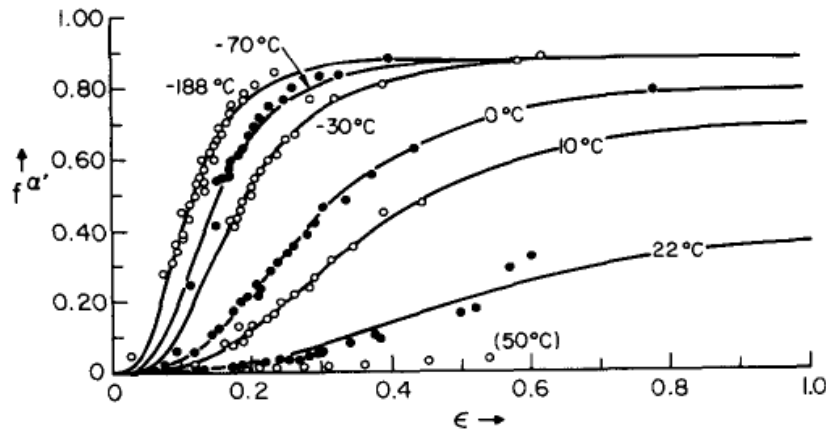
Figure 2.4. The experimental and fitted (Equation 2.2) martensite volume fraction ($f^{\alpha\prime}$) of an SS 304 alloy as function of strain at different temperatures
(Source: Olson and Cohen[14])

6

The effects of strain state and strain rate on the strain-induced transformation in an SS 304 sheet tensile loaded uniaxially and biaxially at a quasi-static (10^{-3} s^{-1}) and a high strain (10^3 s^{-1}) rate were investigated by Hecker et al.[9]. The reported true stress-true strain curves at four different temperatures are shown in Figure 2.5(a). As seen in the same figure, the strain-induced $\gamma \rightarrow \alpha'$ transformation enhances the strain hardening rate at -15°C and -80°C, while reducing the elongation to failure. It was proposed that the saturation of martensite formation at larger strains resulted in an earlier failure at -15°C and -80°C due to the decreased strain hardening rate. Figure 2.5(b) shows the variation of the volume fraction of martensite with strain in uniaxial tension tests at 10^{-3} s^{-1} and 10^3 s^{-1} in the same study. At low strains, the formation of α' is seen to be higher in the high strain rate test (10^3 s^{-1}) than in the low strain rate test (10^{-3} s^{-1}). However, the adiabatic heating in the high strain rate test reduces the formation of α' after about 0.25 strain. The volume fraction of martensitic transformation in the high strain rate test becomes, therefore, smaller than that in the quasi-static strain rate test after about 0.25 strain.
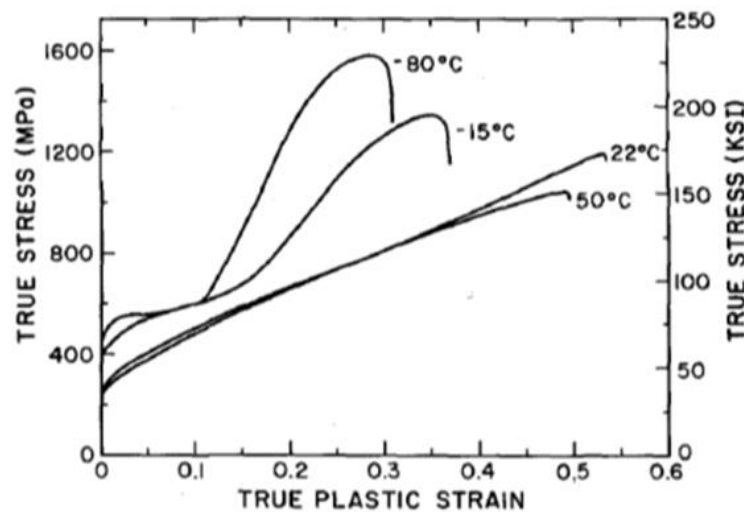
(a)

(cont. on the next page)

Figure 2.5. (a)true stress-true strain curves at four different temperatures at 10^{-3} s^{-1} and (b) the variation of the volume fraction of martensite with strain in uniaxial tension test at 10^{-3} and 10^3 s^{-1} in an SS 304

(Source: Murr et al. [15])
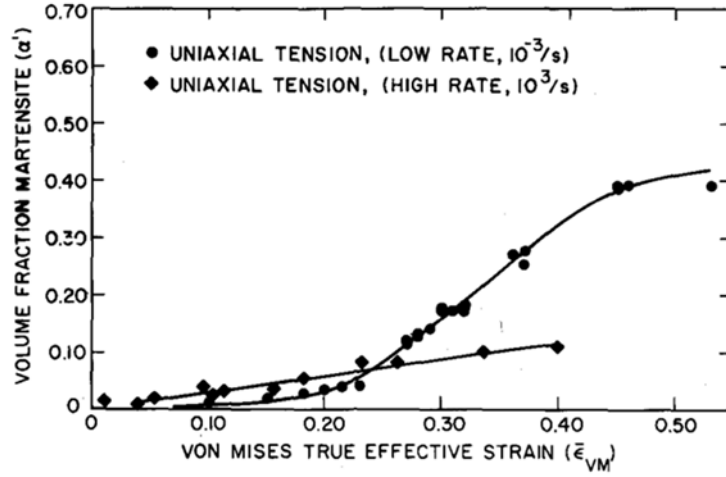
(b)

Figure 2.5 (cont.)

A following microscopic study[15] on the quasi-statically and dynamically tested specimens showed that α' martensite was nucleated at the certain region of the intersections of shear bands which was consisted of stacking faults, twins and ε-plates. In the high strain rate tested specimen, a large volume fraction of α' was observed at low strains while adiabatic heating prevented the further transformation at larger strains, agreeing with the experimentally measured volume fractions of martensitic transformation.

Ramirez et al.[16] determined the flow strength of an SS 304 at room temperature by considering the structure composing of two different phases, austenite and martensite, and by taking into account the stress and strain (deformation energy) of each phase. Compression tests were also performed in the same study at different temperatures in order to determine the martensite volume fraction ($V_{fm} = f^{\alpha'}$) and the ratio of martensite volume fraction to austenite volume fraction $\left(V_{fam} = \dfrac{V_{fm}}{V_{fa}}\right)$, as depicted in Figures 2.6(a) and (b), respectively. The following flow stress equation was proposed in the same study to represent the flow stress of SS3 304 as function of strain

$$\sigma_t = V_{fa}\sigma_a V_{fa}^{-\gamma}\left\{\gamma\left[BV_{fm} + \frac{\varepsilon \ln(V_{fa})}{(\gamma_b + \varepsilon)} + 1\right]\right\} + \cdots$$

$$V_{fm}\sigma_m V_{fm}^{\alpha}\left\{\alpha\left[BV_{fm} + \frac{\varepsilon\alpha_n \ln(V_{fm})}{(\alpha_b + \varepsilon)} + 1\right]\right\} \quad (2.4)$$

8

where σ is the stress, a, m and t refer sequentially to austenite, martensite and total and $B, \gamma, \gamma_b, \alpha$ and α_b are the constants. It should be emphasized here that above equation differs from the rule of mixture formulations in the composite mechanics in that it takes into account the change of $\frac{V_{fm}}{V_{fa}}$ with strain (see Figure 2.6(b)).
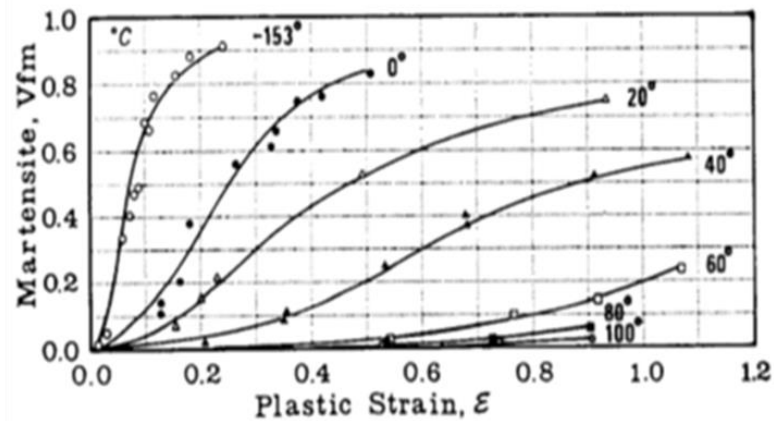
(a)
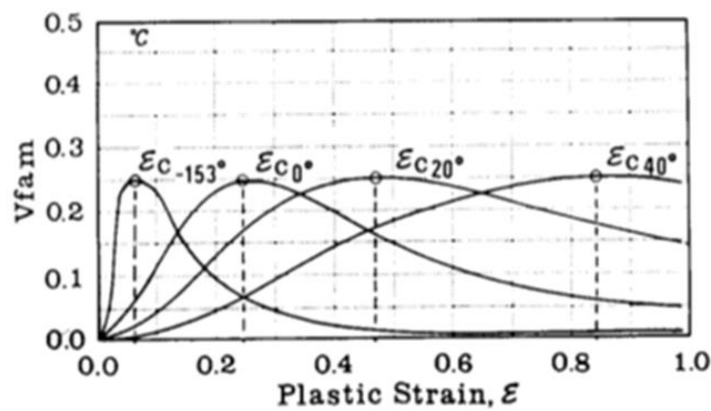
(b)

Figure 2.6. (a)martensite volume fraction (V_{fm}) and (b) the variation of the ratio of martensite volume fraction to austenite volume fraction $\left(V_{fam} = \frac{V_{fm}}{V_{fa}}\right)$ with plastic strain in an SS 304

(Source: Ramirez et al. [16])

Stringfellow et al.[17] proposed a constitutive model, composing of two equations. These are the formulation for the martensite transformation volume fraction and the formulation for the flow stress of the composite of austenite and martensite. In this study, the Olson-Cohen model for martensite volume fraction was generalized by incorporating a stress state parameter, expressed as.

$$\frac{df^{\alpha'}}{(1-f^{\alpha'})} = A_f \dot{\gamma}_a + B_f d\Sigma \tag{2.5}$$

In above equation, Σ stands for the stress triaxiality; A_f and B_f are the strain and temperature dependent parameters, B_f is also function of the state of stress, and $\dot{\gamma}_a$ is the shear strain rate. The model's predictions were subsequently validated against previously available experimental data for austenitic steels.

Tomita and Iwamota[18] extended the Stringfellow et al[17] model (given above) and proposed a constitutive model known as TI Model that can predict the deformation behaviour of SS 304 alloy under varying strain rates. The starting equation in the IT model is

$$df^{\alpha'} = A(1-f^{\alpha'})\bar{\dot{\varepsilon}}_a^{pslip} \tag{2.6}$$

where,

$$A = \alpha n \beta \, (f^{sb})^{n-1} \, (1 - f^{sb}) \tag{2.7}$$

$$\alpha = (\alpha_1 T^2 + \alpha_2 T + \alpha_3) \left(\frac{\bar{\dot{\varepsilon}}_a^{pslip}}{\dot{\varepsilon}_y} \right)^M \tag{2.8}$$

$$\beta = \frac{\eta}{\sqrt{2\pi}\sigma_g} \int_{-\infty}^{g} e^{\left\{ -\frac{(g'-g_o)^2}{2\sigma_g^2} \right\}} dg' \tag{2.9}$$

$$g = -T + g_1 \Sigma \tag{2.10}$$
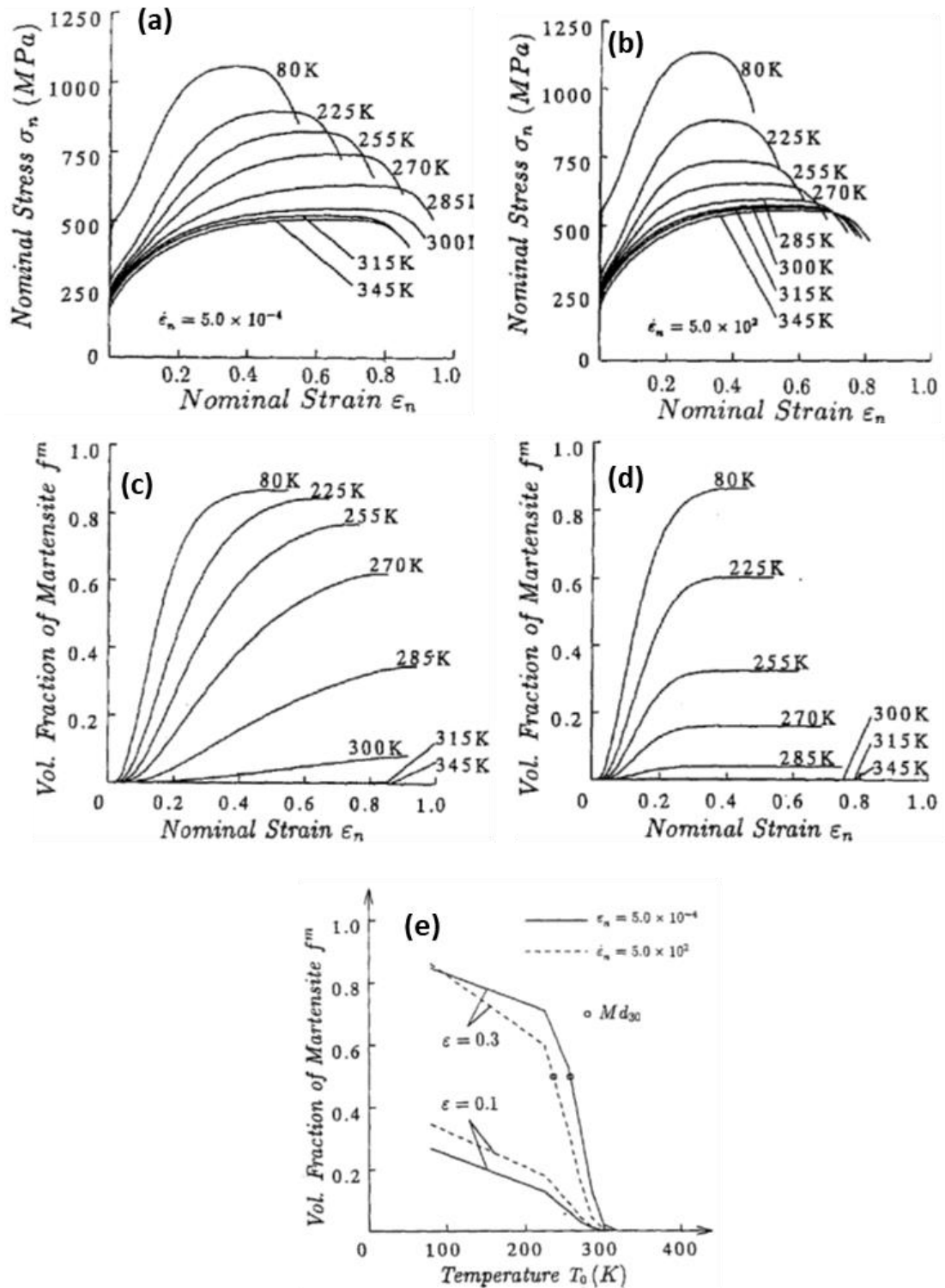
Figure 2.7. Nominal stress-strain curves of an SS 304 at (a)5×10^{-4} s^{-1} and (b)5×10^4 s^{-1}, the volume fraction of martensite vs. strain at (c)5×10^{-4} s^{-1} and (d)5×10^4 s^{-1} and (e) the volume fraction of martensite vs. temperature at 0.1 and 0.3 strain (Source: Tomita and Iwamoto[18])

In the aforementioned equations, $\bar{\dot{\varepsilon}}_a{}^{pslip}$ denotes the strain rate; β signifies the likelihood of a shear band intersection initiating martensitic nucleation, and n, a geometric parameter, holds a value of 4.5; f^{sb} represents the volume fraction of shear bands; M corresponds to the strain rate sensitivity exponent. σ_g is the standard deviation, g_o denotes the mean transformation driving force; g_1 is a constant; $\dot{\varepsilon}_y$ is the reference strain rate; η is a geometric constant, and T represents temperature. Finite element numerical simulations were executed using the proposed constitutive framework in conjunction with a differential heat conduction equation, presuming that 90% of the deformation energy is dissipated as heat. The results of the FE analysis on the deformation behaviour of an SS 304 at a lower strain rate of 5×10^{-4} s^{-1} and a higher strain rate of 5×10^{4} s^{-1} are shown in Figures 2.7(a-e). Followings were concluded in the same study based on the graphs in in the figures. At the lowest temperature (80K), a large saturation value of martensite (0.85) was seen at the lower strain rate (Figure 2.7(c)) and at the higher strain rate (Figure 2.7(d)) while the saturation values at the higher strain rate decreased more rapidly than those at the lower strain rate at increasing temperatures due to the adiabatic heating effect at high strain rates. Since the martensite volume fraction decreased more rapidly in the higher strain rate as the temperature increased, the higher strain rate test necking strains (Figure 2.7(b)) also decreased more rapidly than the lower strain rate necking strains (Figure 2.7(a)). At a low strain (0.1), the higher strain rate promoted a higher volume fraction of martensite formation while the lower strain rate induced a higher volume fraction of martensite formation at a larger strain (0.3) as seen in Figure 2.7(e).

Iwamoto et al. [19] modified above IT model by including an additional parameter $\alpha_4\Sigma$ into Equation 2.8 (α) as

$$\alpha = (\alpha_1 T^2 + \alpha_2 T + \alpha_3 - \alpha_4\Sigma)\left(\frac{\bar{\dot{\varepsilon}}_a{}^{pslip}}{\dot{\varepsilon}_y}\right)^M \qquad (2.11)$$

This additional term differentiates the tension and compression deformation behaviour from each other by taking $\Sigma = 1/3$ for tension and $\Sigma = -1/3$ for compression. The experimental tension and compression tests on an SS 304 alloy showed that the compression flow stresses were higher than the tension flow stresses at low strains and temperatures (Figure 2.8(a)). However, the tension flow stresses increased over the compression flow stresses at increasing strains (Figure 2.8(a)). The measured volume

12

fractions of martensite as function of strain were also confirmed these results (Figure 2.8(b)). The modified model for compression was also shown to match with the measured volume fractions of martensite at different temperatures as depicted in Figure 2.8(c). The detected asymmetry between the compression and tension stress-strain behaviour was further ascribed to the deformation-induced anisotropy.
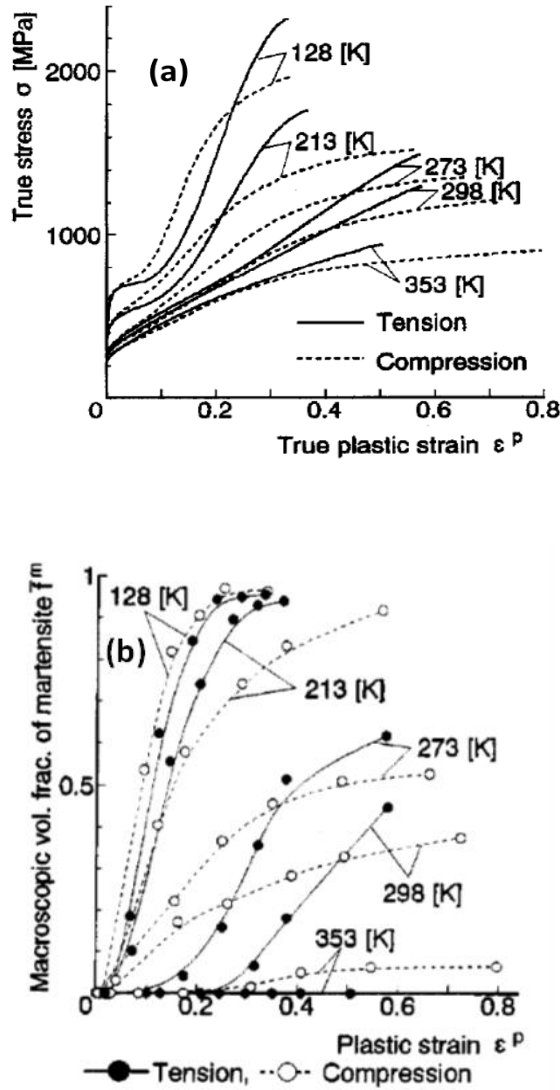
Figure 2.8. (a) experimental true stress-strain curves under tension and compression and the volume fraction of martensite vs. strain, (b) experimental (c) experimental and model at 5×10^{-4} s^{-1}

(Source: Tomita and Iwamoto [18])

13
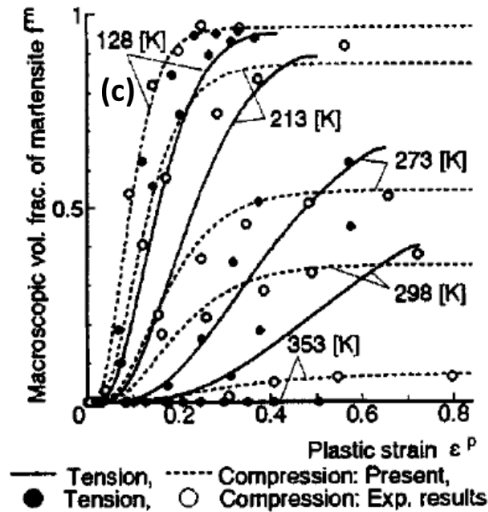
Figure 2.8 (cont.)

Diana and Parks[20] modelled the volume fraction of martensite in a polycrystalline steel under thermomechanical loading. The model's foundational premise posited that martensitic nucleation within a grain occurred at the confluence points of shear bands engendered by the movement of twelve partial dislocations traversing the $\{111\}\langle\bar{2}11\rangle$ slip plane. A numerical computation, adapted from the established Taylor framework, was executed upon a polycrystalline aggregate with the objective of quantifying the shear band intensity, thereby enabling the determination of the martensitic volume fraction within each constituent grain. The model exhibited a high degree of congruency with a diverse array of empirical findings, primarily garnered from investigations conducted on 293L stainless steel. Song et al.[21] undertook an in-depth examination of the martensitic transformation under conditions of elevated strain rates. Concurrently, a correlative relationship was established within the framework of the study, incorporating strain, stress, strain rate, transformation rate, and the modified Bodner-Partom constitutive equation. Employing a one-dimensional analytical approach, the model successfully forecasted the deformation characteristics of SS 304 subjected to conditions of extreme strain rates. It was shown that the martensite volume fraction decreased with increasing strain rate.

Dan et al.[22] extended the Stringfellow et al.[17] and Iwamoto et al. [19] models by considering the nucleation site probability as a function of not just stress state, strain, and temperature, but also strain rate (with shear band intersections reduced through adiabatic

14

heating). A mixed hardening law with four phases (retained austenite, bainite, ferrite and martensite) was implemented into ABAQUS/UMAT for the tensile deformation analysis. The stress-strain curves of an SS 304 alloy were obtained at the strain rates between 1×10^{-3} and 0.1 s^{-1} to identify the simulation results based on the new constitutive model. The extended model predicted the temperature increase during deformation with strain rate, and the martensite transformation at different strain rates.
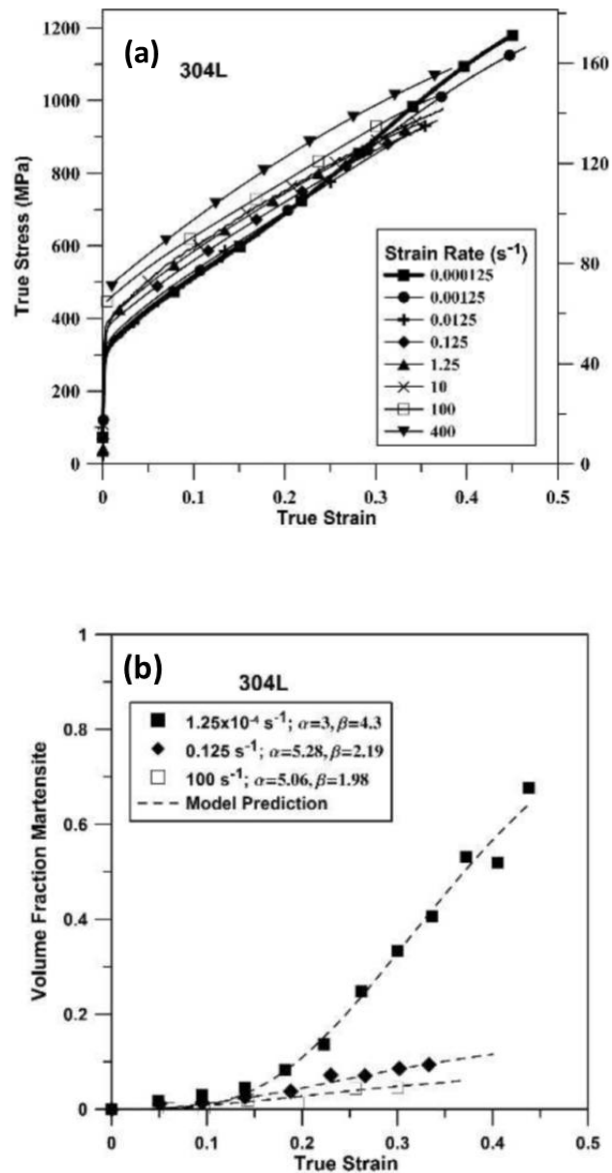
Figure 2.9. (a) experimental true stress-strain curves under tension at different strain rates (room temperature) and (b) the predicted variation of the volume fraction of martensite with strain

(Source: Lichtenfeld et al. [23])

15

The effect of strain rate on the tensile stress-strain behaviour of an SS 304L was investigated between 1.25×10^{-4} s^{-1} to 400 s^{-1} by Lichtenfeld et al.[23]. As with the previous studies, the low strain rate tensile test stresses were found to be higher than the high strain rate test stresses at large strains (Figure 2.9(a)). The martensite volume fraction was predicted at different strain rates by using the Olson-Cohen Model[14], taking the *n* value 4.5 and using the experimentally determined *α* and *β* values. The prediction is shown in Figure 2.9(b) together with the experimental results. The model, as is seen in the same figure, well predicts the experimental martensite volume fractions at different strain rates.

Talonen et al.[24] studied the relationship between the SFE, shear band formation and martensite transformation in an SS 304 alloy. The SFE was measured by the XRD and the martensite volume fraction was measured using a Ferritescope. In the same study, no shear band formation was microscopically observed at 0.05 strain (Figure 2.10(a)), parallel shear bands were observed at 0.09 strain (Figure 2.10(b)), shear band intersections were seen at increasing strains, 0.2 and 0.42 (Figure 2.10 (c) and (d)). As depicted in Figure 2.111(a), although the martensite volume fraction increased as the strain rate increased from 3×10^{-4} to 200 s^{-1} at low strains, a higher martensite volume fraction was found at the lowest strain rate of 3×10^{-4} s^{-1} at increasing strains. Furthermore, the volume fraction at which the martensite formation saturated increased as the test temperature decreased (Figure 2.11(b)).
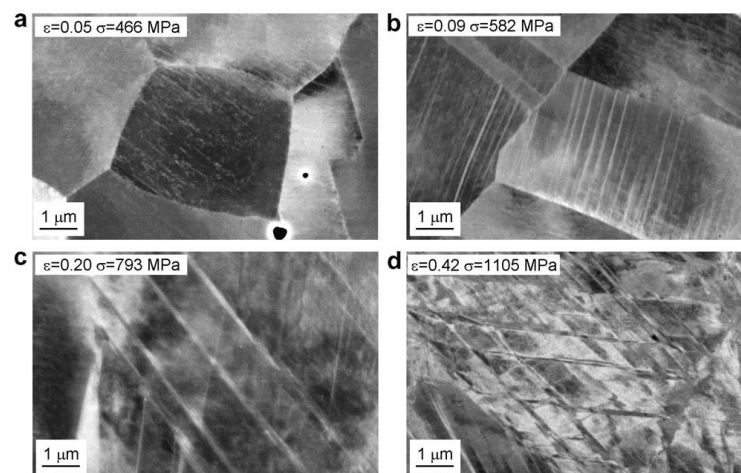
Figure 2.10. The SEM microstructure of an SS 304 alloy deformed till (a) 0.05, (b) 0.09, (c) 0.2 and (d) 0.42 at 3×10^{-4} s^{-1} and room temperature
(Source: Talonen and Hänninen [24])
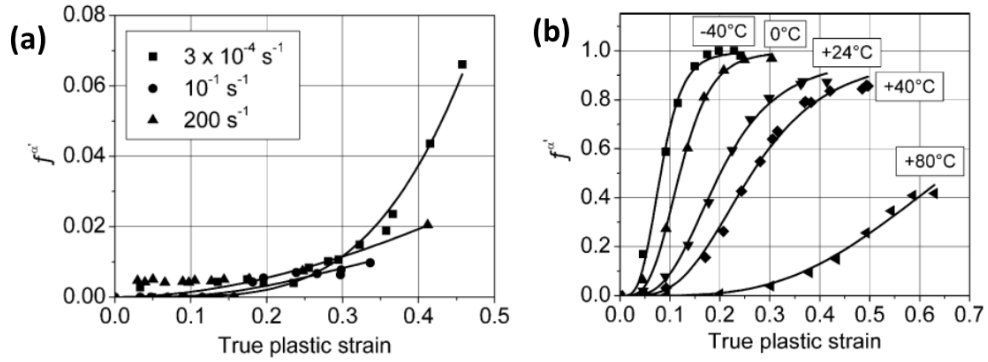
Figure 2.11. The variation of martensite volume fraction with strain of a deformed SS 304 alloy (tension) (a) at different strain rates and at room temperature and (b) at different temperatures and at 3×10^{-4} s^{-1} temperature

(Source: Talonen and Hänninen [24])

Rusinek et al.[25] carried out tension tests on an SS 304 at room temperature over a wide range of strain rate. An extended Rusinek-Klepaczko model (including the viscous drag effects) was used to model the thermo-viscoplastic behaviour. The developed constitutive model with a rate insensitivity plastic strain showed a good match with the experimental stress-strain curves between the quasi-static strain rates and 5000 s^{-1} (Figure 2.12)
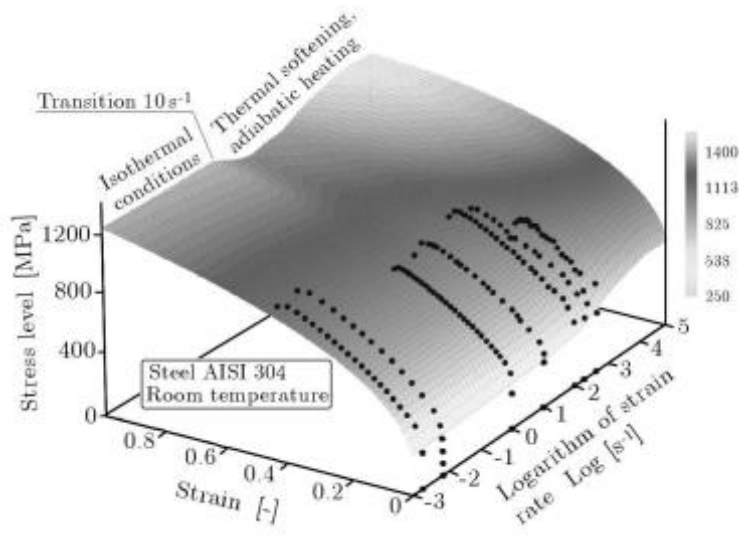
Figure 2.12. Comparison between experiments and analytical predictions of the constitutive model for an SS 304

(Source: Rusinek et al. [25])

Yaoo et al. [26] combined TI model, Bodner/Partom flow stress model and Bodner/Chan damage model to predict the TRIP behavior of SSs. The models were modified to take into account the temperature, strain rate, second hardening and failure. The used flow chart of FE algorithm and the damage model are shown in Figure 2.13. The fidelity of the used computational model was verified by comparing the model and experimental results.
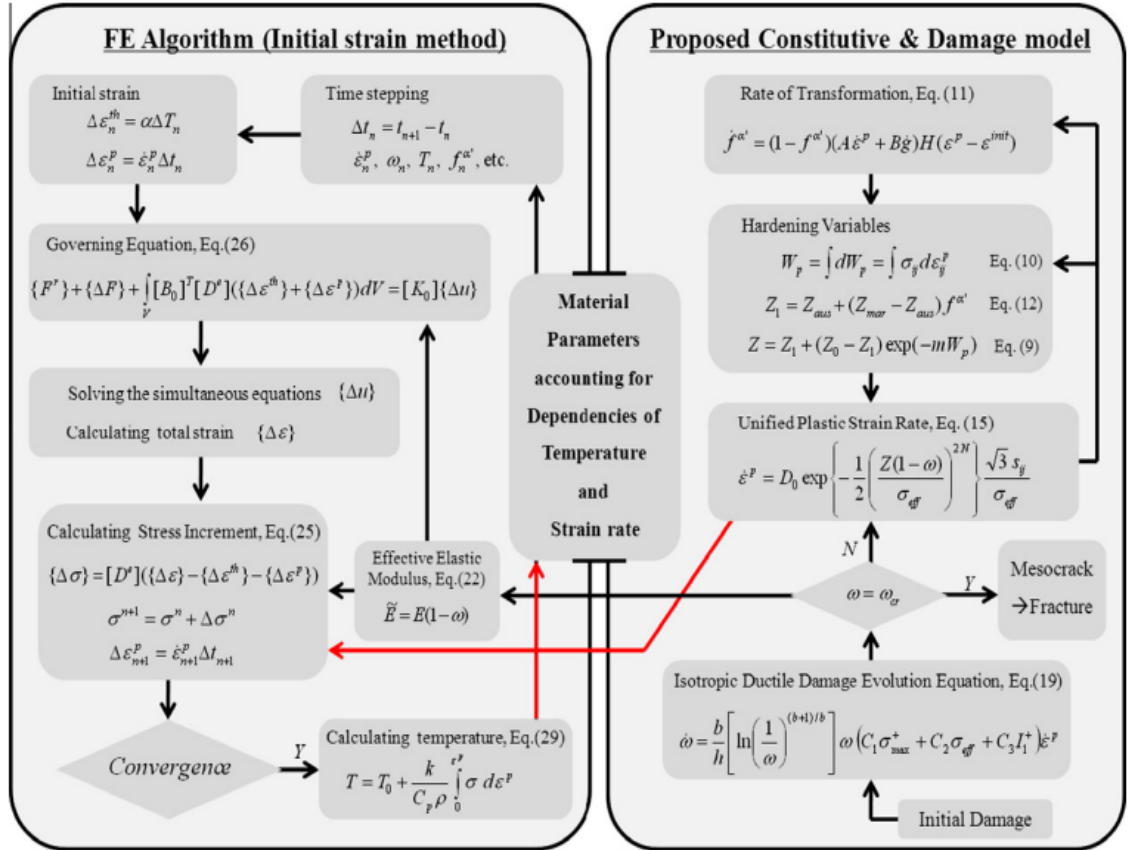
Figure 2.13.The flow chart of FE algorithm used in reference
(Source: Yoo et al. [26])

Zaera et al.[27] developed a numerical approach on the strain induced martensitic deformation by adding 1) the influence of elevated temperature on the dynamics of phase transition kinetics and 2) temperature-induced softening in austenitic steel using a homogenization approach to the previous models. The model well predicted the experimental stress-strain curves obtained at high strain rates and the effect of adiabatic heating on the stress-strain behaviour (Figures 2.14(a-d)).
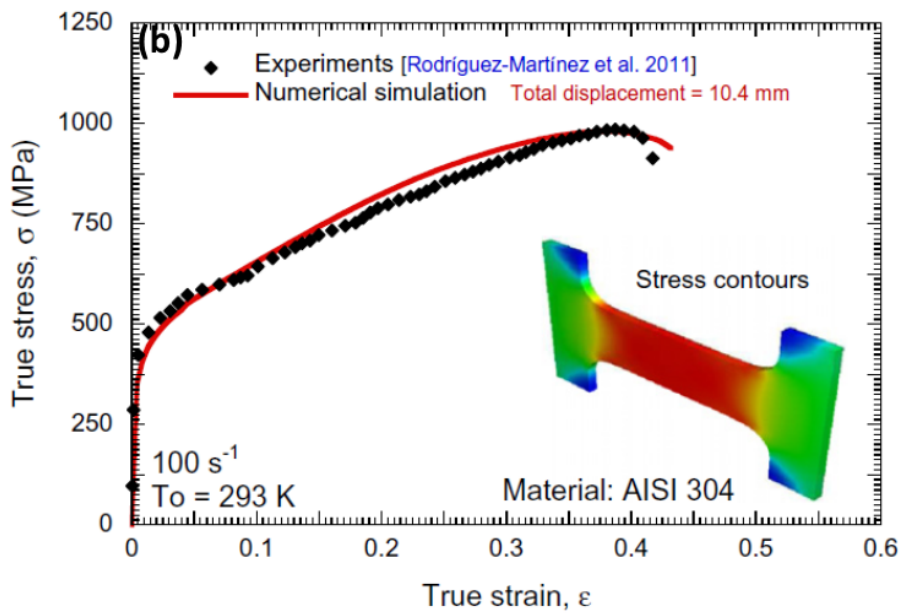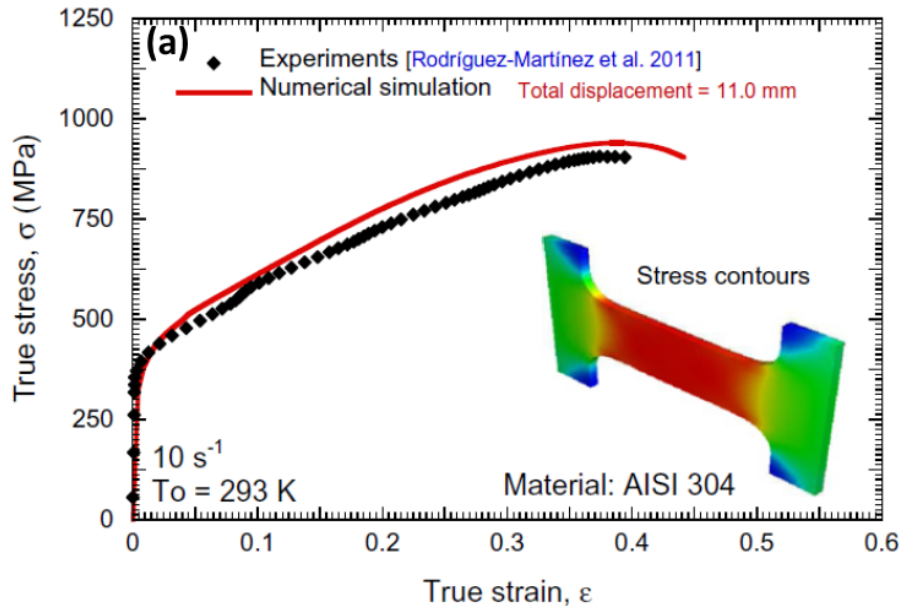
Figure 2.14. The numerical true stress-strain curves of the proposed model together with the experimental curves at (a)10, (b) 100 and (c) 5000 s^{-1} (room temperature) and (d) the numerical predictions of the volume fraction of martensite as a function of strain and strain rate

(Source: Zaera et al. [27])
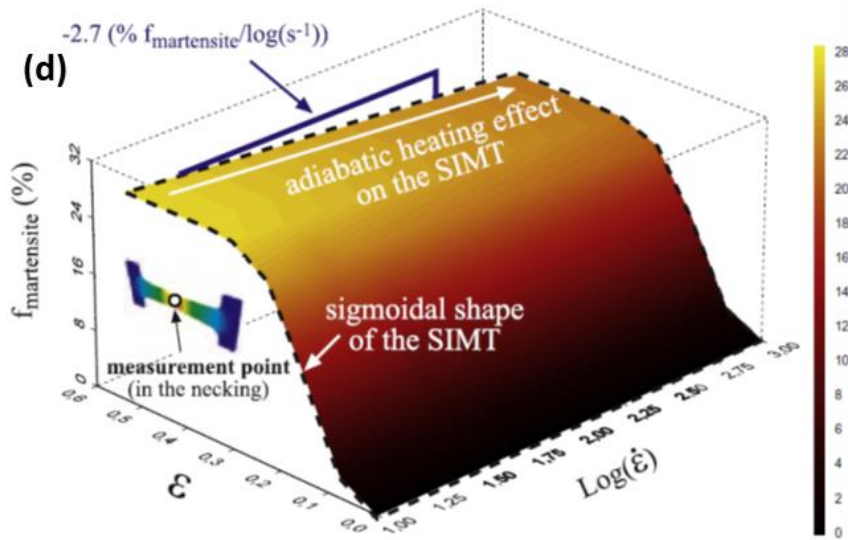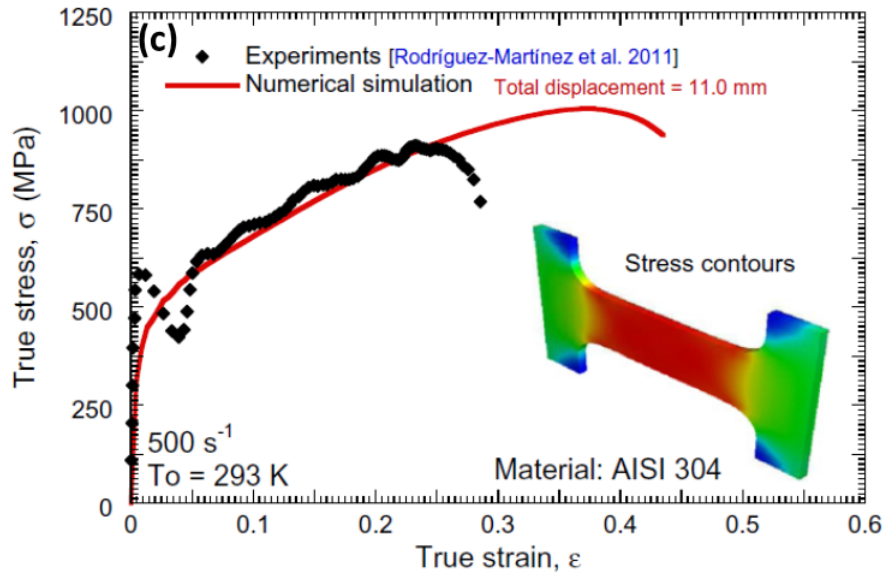
Figure 2.14 (cont.)

Peng et al.[28] predicted the tensile stress-strain curves of an SS 304 by using a modified Olson-Cohen Model. The α and β parameters in the Olson-Cohen model were also taken strain rate dependent sequentially as

$$\alpha = f(\Delta T)g(\dot{\varepsilon}) \tag{2.12}$$

$$f(\Delta T) = \alpha_o + q_1 \tag{2.13}$$

$$g(\dot{\varepsilon}) = \left(\frac{\dot{\varepsilon}}{\dot{\varepsilon}_o}\right)^{q_2} \qquad (2.14)$$

$$\beta = \beta_o \left(\frac{\dot{\varepsilon}}{\dot{\varepsilon}_o}\right)^{q_3} \qquad (2.15)$$

where ΔT is the temperature increase during the deformation, α_o is a physical parameter dependent only on temperature, q_1 is a material constant; $\dot{\varepsilon}_o$ is the reference strain rate; and q_2 and q_3 are the strain rate sensitivity exponents. The flow stresses of austenite and martensite were formulated using a modified JC equation. The flow stress was then calculated using the rule of mixture as

$$\sigma = \left(1 - f^{\alpha'}\right)\sigma_\gamma + f^{\alpha'}\sigma_{\alpha'} \qquad (2.16)$$

where σ_γ and $\sigma_{\alpha'}$ are the flow stress of austenite and martensite, respectively. The predicted martensite volume fraction as function of strain and determined stress-strain curves at different strain rates are shown together with the experimental results in Figure 2.15(a) and (b), respectively.
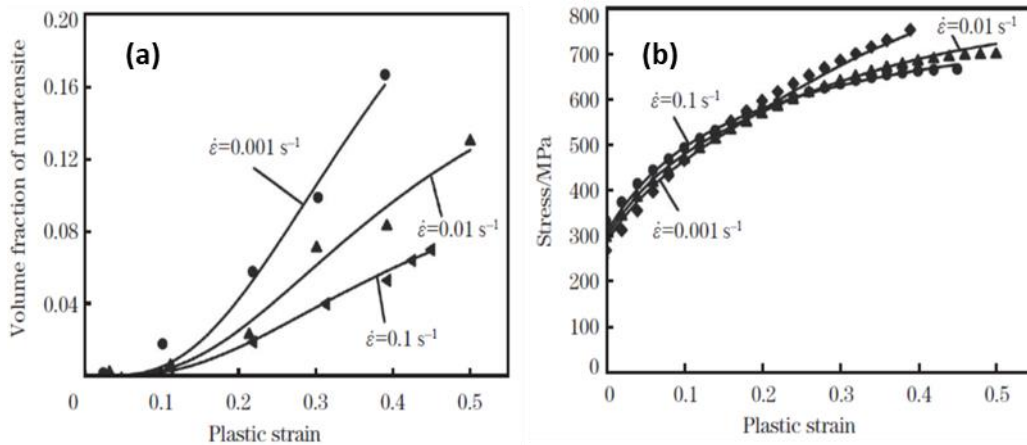
Figure 2.15. (a) the predicted martensite volume fraction as function of strain and (a) determined stress-strain curves at different strain rates

(Source: Peng et al. [28])

(a)

(b)
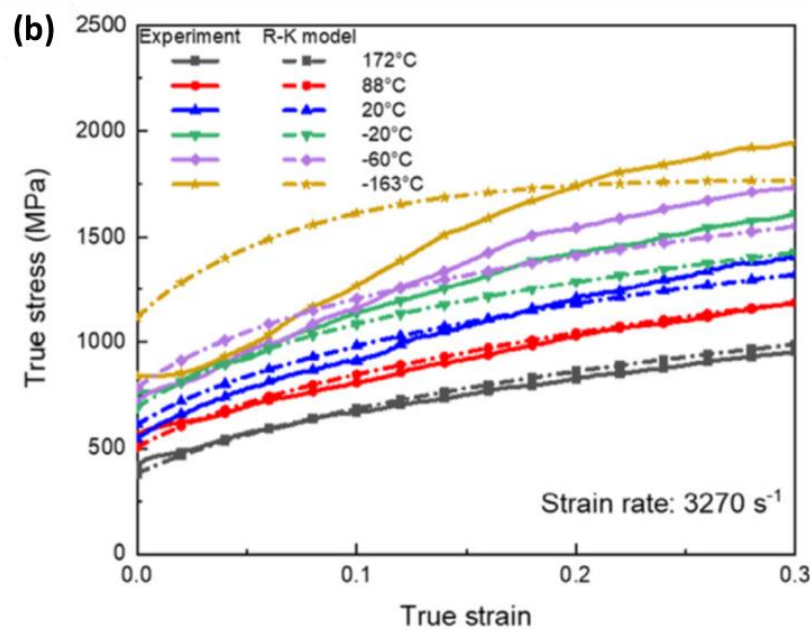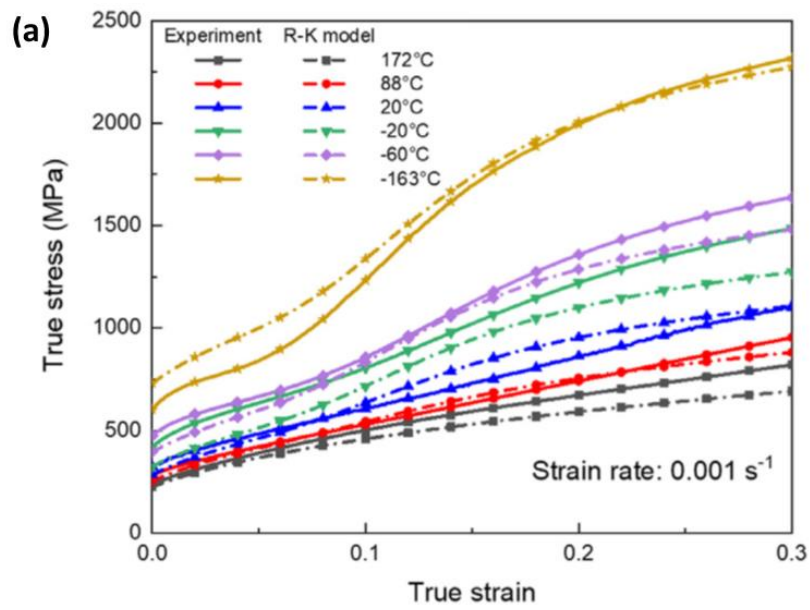
Figure 2.16. Comparison of (a) flow stress curves between experiment and RK model at
(a) 1×10^{-3} and (b) 2370 s^{-1} and comparison of strain rate sensitivity between
experiments and the extended RK model at (c) 0.05 and (d) 0.2 strain
(Source: Jia et al. [29])
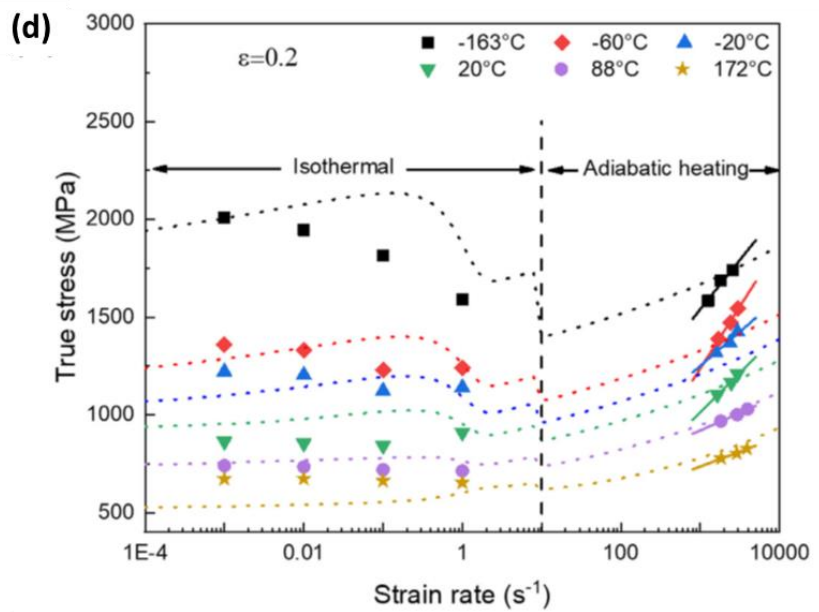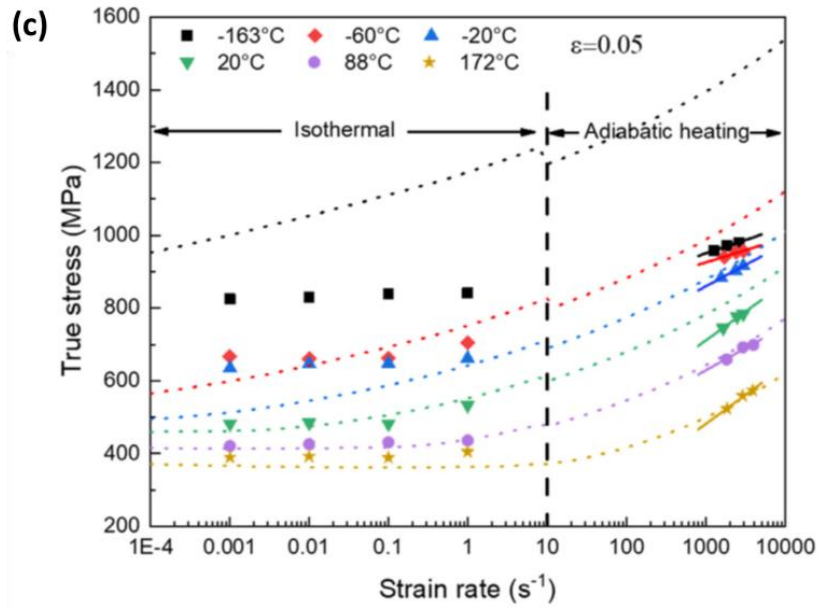
Figure 2.16 (cont.)

Jia et al[29] carried out experimental compression tests on an SS 304 specimen between -163°C and 172°C and between 10^{-3} s^{-1} and 3270 s^{-1}. The deformation of the tested specimens was modelled using a modified Rusinek-Klepaczko material model by taking into account the martensitic transformation as

$$\sigma = \frac{E(T)}{E}\left[\sigma_\mu(\varepsilon, \dot{\varepsilon}, T) + \sigma^*(\dot{\varepsilon}, T) + \sigma_{Tr}(\varepsilon, \dot{\varepsilon}, T)\right] \tag{2.17}$$

where σ_μ, σ^* and σ_{Tr} are sequentially the internal stress (long range obstacles), the effective stress (short range obstacles) and the stress component caused by martensitic transformation. The experimental results showed that at quasi-static strain rates between 1×10^{-3} s^{-1} and 1 s^{-1} and between -163°C and -20°C, the stress-strain displayed an S-shape with a second strain hardening (Figures 2.16 (a) and (b)). It was also shown that due to adiabatic heating, the flow stresses decreased more rapidly at high strains than low strains at increasing strain rates and at low temperatures (Figures 2.16(c) and (d)). The material model was also validated by simulating the ballistic impact tests in the Abaqus/Explicit.
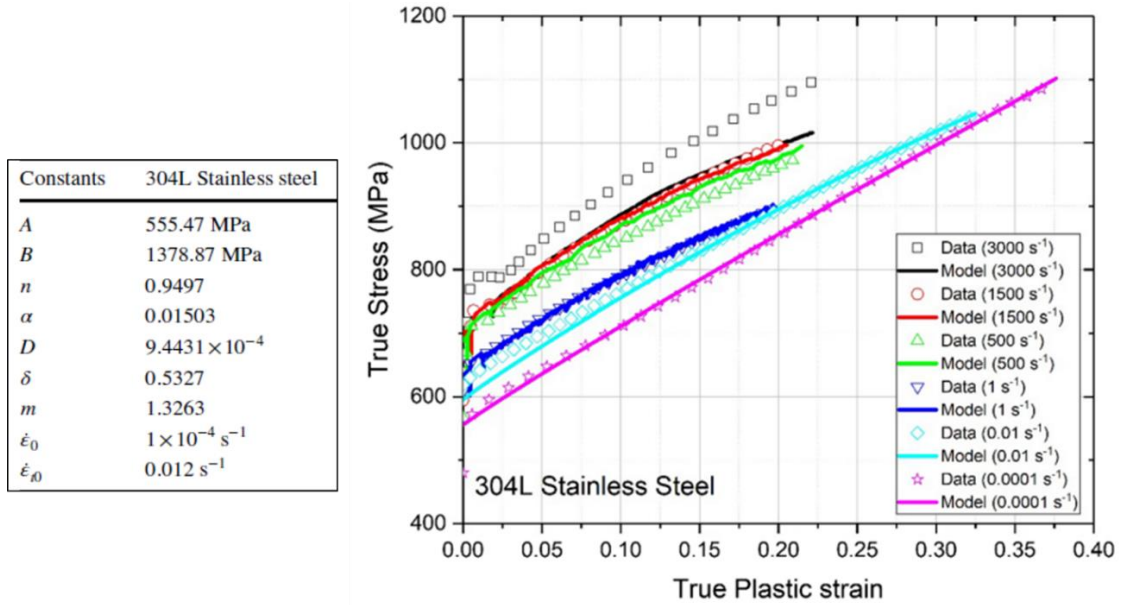
Figure 2.17. The experimental and model predicted true stress–strain response of an SS 304L until necking

(Source: Song and Sanborn [30])

Song and Sanborn[30] confirmed the experimental tensile test results of an SS 304 between 10^{-3} s^{-1} and 3000 s^{-1} at room temperature using a modified JC model as

$$\sigma = (A + B\varepsilon^n)\left(\frac{\dot{\varepsilon}}{\dot{\varepsilon}_o}\right)^\alpha \left\{1 - \left[\frac{D\left(\frac{\dot{\varepsilon}}{\dot{\varepsilon}_o}\right)^\alpha Y(\varepsilon)}{1+\left(\frac{\dot{\varepsilon}}{\dot{\varepsilon}_o}\right)^{-\frac{1}{\delta}}}\right]^m\right\} \tag{2.18}$$

In above equation, there are eight model constants: A, *B, D, m, n,* α, δ and *Y* to be determined experimentally. The determined model constants are shown in Figure 2.17 together with the model and experimental stress-strain curves at different strain rates. In the same figure, $\dot{\varepsilon}_{ot}$ represents the transition strain rate from isothermal to adiabatic condition.

,
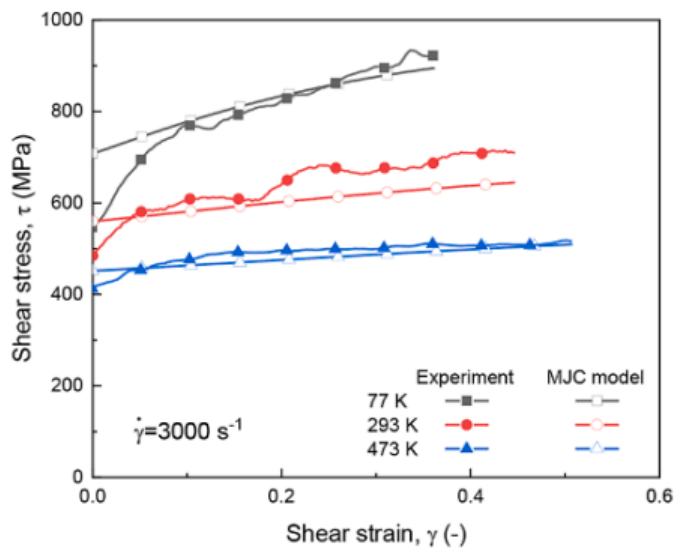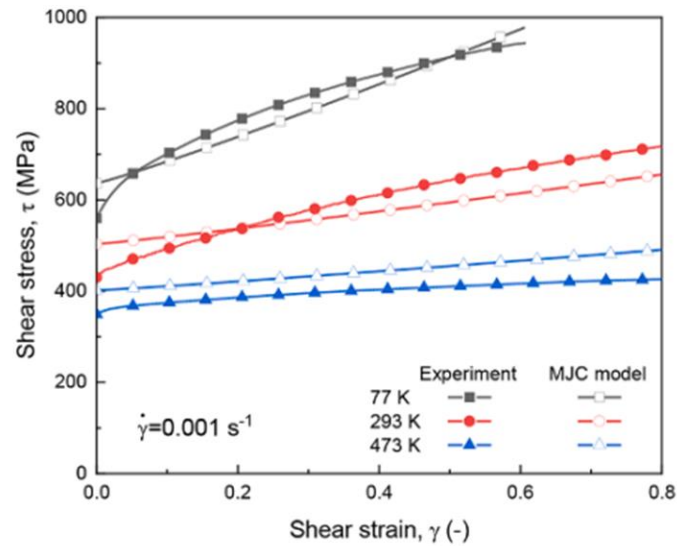
(cont. on the next page)

Figure 2.18. The model parameters and experimental and model flow stress curves at different strain rates and different temperatures

(Source: Jia et al. [31])

A (MPa)	B_0 (MPa)	c_0	m	n_0	n_1	n_2	$\dot{\varepsilon}_0$
1102	302	1.933	1.644	1.089	-0.653	0.654	120000
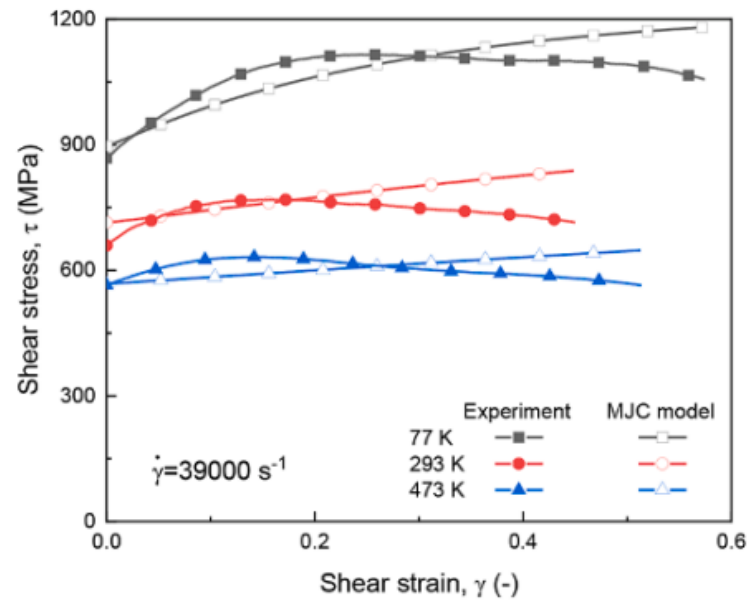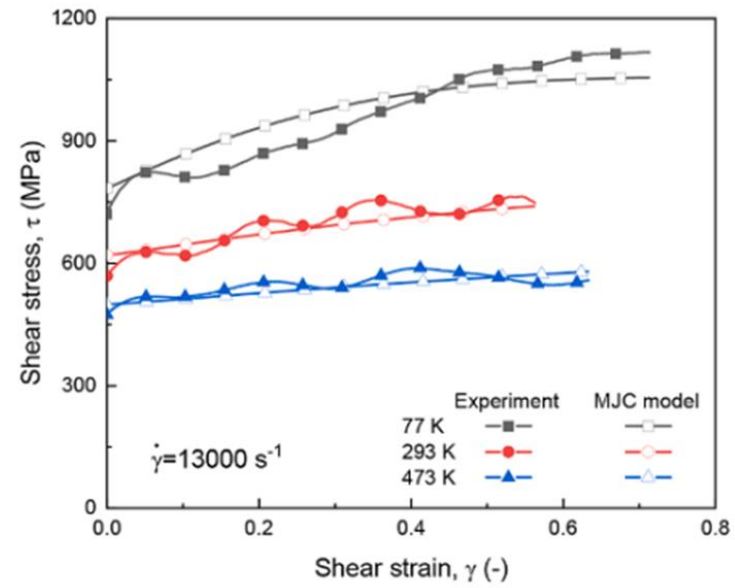
Figure 2.18 (cont.)

Jia et al.[31] conducted shear tests on an SS 304 between 77K and 473K in the strain rate range from 0.001 to 39000 s^{-1}. A modified Johnson Cook model was used to predict the strain rate and temperature dependent stress-strain behaviour as

26

$$\sigma = (A + B\varepsilon^n)\left(1 + c\ln\left(\frac{\dot{\varepsilon}}{\dot{\varepsilon}_o}\right)\right)\left\{1 - \left[\frac{T-T_r}{T_m-T_r}\right]^m\right\} \tag{2.19}$$

$$B(\dot{\varepsilon}, T) = B_o\left(1 - \frac{\ln\dot{\varepsilon}}{\ln\dot{\varepsilon}_{max}}\right)^{n1}\left(\frac{T_m}{T}\right)^{n2} \tag{2.20}$$

$$c(\dot{\varepsilon}) = 1 + \left(\frac{\dot{\varepsilon}}{\dot{\varepsilon}_o}\right)^{\frac{1}{c_o}} \tag{2.21}$$

$$\Delta T(\varepsilon) = \frac{\beta}{\rho C_p}\int \sigma d\varepsilon \tag{2.22}$$

where n_o, n_1, n_2 and c_o are the constants, ρ is the density, β is the average Taylor-Quinney coefficient defines the proportion of plastic work converted into heat, while Cp represents the specific heat. The determined modified Johnson Cook model parameters and the forecasted model stress-strain curves at various strain rates and temperatures are presented in Figure 2.18 together with the experimental ones.

Kishore et al.[32] studied the strain rate effect on the flow stress, work hardening, hardness, dislocation density and cell size of an SS 304. Tensile tests were performed at 1×10^{-4} s^{-1} (called SSR) and at 1×10^{-2} s^{-1} (called HSR). The SSR specimen showed lower stresses until about 0.4 strain; thereafter, the stress increased over that of HSR specimen (Figure 2.19(a)). This proved an earlier transition to the dislocation dominant deformation stage (stage 3) in the HSR tested specimen. Due to higher work hardening rate of HSR specimen at low strains, it exhibited a higher YS but a reduced ultimate tensile strength UTS and ductility in comparison to SSR deformed specimen. This was caused by the higher overall work hardening in SSR specimen at larger strains due to the formation of a higher fractions of martensite and twins. A cross-over in the work hardening of the SSR and HSR specimen was found at around 0.05 strain (Figure 2.19(b)) and over that strain the work hardening rate of the SSR specimen was shown to be higher than that of the HSR specimen. The increase in the dislocation density with increasing strain was also shown to be higher in the SSR tested specimen with a reduced dislocation cell size (Figure 2.19(c)) Hence, the fracture surface of the SSR specimens contained finer dimples than that of HSR specimen. The measured harness values of the SSR specimen were shown to

be higher than those of the HSR tested specimen due to the increased dislocation density in the SSR specimen (Figure 2.19(d)).

(a)

(b)
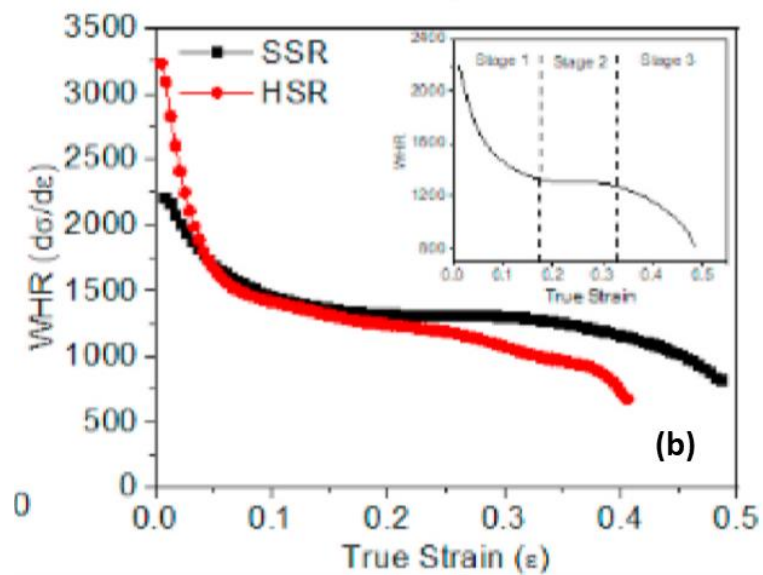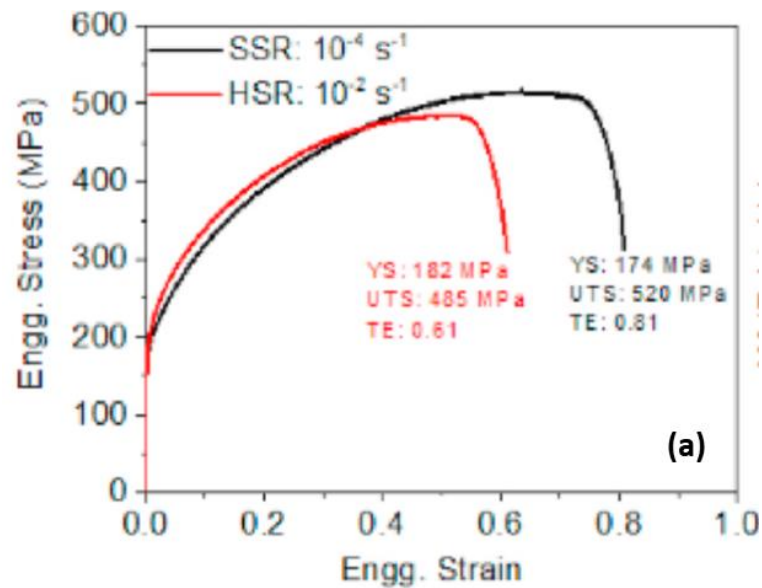
(cont. on the next page)

Figure 2.19.(a) SSR and HSR engineering stress-strain and (b) corresponding work hardening curve, (c) dislocation density and crystallite size and (d) hardness variation in HSR and SSR specimens

(Source: Kishore et al. [32])
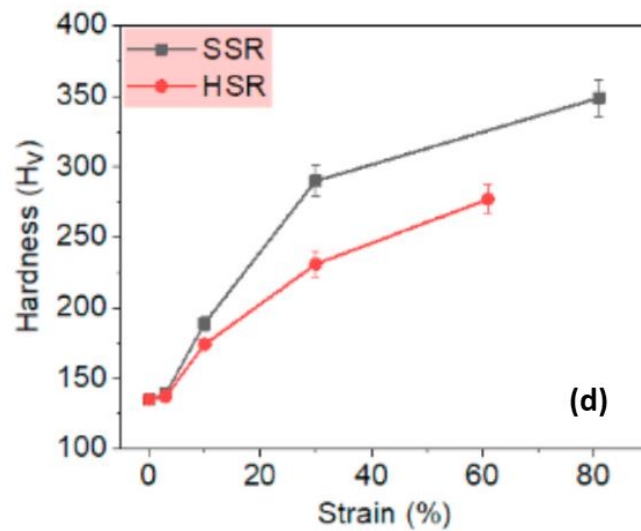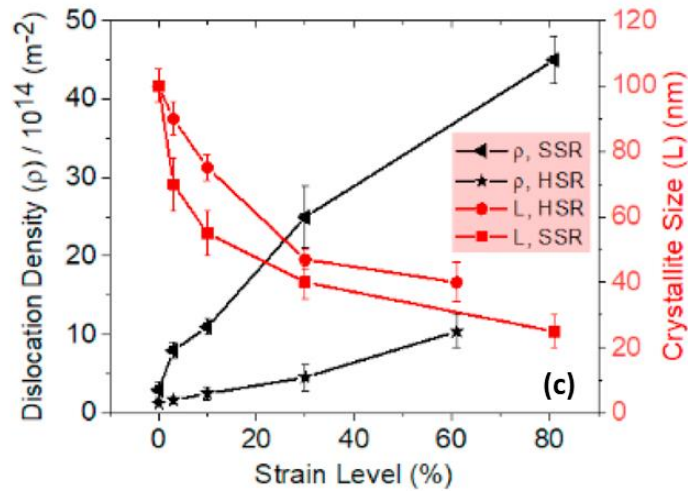
Figure 2.19 (cont.)

Li et al.[33] carried out quasi-static and dynamic compression tests on an SS 304 at a temperature range of 20-600°C and a strain rate range of 0.001-3000 s⁻¹. Dynamic compression tests were carried out using a compression SHPB apparatus. The JC flow stress model parameters were then determined from the experimental stress-strain curves. The determined model stress-strain curves are shown in Figure 2.20 at four different strain rates and at different temperatures. A good match between the model and experiments seen in the same figures is provided by using a variable *c* value between different strain rate regimes and a variable *m* value at different temperature regime as tabulated in Figure 2.20.

A(MPa)	B(MPa)	n	c		
			1000 s^{-1}	2000 s^{-1}	3000 s^{-1}
270	637	0.7587	0.0749	0.0921	0.1003

m		
200°C	400 °C	600 °C
0.538	0.653	0.808
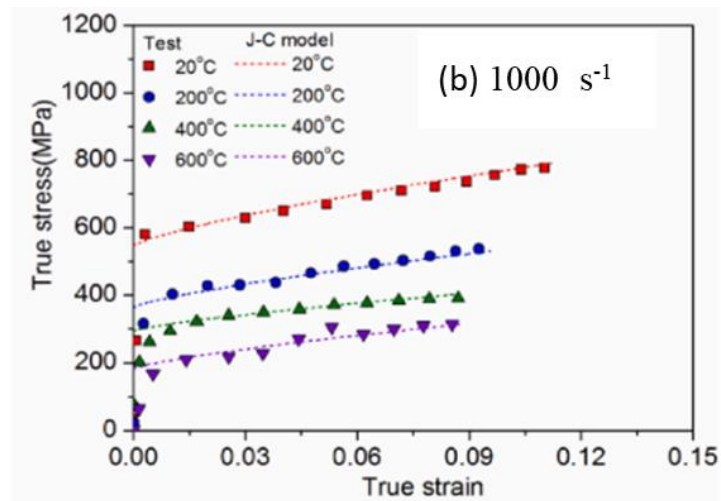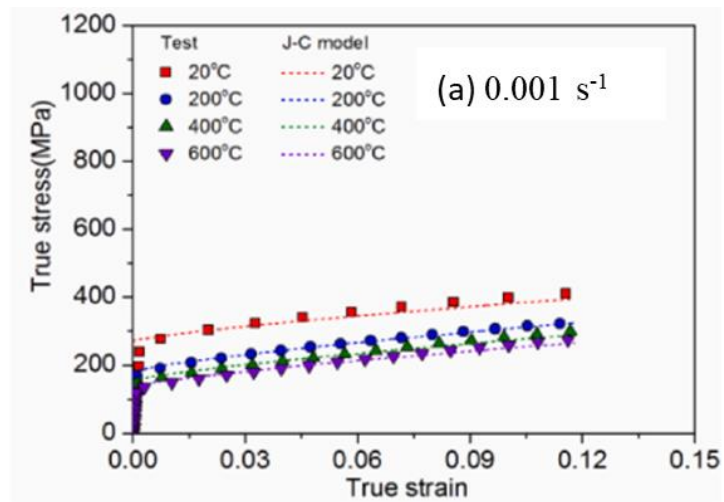
(cont. on the next page)

Figure 2.20. Comparison of experimental results and JC fitting related to SS 304 and JC model parameters

(Source: Li et al. [33])
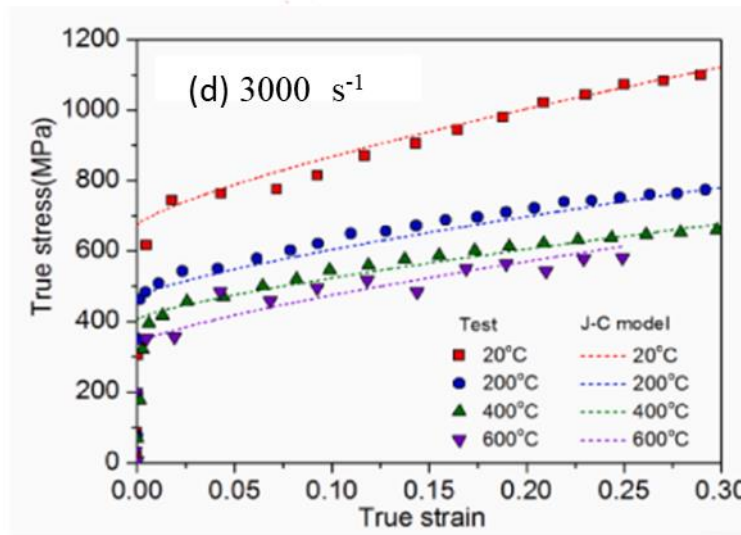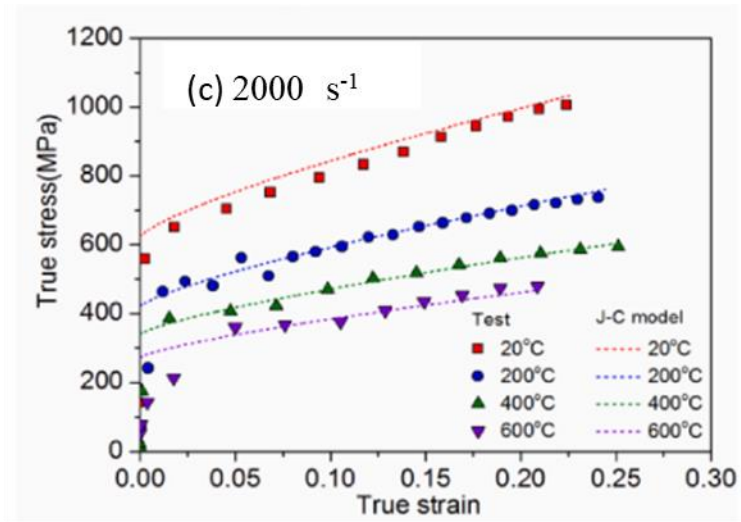
Figure 2.20 (cont.)

Jia et al.[34] investigated experimentally and numerically the flow stress-strain behaviour of an SS 304, in the strain rate range of 0.001-39000 s^{-1} and temperature range of 77-1073 K. The Material model parameters of eight constitutive models: JC, Khan-Liang-Farrokh (KLF), Hollomon/Voce (HV), Zerilli-Armstrong (ZA), Voyiadjis-Almasri (VA), Nemat-Nasser-Li (NNL), BP and ANN (artificial Neural Network) were determined, and the derived model stress-strain profiles were juxtaposed with the experimental stress-strain data across various strain rates and temperatures. (Figure 2.21 for the JC model). ANN was found giving the least error margin for the stress-strain curves, the average error margins of NNL and VA were 6.27% and 7.20%, respectively.

The average margin of error for the PB, KLF, and JC models was 10%. Highest error was in the ZA material model.

A (MPa)	B (MPa)	n (-)	C (-)	m (-)
544.2	507.2	0.4673	0.0321	0.4546
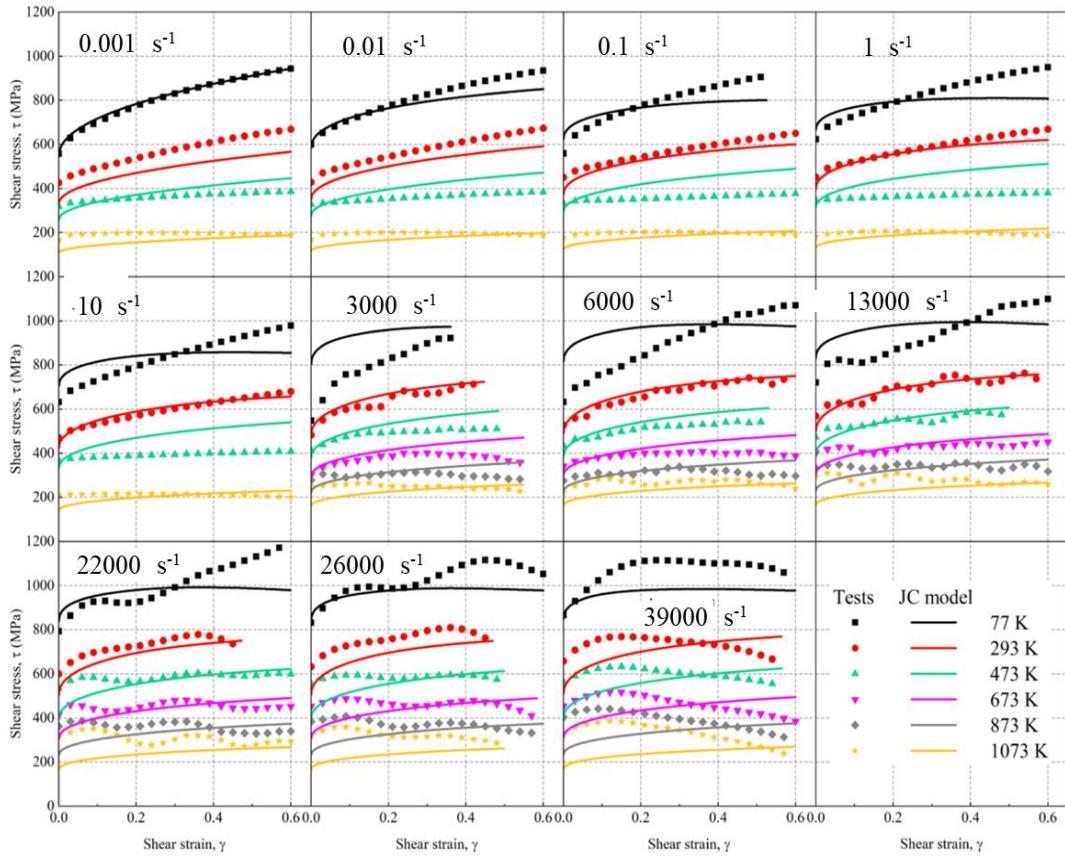
Figure 2.21. JC model parameters and the comparison of experimental and JC stress-strain curves

(Source: Jia et al. [34])

Seo et al.[35] carried out tensile tests on an SS 304 at the strain rates ranging from 10^{-3} s^{-1} to 1000 s^{-1} at room temperature. The stress-strain curves at different strain rates were used to construct the JC and modified JC models. The used modified JC equation is

$$\sigma = (A + B\varepsilon^n)[1 + C_1 \left(\frac{\dot{\varepsilon}}{\dot{\varepsilon}_o}\right) + C_2 \left(\frac{\dot{\varepsilon}}{\dot{\varepsilon}_o}\right)\varepsilon] \tag{2.23}$$

In above equation, C_{JC} is the strain rate sensitivity parameter. The obtained model parameters of the JC and modified JC are listed in Figure 2.22. The modified JC model was shown to reduce the errors between model and experiments (Figures 2.22(a) and (b)).

Material	$\dot{\varepsilon}_0$ (s^{-1})	A (MPa)	B (MPa)	n	C_{JC}	C_1	C_2
304	0.001	325	1616	1.06	0.022	0.028	−0.053
304 L		325	1423	0.91	0.025	0.028	−0.034
316 L	0.0004	250	1143	0.67	0.015	0.020	−0.047
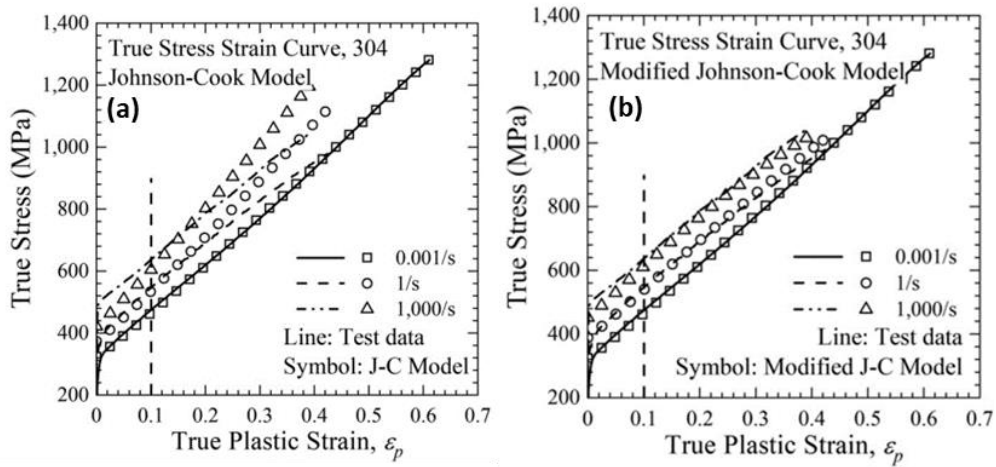
Figure 2.22. Comparison of experimental and model true stress–strain response of SS 304, (a) JC and (b) modified JC model

(Source: Seo et al. [35])

2.2. Johnson Cook Flow Stress and Damage Models

The JC flow stress model (equation) [36] was introduced by Johnson and Cook. It is one of the most widely used models in the impact and structural numerical analyses. The JC flow stress model takes into account simultaneously the effect of strain hardening, temperature and strain rate strengthening on flow stress. It is given as

$$\sigma_y = \left[A + B\bar{\varepsilon}_p^n \right]\left[1 + C ln(\dot{\varepsilon}^*) \right]\left[1 - (T^*)^m \right] \tag{2.24}$$

$$\dot{\varepsilon}^* = \frac{\dot{\varepsilon}_p}{\dot{\varepsilon}_0} \tag{2.25}$$

$$T^* = \frac{T - T_r}{T_m - T_r} \qquad (2.26)$$

where, $\overline{\varepsilon_P}$ represents the equivalent plastic deformation, A denotes the yield stress, B is the coefficient of strain hardening, n refers to the exponent of strain hardening, $\dot{\varepsilon}_p$ indicates the effective rate of plastic strain, $\dot{\varepsilon}_0$ denotes the reference rate of strain, c indicates the coefficient for strain rate hardening, m signifies the thermal softening parameter, T represents the temperature, T_m refers the melting point, and T_r denotes the reference temperature, typically considered as the room temperature.

The JC damage or failure model [36] was introduced in 1985. It is based on the fracture strain model of Hancock and Mackenzie, developed in 1976 [37]. The Hancock and Mackenzie fracture model is based on a strain-, strain rate- and temperature-dependent void growth model. In the JC damage model, a damage parameter (D) showing a degree of continuity of damage is defined as

$$D = \frac{\overline{\varepsilon_P}}{\varepsilon_f} \qquad (2.27)$$

where ε_f is the equivalent failure strain. As seen in Figure 2.23, the value D is zero just before the damage starts to initiate at the ultimate tensile strength. The stress decreases from a maximum ($D=0$) to lower values as damage progresses and material fails when the stress becomes zero and the same time the value of D reaches one.

The JC equivalent failure strain is represented by the following relation

$$\varepsilon_f = [D_1 + D_2 \exp(D_3\sigma^*)][1 + D_4 \ln(\dot{\varepsilon}^*)][1 + D_5 T^*] \qquad (2.28)$$

Here, D_1 refers the initial failure strain, D_2 denotes the exponential factor, D_3 represents the triaxiality factor, D_4 refers strain rate factor, D_5 refers the temperature factor and σ^* signifies the stress triaxiality. The stress triaxiality is

$$\sigma^* = \frac{\sigma_h}{\sigma_e} \qquad (2.29)$$

where σ_e is the equivalent stress and σ_h is the hydrostatic stress.

34
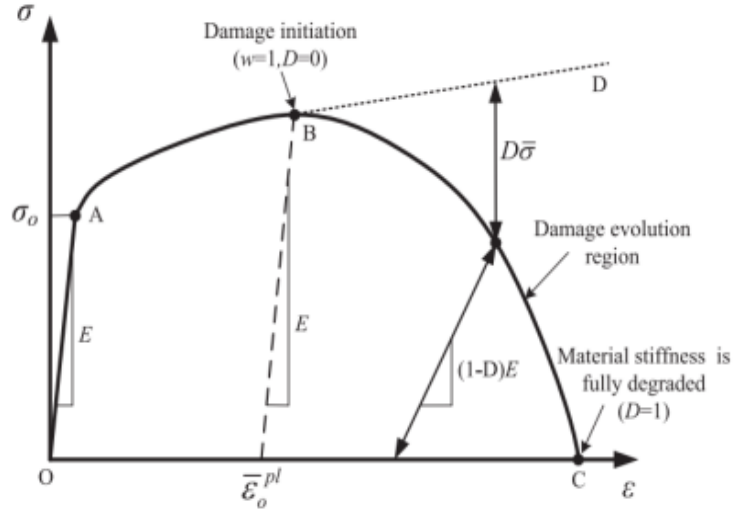
Figure 2.23. Failure strain history curve of a metallic material

(Source: Gkolfinopoulos and Chijiwa [38])

2.3. Modified Johnson Cook and Modified Zerilli Armstrong Flow Stress Model

The modified Johnson Cook is an empirical model similar to the JC flow stress model. The only difference between the modified and JC models is that the strain rate coefficient parameter is expressed in an exponential form in the modified JC as

$$\sigma_{eq} = \left(A + B\varepsilon_{eq}^n\right)\left(1 + \dot{\varepsilon}_{eq}^*\right)^C (1 - T^{*m}) \qquad (2.30)$$

While the JC and modified JC constitutive models are empirical, the Modified Zerilli Armstrong (MZA) model is physical-based. It is based on the thermally activated dislocation mechanics. The MZA flow stress is expressed as

$$\sigma_{eq} = \sigma_a + Be^{[-(\beta_0 - \beta_1 ln\dot{\varepsilon}_{eq})T]} + A\varepsilon_{eq}^n e^{[-(\alpha_0 - \alpha_1 ln\dot{\varepsilon}_{eq})T]} \qquad (2.31)$$

where σ_a, B, β_0, β_1, A, α_0, α_1 and n are the material constants. The MZA model is preferred over the JC model when the complex situations such as the strain rate, temperature and dislocation mechanics effects are considered. The material model is more

complex than the JC model as it involves with the couplings of different effects. Dey et al[39] used the MZA material to simulate the projectile impact on Weldox 460 E steel plates.

2.4. Extended Johnson-Cook Damage Law

LS - DYNA includes the modified JC and MZA models in the MAT 107 material card. The extended JC Damage model, similar to the JC damage model, is also included in the MAT 107 material card. The equation is given as

$$\varepsilon_f = [D_1 + D_2 e^{[D_3 \sigma^*]}][1 + \dot{\varepsilon}_{eq}^*]^{D_4}[1 + D_5 T^*] \tag{2.32}$$

As is noted in above equation, the difference between the extended JC damage model and the JC damage model is that the *D4* parameter is given in the exponential form in the extended model.

2.5. Cockcroft-Latham Damage Evolution Rule

In the Cockroft-Latham damage evolution rule, the strain energy determines the failure. The strain energy (*W*) and the damage criterion is given as[40]

$$W = \int_0^{\varepsilon_{eq}} \langle \sigma_1 \rangle \, d\varepsilon_{eq} \leq W_{cr} \tag{2.33}$$

where σ_1 is the maximum principal stress and ε_{eq} is the equivalent strain. When the *W* parameter reaches a value of W_{cr}, the damaged elements are allowed to wear out during the impact in the ballistic simulations. The model is applied to tensile stresses $\sigma_1 \geq 0$, and when $\sigma_1 \leq 0$, there will be no fracture.

2.6. Johnson–Holmquist Constitutive Model-2

Johnson–Holmquist constitutive model-2 (JH-2)[41] was developed for brittle materials. The model is described in Figure 2.24.

The normalized strength σ^* ($\sigma^* = \frac{\sigma}{\sigma_{HEL}}$) is expressed by the following equation

$$\sigma^* = \sigma_i{}^* - D(\sigma_i{}^* - \sigma_f{}^*) \tag{2.34}$$

Here, σ_{HEL} is the Hugonoid stress, $\sigma_i{}^*$ is the strength of the undamaged sample ($\sigma_i{}^* = \frac{\sigma_i}{\sigma_{HEL}}$), $\sigma_f{}^*$ is the normalized breaking strength ($\sigma_f{}^* = \frac{\sigma_f}{\sigma_{HEL}}$) and D is the damage value, where 0 indicates undamaged condition and 1 the broken condition. The normalized strength of the undamaged sample is expressed by the following equation

$$\sigma_i{}^* = A(P^* + T^*)^N(1 + cln\dot{\varepsilon}^*) \tag{2.35}$$

Normalized breaking strength is formulated as

$$\sigma_f{}^* = B(P^*)^M(1 + cln\dot{\varepsilon}^*) \tag{2.36}$$

Here, P_{HEL} is the Hugonoid pressure, P^* is the normalized pressure ($P^* = \frac{P}{P_{HEL}}$), T^* is the normalized tensile strength ($T^* = \frac{T}{P_{HEL}}$), $\dot{\varepsilon}^*$ is the normalized strain rate ($\dot{\varepsilon}^* = \frac{\dot{\varepsilon}}{\dot{\varepsilon}_{ref}}$; where $\dot{\varepsilon}_{ref}$ reference strain rate) and A, N, c and M are the model constants. The JH-2 stress-pressure graph is shown in Figure 2.23(a) for $D=0, 0<D<1$ and $D=1$. The SFMAX value here is the optional fracture strength that limits the normalized fracture strength. When $M=1$, the JH-2 model, and the JH-1 model become the same.

In the JH-2 model, the plastic fracture strain (ε_f^p) is

$$\varepsilon_f^p = D_1(P^* + T^*)^{D_2} \tag{2.37}$$

Here D_1 and D_2 are the material constants. When $P^* = -T^*$, the material is brittle, no plastic strain occurs. The fracture strain and relative volume increase with increasing pressure, as seen in Figure 2.24(b). Furthermore, the D value varies from 0 to 1 as seen in the same figure.
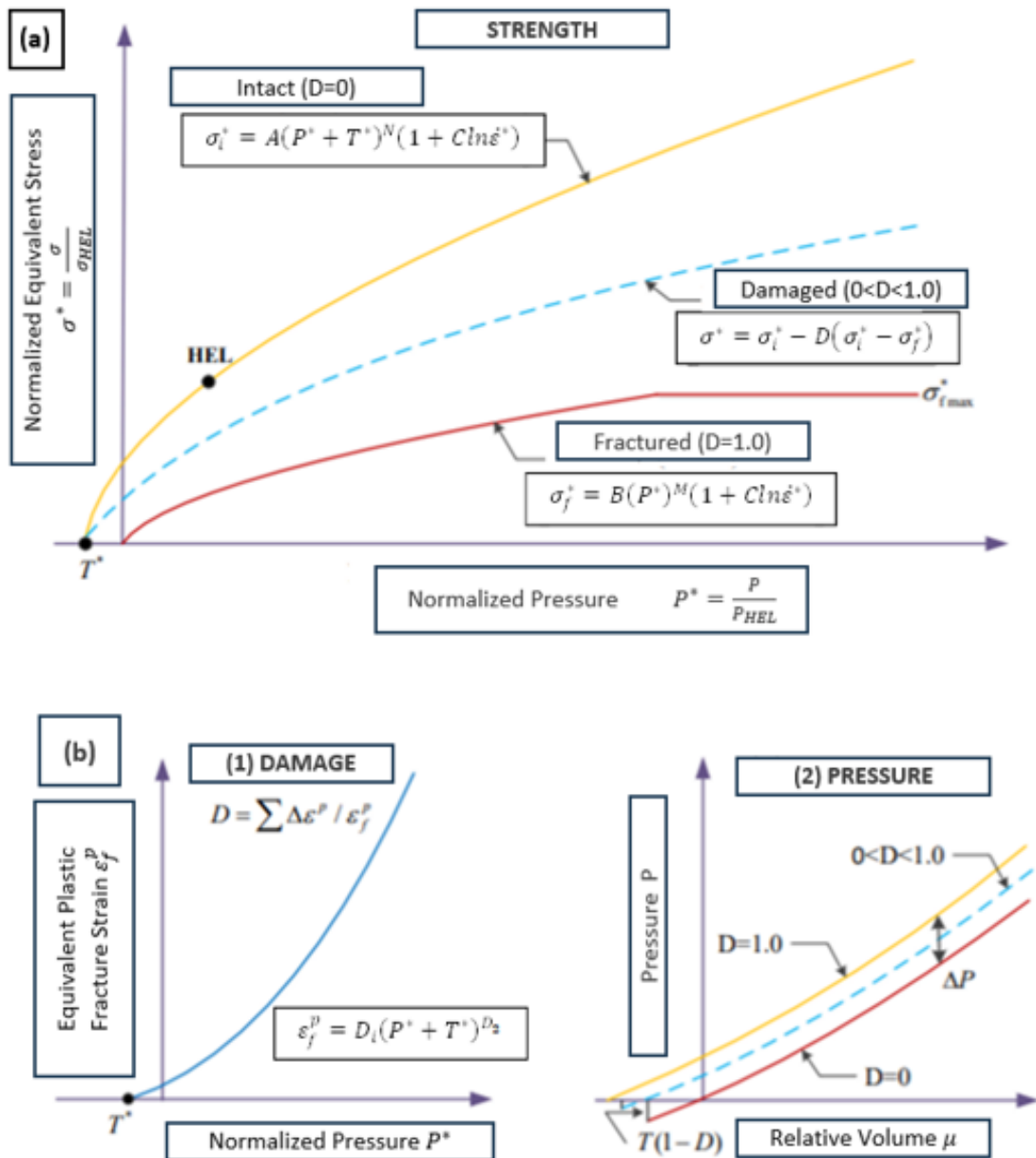
Figure 2.24. JH-2 (a) stress, (b.1) strain model and (b.2) relative volume change with
pressure

(Source: Johnson and Holmquist [41])

2.7. Equation of State

The equation of state (EOS) defines the interdependence between pressure, volume, and temperature of a material. The EOS is related to the hydrodynamic pressure which is the function of density and internal energy. Experimental data about the types of

pressures can be obtained by Shock transition experiment.[42] There are two types of EOS commonly used in metallic materials. These are the Mie-Gruneisen and polynomial.

The pressure in the Mie-Gruneisen EOS is expressed as

$$P = \rho_o C^2 \mu \left\{ \frac{\left[1+\left(1-\frac{\gamma_o}{2}\right)\mu-\frac{a}{2}\mu^2\right]}{\left[1-(S_1-1)\mu-S_2\frac{\mu^2}{\mu+1}-S_3\frac{\mu^3}{(\mu+1)}\right]^2} \right\} + (\gamma_o + a\mu)E \qquad (2.38)$$

for compression ($\mu > 0$) and

$$P = \rho_o C^2 \mu + (\gamma_o + a\mu)E \qquad (2.39)$$

for tension ($\mu < 0$). In above equations, μ is volume parameter ($\mu = \rho/\rho_o - 1$); ρ and ρ_o are sequentially the density and the reference density; C is the speed of sound; γ_0 is the Gruneisen gamma; S_1 is the linear material coefficient; S_2 is the quadratic material coefficient; S_3 is the cubic material coefficient; a the first order volume changing γ_o (the default value of a is γ_o) and finally E is the internal energy per unit of reference volume.

The pressure in polynomial EOS is expressed as

$$P = C_0 + C_1\mu + C_2\mu^2 + C_3\mu^3 + (C_4 + C_5\mu)E \qquad (2.40)$$

where C_0-C_5 are the hydrodynamic pressure constants.

2.8. Motivation for the Thesis

Previous experimental and numerical studies on the quasi-static and high strain rate deformation behaviour and the flow stress equations of SS 304 alloy have been summarized. These studies mostly focused on the determination of the stress behaviour as function of the volume fraction of martensite and few studies have also attempted to fit the stresses to the well-known constitutive equations. Note that the failure behaviour of the alloy is equally important in the impact related applications as it determines the

energy absorption as with the flow stress and the ultimate resistance to the plastic deformation.　No systematic studies have been so far performed on the determination of the damage models of SS 304 alloy in order to simulate its dynamic loading behaviour. In this thesis, the parameters of the JC flow stress and JC damage equations were experimentally determined for an SS 304. The determined parameters were then verified and also calibrated by modelling the experimental tests used to extract these parameters. In the content of the thesis, quasi-static and high strain rate tension tests were conducted. The numerical models of these tension tests were implemented in LS-Dyna.　Finally, the experimental ballistics tests performed at 800 m s^{-1} on B$_4$C coated and uncoated SS 304 plates were also simulated in Ls-Dyna using the determined model parameters.

CHAPTER 3

MATERIALS AND TESTING METHODS

3.1. Materials and Testing Methods

A rolled-SS 304 plate was used to prepare mechanical test specimens in the rolling direction through machining. The quasi-static and SHTB tests were conducted to determine the numerical flow stress and damage models of the investigated SS 304. The tension tests were conducted in accordance with the ASTM E8/E8M standard[43]. The technical drawings and pictures of the used tension test specimens with different stress triaxiality (σ^*) values are shown in Figures 3.1(a-d). Circular cross-section (axisymmetric) quasi-static strain rate tension test specimens with the stress triaxiality of 0.33 had a diameter of 4 mm and a gage length of 20 mm (Figure 3.1(a)).
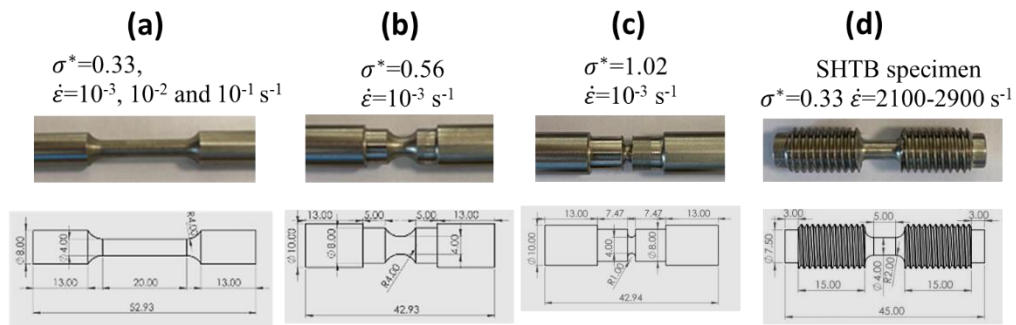
Figure 3.1.The tension test specimen pictures showing the sizes: (a) quasi-static, $\sigma^* = 0.33$ (b) quasi-static, $\sigma^* = 0.56$, (c) quasi-static, $\sigma^* = 1.02$ and (d) SHTB, $\sigma^* = 0.33$

These specimens were tested at the strain rates of 10^{-3}, 10^{-2} and 10^{-1} s^{-1}. The notched specimens with $2a=4$ mm (the same as the diameter of the tension test specimens) had the R values of 4 and 1 mm, corresponding to the stress triaxialities sequentially to 0.56 and 1.02 (Figures 3.1(a) and (b)). The notched specimens were tested at 10^{-3} s^{-1}. A technical drawing and a picture of the SHTB test specimen is shown in Figure 3.1(d). The SHTB test specimens maintained the same diameter with the quasi-

static strain rate test specimens while the gage length in these specimens was reduced to 5 mm in order to attain the stress equilibrium in the SHTB tests. These specimens were securely attached directly to the ends of the tension bars using screws and tested at the average strain rates of 2100 and 2900 s^{-1}.

The quasi-static tension tests were conducted in a Shimadzu AG-X 300 KN universal test machine (Figure 3.2) at the constant cross-head speeds corresponding to 10^{-3}, 10^{-2} and 10^{-1} s^{-1} strain rates. A video extensometer synchronized with the test machine was used to determine the test specimen displacement and a SONY camera was used to record the deformation. The camera records were then used to determine the diameter of test specimen during a test until the failure strain using the ImageJ software. From these records, the average true stress (σ_{Avg}) was calculated as

$$\sigma_{Avg} = \frac{P}{A} \tag{3.1}$$

where, P is the applied load and A is the instantaneous area of test specimen.
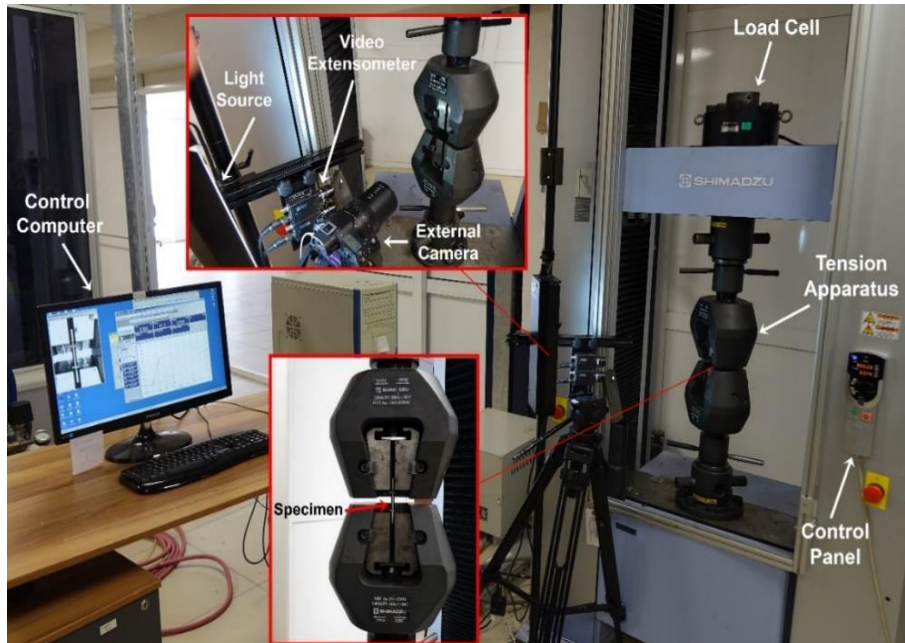
Figure 3.2. Shimadzu AG-X 300 KN universal testing machine

Note that the stress after necking is three dimensional as shown in Figure 3.3. In the same figure, σ_r is the radial, σ_θ is the hoop and σ_z is the axial stresses in the necking,

a signifies the radius of the neck's cross-sectional area; and R refers the local radius of the neck. The radial, hoop and axial stresses for a round specimen are sequentially given as [44]

$$\sigma_r = \sigma_\theta = \frac{\sigma_{Avg}}{(1+\frac{2R}{a})}\left(\frac{ln\left(\frac{a^2+2aR-r^2}{2aR}\right)}{ln(1+\frac{2R}{a})}\right) \tag{3.2}$$

$$\sigma_z = \frac{\sigma_{Avg}}{(1+\frac{2R}{a})}\left(\frac{1+ln\left(\frac{a^2+2aR-r^2}{2aR}\right)}{ln(1+\frac{2R}{a})}\right) \tag{3.3}$$

Since the shear stresses are zero at the minimum cross-section, the principal stresses are the radial, hoop and axial stresses. The von Misses equivalent stress (σ_{eq}) is

$$\sigma_{eq} = \frac{1}{\sqrt{2}}\sqrt{[(\sigma_z - \sigma_r)^2 + (\sigma_r - \sigma_\theta)^2 + (\sigma_\theta - \sigma_z)^2]} \tag{3.4}$$

Inserting Equations 3.2 and 3.3 into Equation 3.4 yields the equivalent stress as

$$\sigma_{eq} = \frac{\sigma_{Avg}}{\left(1+\frac{2R}{a}\right)ln\left(1+\frac{a}{2R}\right)} \tag{3.5}$$

Equations 3.2 and 3.3 are re-written using Equation 3.5 as

$$\sigma_r = \sigma_\theta = \sigma_{eq}ln\left(\frac{a^2+2aR-r^2}{2aR}\right) \tag{3.6}$$

$$\sigma_z = \sigma_{eq}\left[1 + ln\left(\frac{a^2+2aR-r^2}{2aR}\right)\right] \tag{3.7}$$

On the external surface, σ_z is equal to σ_{Avg} since the stress components σ_r and σ_θ become negligible at the centre of the neck as seen in Figure 3.4. In Equation 3.7, the term on the right-side denominator is the Bridgman's correction factor, B, which is implemented to offset the impacts of stress triaxiality present in the necking area as

$$B = \frac{1}{\left(1+\frac{2R}{a}\right)ln\left(1+\frac{a}{2R}\right)}$$ (3.8)

Equation 3.7 is rewritten in

$$\sigma_{eq} = B\sigma_{Avg}$$ (3.9)
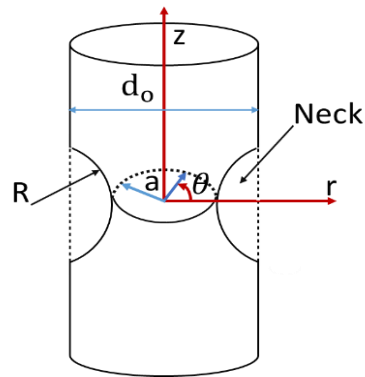
Figure 3.3.Tensile necking region in a round test specimen

(Source: Bao et al. [45])
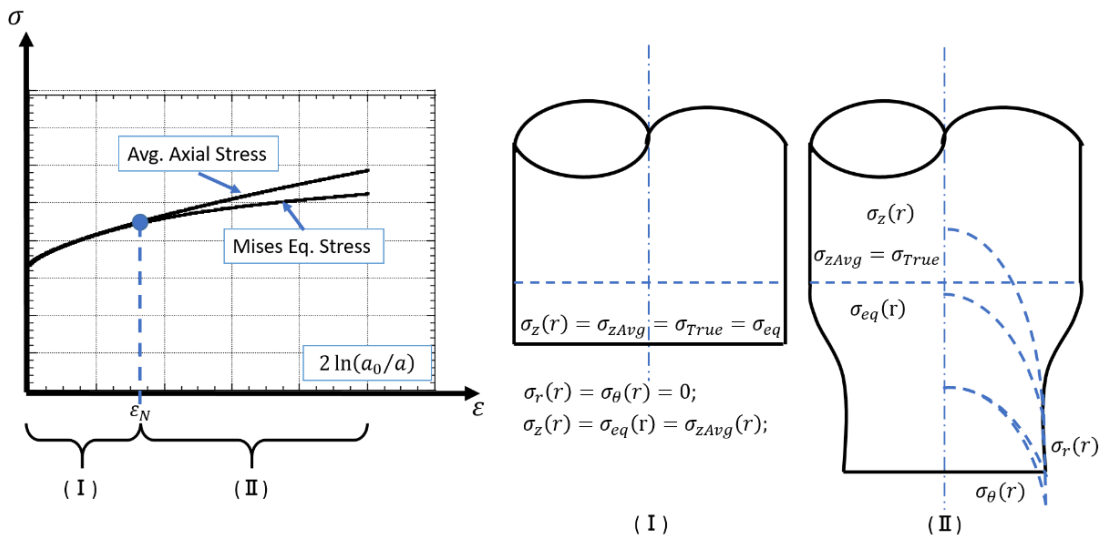
Figure 3.4. The average and equivalent stress-strain curves and the corresponding stress distributions

(Source: Mirone and Corallo [45])

Equations 3.4 and 3.5 give the following relation

$$\sigma_z = \sigma_e + \sigma_r = \sigma_e + \sigma_\theta \qquad (3.10)$$

Then, the stress triaxiality (σ^*) at the centre of a neck region in a tensile test specimen is determined using above relations as

$$\sigma^* = \frac{\sigma_h}{\sigma_{eq}} = \frac{1}{3} + \ln(1 + \frac{a}{2R}) \qquad (3.11)$$

where σ_h is the hydrostatic stress.

The equivalent strain (ε_{eq}) at the necking is written as

$$d\varepsilon_{eq} = \frac{\sqrt{2}}{3}\sqrt{[(d\varepsilon_z - d\varepsilon_r)^2 + (d\varepsilon_r - d\varepsilon_\theta)^2 + (d\varepsilon_\theta - \sigma d\varepsilon_z)^2]} \qquad (3.12)$$

The relation between the radial and axial strains for plastic deformation is

$$d\varepsilon_r = d\varepsilon_r = -0.5d\varepsilon_z \qquad (3.13)$$

Inserting Equation 3.13 into Equation 3.12 gives the equivalent strain as

$$\varepsilon_{eq} = \varepsilon_z = \ln\left(\frac{A_0}{A_i}\right) = 2\ln\left(\frac{a_o}{a_i}\right) \qquad (3.14)$$

where, a_o and a represent the initial and instantaneous radius (or necking radius) of test specimen, respectively.

The determination of the Bridgman's correction factor is challenging since after necking the R values must be determined through image analysis. While the equivalent stress after necking in the present study was calculated using the following practical relation

$$\sigma_e = \sigma_{at}MLR_{(\varepsilon_e - \varepsilon_n)} \qquad (3.15)$$

where $MLR_{(\varepsilon_e - \varepsilon_n)}$ is a coefficient that converts the average stress to the equivalent stress, similar to Bridgman's coefficient, and given as[46]

$$MLR_{(\varepsilon_e - \varepsilon_n)} = 0.9969 - 0.6058(\varepsilon_e - \varepsilon_n)^2 + \cdots \qquad (3.16)$$
$$0.6317(\varepsilon_e - \varepsilon_n)^3 - 0.2017(\varepsilon_e - \varepsilon_n)^4$$

where ε_n is the true plastic strain at necking. The effectiveness of the MLR correction method was confirmed over 15 different isotropic metals as depicted in Figure 3.5. In the same graph, the ratio of the equivalent stress to the average true stress (σ_{eq}/σ_{Avg}) is drawn as function of ($\varepsilon_{eq} - \varepsilon_N$). A polynomial fit to the data in Figure 3.5 yields $MLR_{(\varepsilon_e - \varepsilon_n)}$ as function of ($\varepsilon_{eq} - \varepsilon_n$).
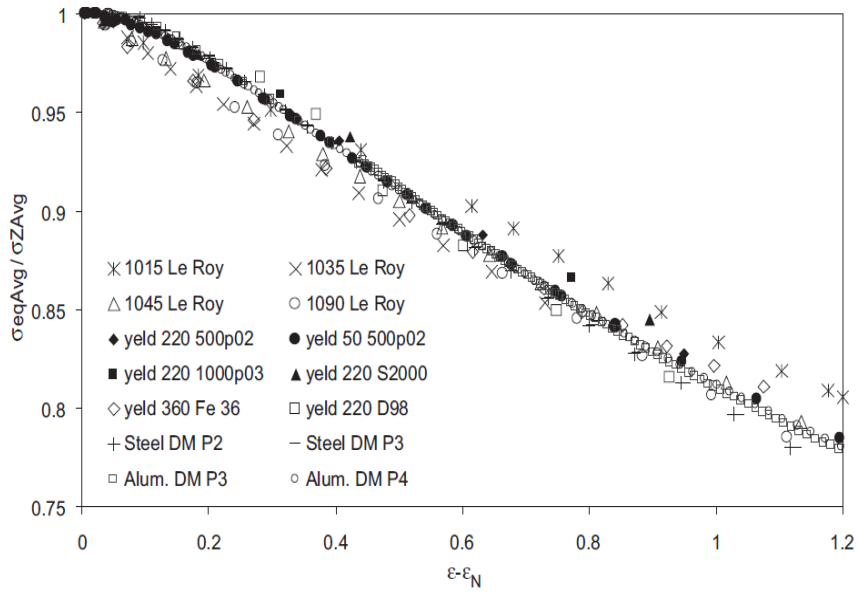
Figure 3.5. The average equivalent stress to average true stress ratio as a function of the normalized plastic strain

(Source: Mirone [46])

A schematic and a picture of the employed SHTB apparatus are presented in Figures 3.6(a) and (b), respectively. The SHTB apparatus comprised a tubular striker with a length of 500 mm, along with incident and transmitted bars, each measuring 2410 mm in length and 20 mm in diameter. The bars and tube were made of 316L alloy. The details

of the used SHTB set-up are given elsewhere[47]. Briefly, the impact of the striker to the stepped end of the incident bar creates a tension wave which propagates to the incident bar (Figures 3.6(a) and (b)). The tension on the incident bar is partly reflected back from the specimen-bar interface (the specimen was screwed to the bars) as the compression wave to the incident bar and partly transmitted to the transmitter bar as tension wave depending on the mechanical impedance difference between the specimen and bar.
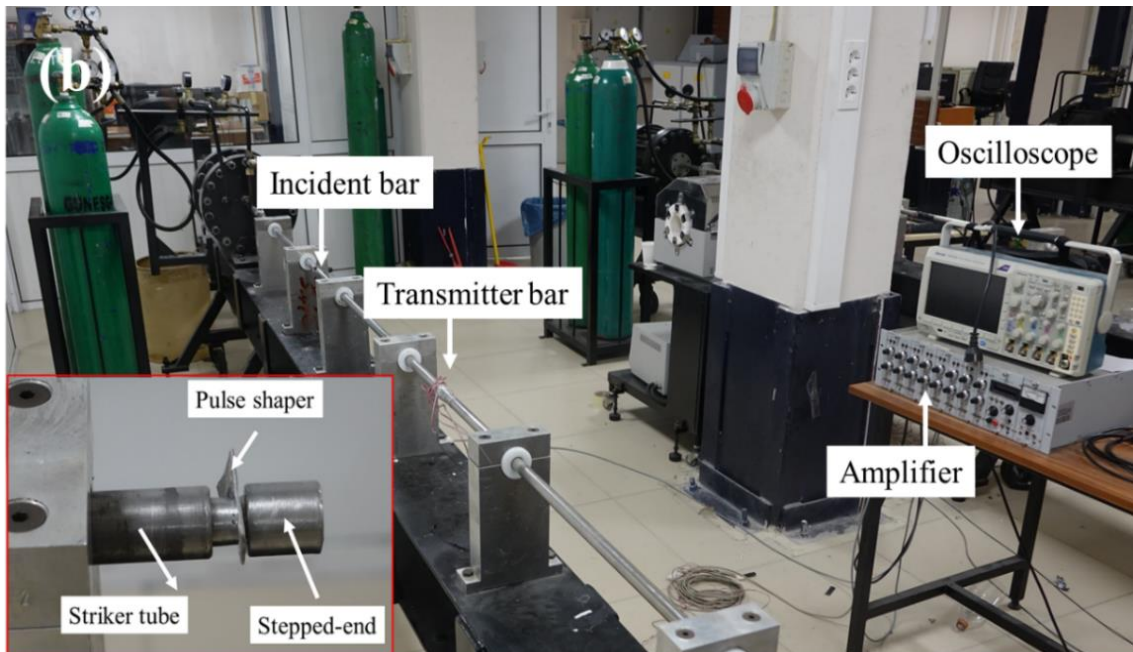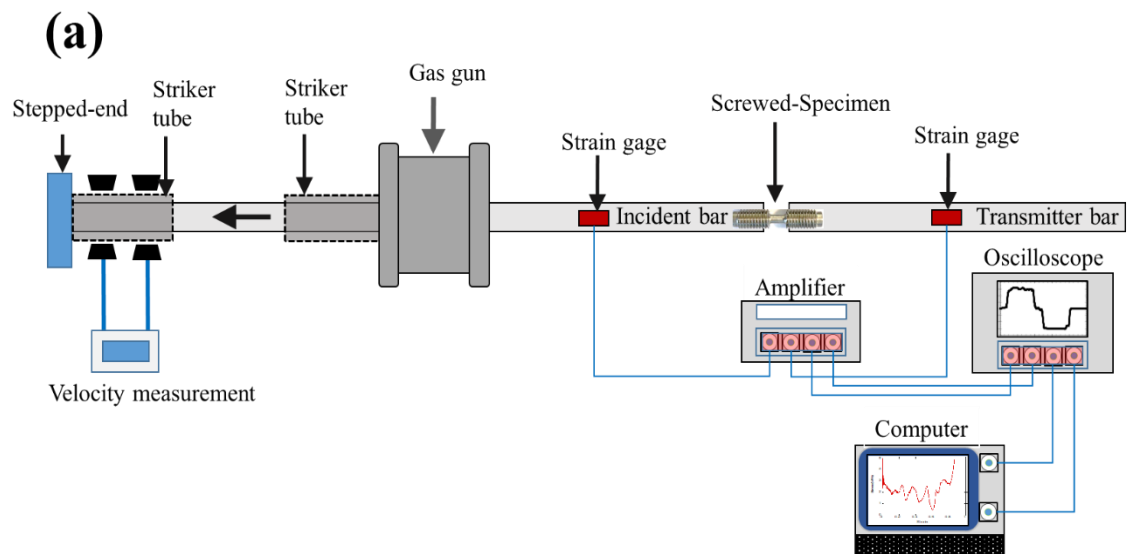
Figure 3.6. SHTB set-up (a) schematic and (b) picture

The elastic modulus, density and yield strength of 316L bars are 193 GPa, 8000 kg m^{-3} and 300 MPa, respectively. Stresses on the bars were measured by a full Wheatstone-bridge configuration of 350 Ω foil strain gages. The sample deformation in the SHTB tests was recorded using a FASTCAM high speed camera at 20000 fps. After recording the waves using an oscilloscope and amplifier, the strain (ε_s), stress (σ_s) and strain rate ($\dot{\varepsilon}_s$) of specimen were calculated using the following relations,

$$\varepsilon_s(t) = -\frac{2C_b}{L_s} \int_0^t \varepsilon_R(t)\, dt \tag{3.17}$$

$$\sigma_s(t) = \frac{A_b}{A_s} E_b \varepsilon_T(t) \tag{3.18}$$

$$\dot{\varepsilon}_s(t) = -\frac{2C_b}{L_s} \varepsilon_R(t) \tag{3.19}$$

where L_s, A_b, A_s, E_b, C_b and t represent the specimen length, the cross-sectional area of the bar, the cross-sectional area of the specimen, the elastic modulus of the bar, the elastic wave velocity in the bar, and time, respectively. ε_R and ε_T correspond sequentially to the reflected and transmitted strains.

The tensile tested and untested 304 specimens were cut in a water-cooled precision diamond saw for metallographic analyses. Diamond solution polished specimens were then etched in order to reveal the microstructure (10% HNO3, 20% HCl and 20% Glycerol) under optical microscope (Meiji IM7 100) and scanning electron microscope (SEM, FEI Quanta 205 FEG and Philips XL 30SFEG). The Vickers micro hardness tests were on the mounted specimens in a SHIMADZU HMV-2 test machine at 9.8 N for 10 s dwell time.

3.2. Quasi-Static Tension Test Models

Three-dimensional models of tension test specimens were created in SolidWorks. After meshing in Hypermesh, the models were exported to LS-PrePost to define the material models and the boundary conditions. All models were implemented in LS-Dyna

Solver. In all models, the test specimen sizes and cross-head speeds were the same as the experimental test specimen sizes and cross-head speeds.
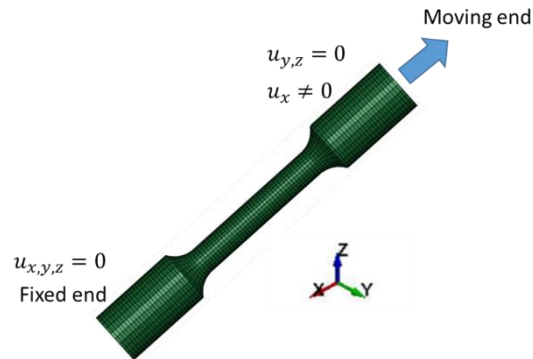
Figure 3.7. Quasi-static tension test model with σ^*=0.33

The quasi-static tension model of unnotched specimen, σ^*=0.33, is shown in Figure 3.7. The fixed and moving end sections of the test specimen at which the grips hold the specimen were modelled using the single point constraint (SPC) nodes. In these ends, the SPC nodes were fully constrained except $u_x \neq 0$ in the loading axis (Figure 3.7). The cross-head speed of the moving end was defined by the PRESCRIBED_MOTION_SET in the x-direction.

Mesh (mm)	σ^*=0.33	σ^*=0.56	σ^*=1.02
0.2			
0.3			
0.4			
0.5			

Figure 3.8. Tension test models with different mesh sizes and stress triaxialities

All tension test models were meshed using the constant stress Hex solid elements. A mesh sensitivity analysis was also performed using 0.2, 0.3, 0.4, 0.5 mm mesh sizes. Figure 3.8 shows the investigated tension test models with four different mesh sizes and three different stress triaxialities.

Since CPU time for the quasi-static test solutions were relatively long, a mass scaling was applied. The mass scaling factor was determined 1000 by following the method given elsewhere[48]. At this mass scaling factor, the kinetic energy change was found to be substantially lower than the internal energy change. Furthermore, the forces at both ends of the numerical tension test specimen were checked after the simulations and found to be very similar, confirming the quasi-static loading condition.

3.3. Constant Speed High Strain Rate Tension Test Model

During the SHTB testing, the strain rate varied with strain; hence, an average strain rate was calculated for each test. The corresponding displacement rate was then calculated and used in the models in order to simulate the high strain rate tests as similar with the constant displacement rate quasi-static tension tests. The gage length was however smaller in the high strain rate models and also experimental tests, 5 mm. As seen in Figure 3.9, one end of the high strain rate test model specimen is fixed (similar to quasi-static tension test model) and the specimen is pulled at the other end in the loading direction. These constant speed high strain rate tension test models were implement using the 0.2 mm mesh size and again using the constant stress Hex solid elements. The boundary conditions of the constant speed high strain rate tension test specimen models were the same with those of the quasi-static tension test specimen models.
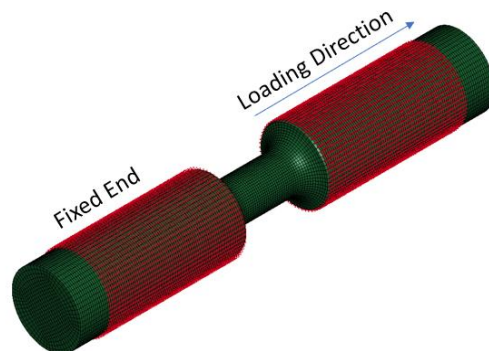
Figure 3.9. Constant speed high strain rate tension test model

3.4. SHTB Tension Test Model

The used quarter SHTB test model is depicted in Figure 3.10. The model is consisted of the incident and transmitter bar and the test specimen. The experimental test specimen was tightly fixed by screwing its ends to the ends of 316L bars, similarly the model specimen ends were fixed to the bars using the TIED_SURFACE_TO_SURFACE contact between them. The 316L incident and transmitted bars, 2410 mm in length and 20 mm in diameter, were modeled as the elastic material. The elastic modulus, density, Poisson's ratio and yield strength were taken the same as the experiments and sequentially 193 GPa, 8000 kg m^{-3}, 0.29 and 300 MPa.

In the models, the experimental incident stress pulse was imposed (at the same location with the strain gage) on the incident bar using the CURVE card in the DEFINE option. The bars and the specimen were modelled using the constant stress Hex solid elements. Since the selected element type is a reduced integration element, the Hourglass type was set to 5 in order to prevent hourglass. For termination, the ENDTIME value in the CONTROL card was set to 2500 μs. To model the entire SHTB in quarters, the symmetrical faces were fully constrained using the Boundary option and the SPC option. The solid elements having a similar size with the used strain gages were selected at the location of the strain gages (HISTORY_SOLID). The stress and strain on the bars were read from these HISTORY_SOLID elements.
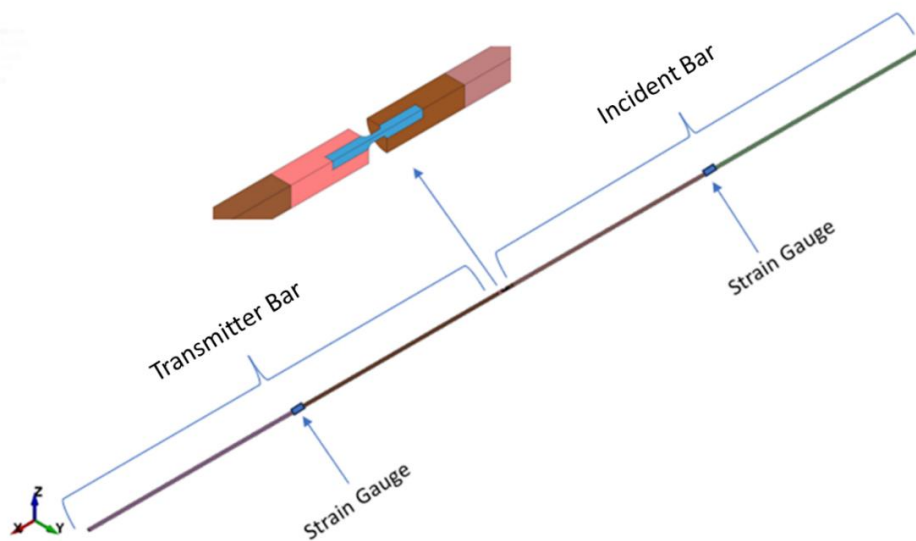
Figure 3.10. Quarter SHTB model

3.5. Ballistic Tests and Models

In a previous study, ballistic tests were performed on the monolithic and B_4C-coated 304 plates using 7.62 mm APM2 projectiles at a velocity of ~800 m s^{-1} [49]. The ballistic tests were performed using NATO Stanag 4569 standard. The shots were fired from a distance of 30 meters with G3 bullets. [49]

These tests were modelled in order to verify the fidelity of the developed flow stress and damage models of SS 304. A drawing of the used 7.62 mm APM2 projectile, taken from taken from the reference[50], is shown in Figure 3.11.

Figure 3.11. Bullet in the ballistic model

(Source: Flores-Johnson et al. [50])

The bullet model is consisted of a brass jacket (blue), a hardened steel core (white in the inside) and a lead filler (gray at the front). The flow stress of the bullet was modelled using the modified JC flow stress model and the damage was modeled using the Cockcroft-Latham damage model. Parameters of both models are given in the reference[50] and also tabulated in Table 3.1.

The quarter models of monolithic and B_4C-coated 304 plate ballistic tests are shown in Figures 3.12(a) and (b), respectively. The total thicknesses of 304 plate and B_4C coating layer were sequentially 5 and 0.05 mm. The bullet impact area on plates (15 mm in diameter) was meshed with the 0.2 mm Hex elements. The mesh sizes in all other locations were biased by 0.3 mm. ELFORM 1 was used as the element formulation with the hourglass type 4. The motion of the nodes at the plate edges were fully constrained. ERODING_SINGLE_SURFACE card was selected as the contact between the bullet and the target and SOFT=2 was used. In eroding contact, elements were deleted according to material failure criteria.

Table 3.1. The modified JC flow stress and the Cockcroft-Latham damage model for the bullet

(Source: Flores-Johnson et al. [50])

Material	Yield Strength	Strain Hardening		Strain Rate Hardening		Temperature Softening			CL
	A(MPa)	B(MPa)	N	$\dot{\varepsilon}_0$ (s^{-1})	C	$T_r(K)$	$T_m(K)$	m	W_{cr}
Brass Jacket	206	505	0.42	5×10^{-4}	0.01	293	1189	1.68	914
Hard. Steel Core	1200	50000	1	5×10^{-4}	0	293	1800	1	-
Lead Cap	24	300	1	5×10^{-4}	0.1	293	760	1	175

Another feature of the ERODING_SINGLE_SURFACE card was that the element was deleted due to negative volume. The SLSFAC value was added by opening the CONTROL_CONTACT card to calculate the stiffness value for SOFT 2. Since B$_4$C was coated on stainless steel, the joints of the two parts were done by merging dupnodes. Boron carbide was modelled using the MAT_JOHNSON_HOLMQUIST CERAMICS (MAT 110) card (JH-2). The material model parameters of B$_4$C were taken from the reference[51] and tabulated in Table 3.2. The EOS is not required in LS-DYNA for the MAT 107 while the Mie-Gruneisen EOS was used for SS 304. The parameters used in the EOS card are further tabulated in Table 3.3.

Table 3.2. JH-2 model parameters of B$_4$C

(Source: Holmquist and Johnson [51])

ρ_0 (kg m^{-3})	G(GPa)	A	B	C	M
2510	197	0.927	0.7	0.005	0.85
N	EPSO (s^{-1})	T (GPa)	SFMAX	HEL (GPa)	P_{HEL} (GPa)
0.67	1	0.26	0.2	19	8.71
BETA	D$_1$	D$_2$	K$_1$(GPa)	K$_2$ (GPa)	K$_3$ (GPa)
1	0.001	0.5	233	-593	2800

Table 3.3. Parameters of the Mie-Gruneisen EOS card of SS 304

Material	C (m s^{-1})	S_1	S_2	S_3	γ_0	a
SS 304	4569	1.49	0	0	2.17	0

(a)　　　　　　　　　　　　**(b)**
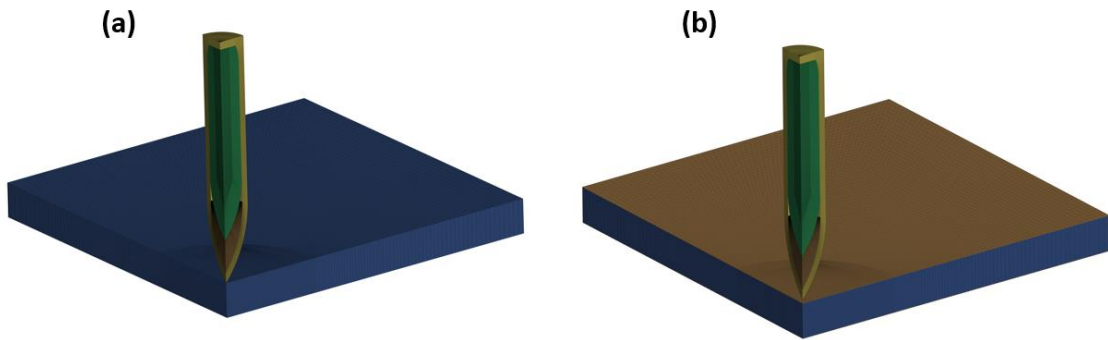
Figure 3.12. The quarter model of the ballistic test (a) monolithic 304 plate and (b) B$_4$C-coated 304 plate

CHAPTER 4

RESULTS AND DISCUSSION

4.1. Quasi-static Stress-strain Behaviour

Figure 4.1(a-c) shows the true stress-strain curves of three specimens tested at the strain rates of 10^{-3}, 10^{-2} and 10^{-1} s^{-1}, respectively. On the same curves, the average true-stress-strain curves (video stress-strain curves) are also shown (circles). As is seen, the average true stresses and true stresses are very much similar to each other until about the necking. Also noted that, the fracture strains marked on the average stress-strain curves are much greater than the necking strains. For example, the necking strain is about 0.39 while the fracture strain is as high as 0.94 for the tests at 10^{-3} s^{-1} as seen Figure 4.1(a). This confirms a very ductile fracture behaviour of the tested SS 304 alloy.

The representative stress-strain curves at three different quasi-static strain rates are further shown in Figure 4.1(d) for comparison. As seen in the same figure, the flow stress values at $1x10^{-3}$ s^{-1} test are lower than those at $1x10^{-2}$ and $1x10^{-1}$ s^{-1} test until about 0.2 strain while the flow stress values at $1x10^{-3}$ s^{-1} tests exceed those at $1x10^{-2}$ and $1x10^{-1}$ s^{-1} test after 0.2 strain. This noted behaviour agrees with the previous studies on SS 304 alloy[18, 23, 29] and is caused by the formation of a higher volume fraction of martensitic transformation at $1x10^{-3}$ s^{-1} test than at $1x10^{-2}$ and $1x10^{-1}$ s^{-1} tests. As will be elaborated later, the facture strains at $1x10^{-3}$ s^{-1} tests are very much similar to those at $1x10^{-2}$ tests but higher than those at $1x10^{-1}$ s^{-1} tests. The deformation images of quasi-static tensile test specimens at $1x10^{-3}$, $1x10^{-2}$ and $1x10^{-1}$ s^{-1} before testing, after necking and after fracture are shown in Figures 4.2(a-c), respectively. As seen in the same pictures, necking starts to initiate at the midsections of test specimens in all tests. Comparably large plastic strain evolution is seen in the necked region until about the facture. It is further noted that the strain at which the necking initiates is highest in the tests at $1x10^{-3}$ s^{-1}. On the other side, nearly a diffuse necking is seen at three strain rates. However, the necking is seen to be more diffusive in the specimens tested at lower strain rates than the specimens tested at $1x10^{-1}$ s^{-1}. The facture strains of three specimens at each strain rate were measured from the fractured section diameters.
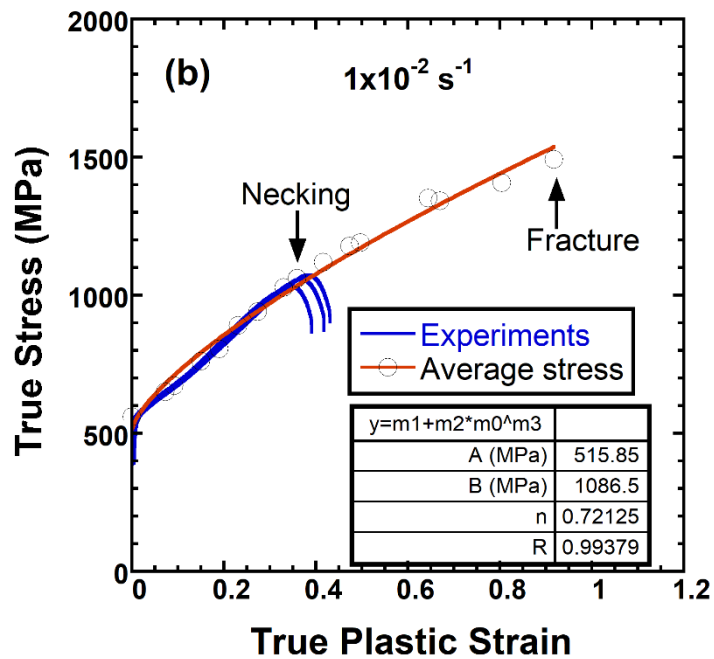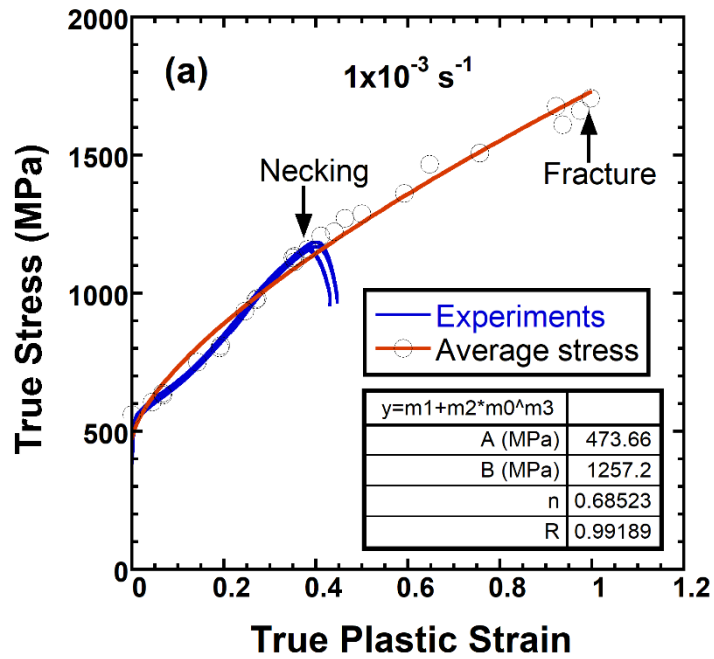
Figure 4.1. Experimental true stress-strain and average true stress-strain (video-read stress-strain) curves at (a)1×10^{-3}, (b)1×10^{-2} and (c) 1×10^{-1} s^{-1} and (d) the selected curves at three different strain rates
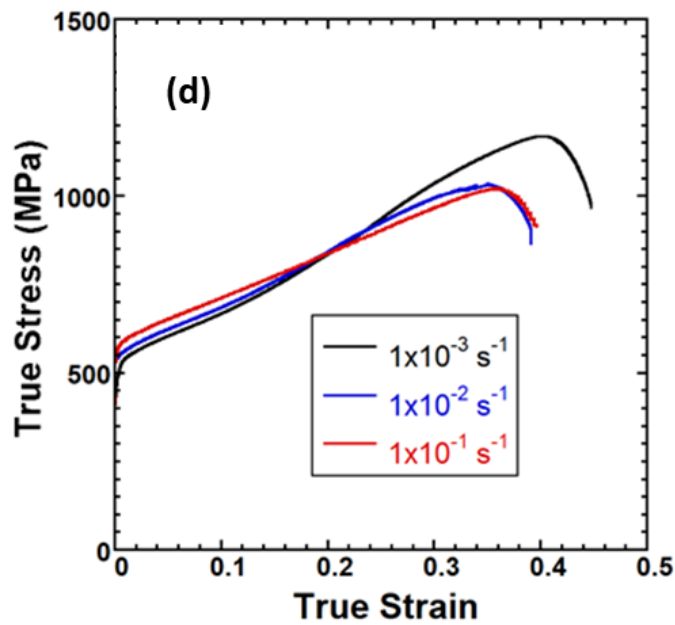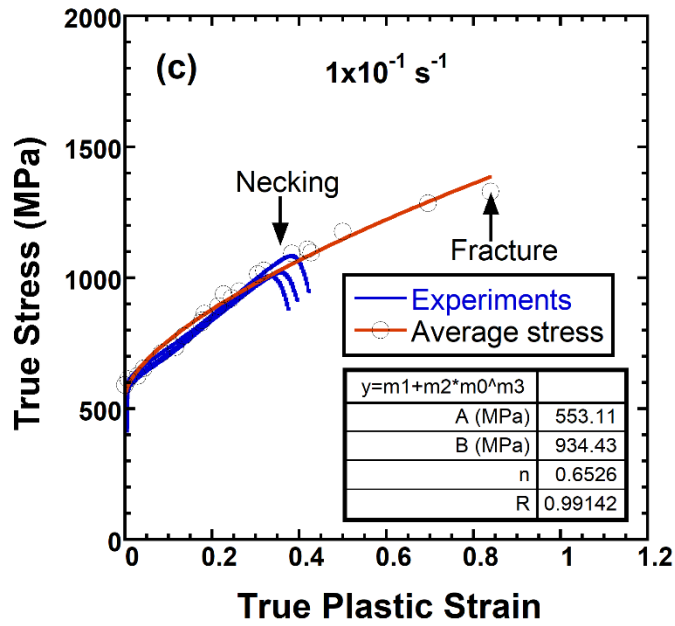
Figure 4.1 (cont.)

The highest true plastic fracture strains are found in the specimens tested at 1×10^{-3} s^{-1} (0.94, 0.99 and 0.9) and at 1×10^{-2} (0.95, 0.94 and 0.97). The fracture strains in the specimen tested at 1×10^{-1} s^{-1} are relatively lower (0.83, 0.85 and 0.82). These results agreed with the previous studies[35] and the facture strain increased as the volume faction of martensite increased. An S-shape stress-strain curve is further seen in Figure 4.1(d) in the tests at 1×10^{-3} s^{-1} which was also seen in the previous studies [15, 29] and ascribed to

higher rate of martensitic transformation at this strain rate. Furthermore, the stress-strain curves are also fitted with the JC stress equation. The determined JC stress parameters are further listed in Figures 4.1(a-c) for each strain rate.
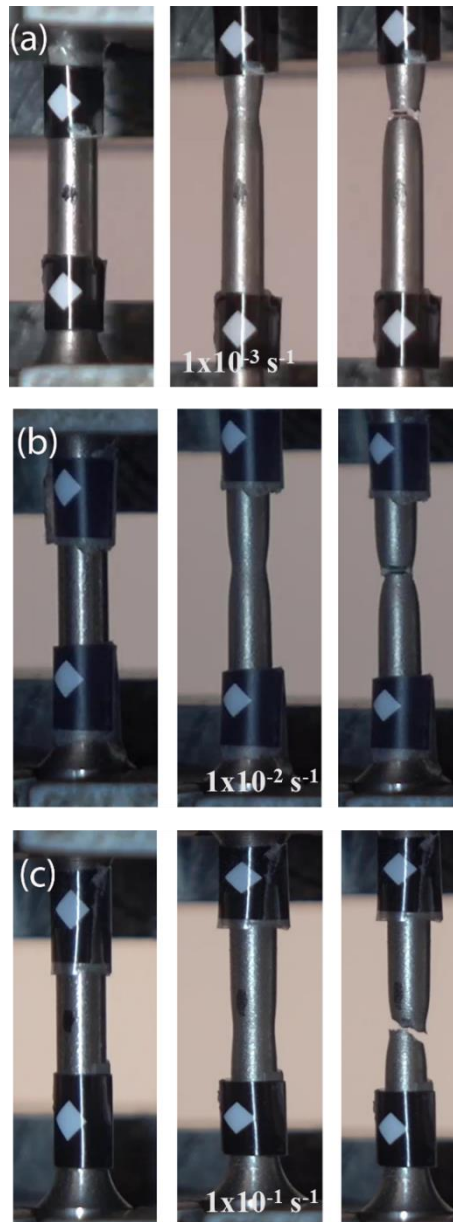
Figure 4.2. Deformation pictures of tension test specimens before testing, after necking and after the facture: (a) $1x10^{-3}$, (b) $1x10^{-2}$ and (c) $1x10^{-1}$ s^{-1}

The engineering stress-displacement curves of the specimens with 0.33, 0.56 and 1.02 stress triaxialities at 10^{-3} s^{-1} strain rate re shown together in Figure 4.3. As is seen in the same figure, the ultimate tensile strength increases from 793 MPa to 1011 MPa, as

the stress triaxiality increases from 0.33 to 1.02. On the other side, the displacement at fracture decreases significantly with increasing stress triaxiality. The deformation images of the tested specimens with 0.56 and 1.02 stress triaxialities before testing, at the peak stress, just before the fracture and after the fracture are shown in Figures 4.4(a-d) and Figures 4.5(a-d), respectively. In both specimens, the localized deformation occurs at the notch section and the specimens fracture at these highly deformation localized regions. The displacement of the notched region is also noted in the same figures to be larger in the test specimen with 0.56 stress triaxiality than the specimen with 1.02 stress triaxiality.
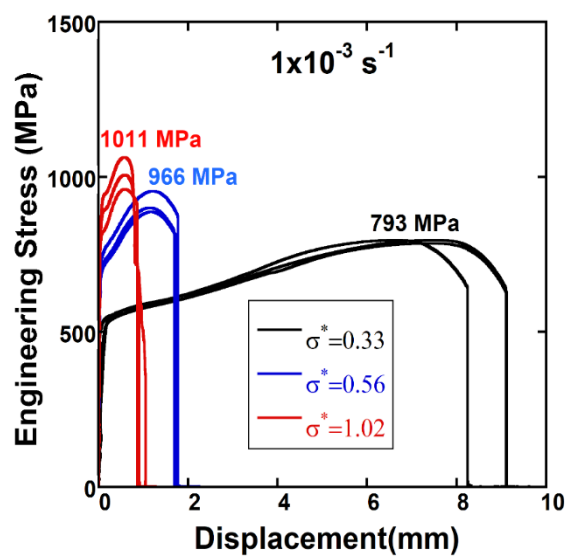
Figure 4.3. Engineering stress-displacement curves of the tensile specimens at three different stress triaxialities
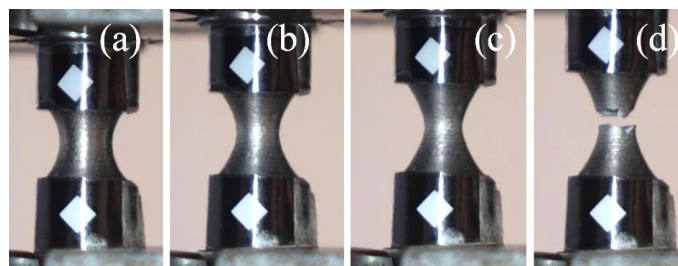
Figure 4.4. The deformation pictures of a test specimen with 0.56 stress triaxiality (a) before testing, (b) at the peak stress, (c) just before the fracture and (d) after the fracture
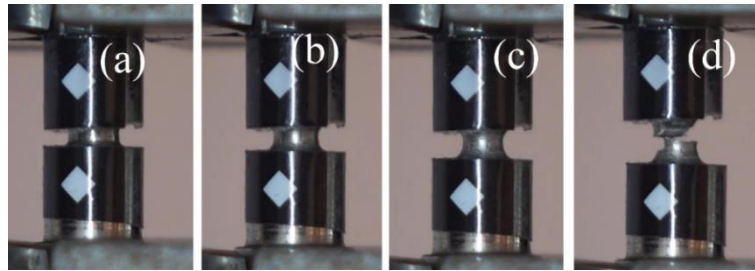
Figure 4.5. The deformation pictures of a test specimen with 1.02 stress triaxiality (a) before testing, (b) at the peak stress, (c) just before the fracture and (d) after the fracture

True plastic fracture strains were determined from the video records for each specimen tested. Table 4.1 tabulates true plastic fracture strains of three tests performed at three different stress triaxialities together with their averages. With increasing stress triaxiality, the average plastic fracture strain is noted to decrease. The average fracture strain decreases from 0.94 to 0.44 when the stress triaxiality increases from 0.33 to 1.02. This corresponds to about 50% decrease in the fracture strain.

Table 4.1. True plastic fracture strains and average values at three different stress triaxialities

Specimen no	Plastic fracture strain $\sigma^*=0.33$	Plastic fracture strain $\sigma^*=0.56$	Plastic fracture strain $\sigma^*=1.02$
1	0.940	0.741	0.399
2	0.989	0.727	0.452
3	0.900	0.693	0.464
Average	0.94	0.72	0.44

4.2. High Strain Rate Stress-Strain Behaviour

Figure 4.6(a) shows the typical SHTB strain gage readings of a test performed at an average strain rate of 2900 s^{-1}. At this average strain rate, the specimen fractures in the second loading. In the first loading, the specimen is deformed until about 0.25 strain. In the second loading as shown in Figure 4.6(a), the returning reflected wave loads the specimen second time, leading to the fracture.
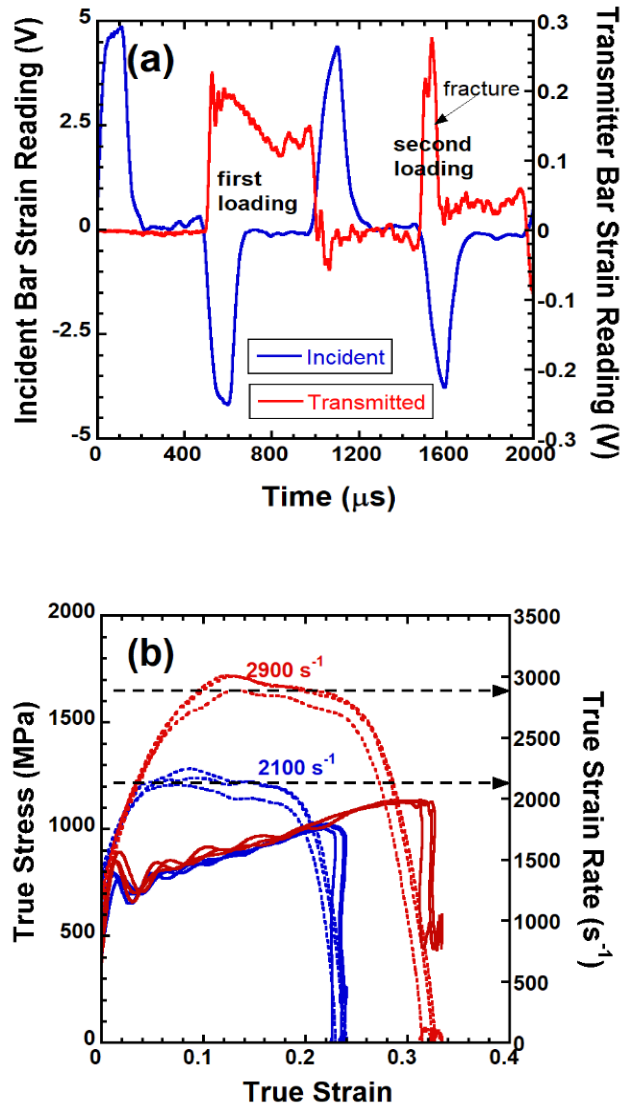
Figure 4.6. (a) SHTB readings of a test at 2900 s^{-1} showing repeated loading and the fracture of specimen in the second loading and (b) true stress-strain curves at 2100 and 2900 s^{-1}

The specimens tested at 2100 s^{-1} also fractured in the second loading. Figure 4.6(b) shows true stress-strain and true strain rate-strain curves of three tests performed at the average strain rates of 2100 s^{-1} and 2900 s^{-1}. The average strain rates were determined as the maximum strain rates in the tests and shown with the dotted lines in Figure 4.6(b). Figures 4.7(a-d) show the deformation pictures of a tensile specimen in the SHTB at 2900 s^{-1} before testing, before necking and after necking in the first loading and after the fracture in the second loading. The necking already forms in the first loading, showing the specimen is heavily deformed in the first loading. The increased transmitter bar stress

in the second loading as compared to the first loading will be discussed together with the modelling results in the next sections. The true plastic fracture strains in the SHTB tests at 2900 s^{-1} are further noted to be lower than those of the quasi-static tests and were measured for three tests as 0.7, 0.705 and 0.71.
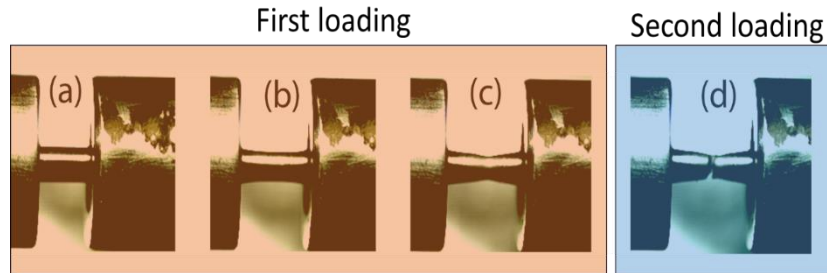
Figure 4.7. Deformation pictures of the tensile specimen in the SHTB at 2900 s^{-1} (a) before testing, (b) before necking and (c) after necking in the first loading and (d) after the fracture in the second loading

4.3. Mechanical Properties and Equivalent Stress Calculations

Table 4.2 tabulates the average mechanical properties of the tested SS 304 at different strain rates. The yield strength as noted in the same table increases with increasing strain rate from 502 MPa at 10^{-3} s^{-1} to 600 MPa at 2900 s^{-1} while ultimate tensile strength (UTS) decreases as the quasi-static strain rate increases, from 1163 MPa at 10^{-3} s^{-1} to 1013 MPa at 10^{-1} s^{-1}. While the UTS increases at the dynamic strain rate, 1114 MPa at 2900 s^{-1}, over those at 10^{-2} to 10^{-1} s^{-1} but the value is below the UTS at 10^{-3} s^{-1}. The percent elongation and equivalent plastic fracture strain decrease as the strain rate increases as tabulated in the same table.

Figures 4.8(a) and (b) show the typical average true stress-true strain and work hardening-plastic true strain curves at different strain rates, respectively. The stress-strain and work hardening-strain curves are composed of three distinct deformation regions marked as I, II and III in the same figures. Region I continuous until about 0.1 strain and it represents a rapid reduction in the work hardening associated with the dislocation motion leading to the shear band formation.

The martensite starts to form after about 0.1 strain in the Region II with an increase in the work hardening rate, the intensity of which varies with the strain rate. At increasing strain rates, the martensite formation is expected to be hindered by the specimen heating (increased SFE) which results in a reduced work hardening in the Region II. In Region III, the deformation switches into the dislocation glide again and the work hardening rate decreases accordingly.

Table 4.2. Average mechanical properties of SS 304 at different strain rates

Strain rate (s^{-1})	10^{-3}	10^{-2}	10^{-1}	2900
Yield strength (MPa)	502	516	553	600
UTS (MPa)	1163	1030	1013	1114
Percent elongation	43	42.5	40.3	31.2
Equivalent plastic fracture strain	0.94	0.95	0.83	0.70
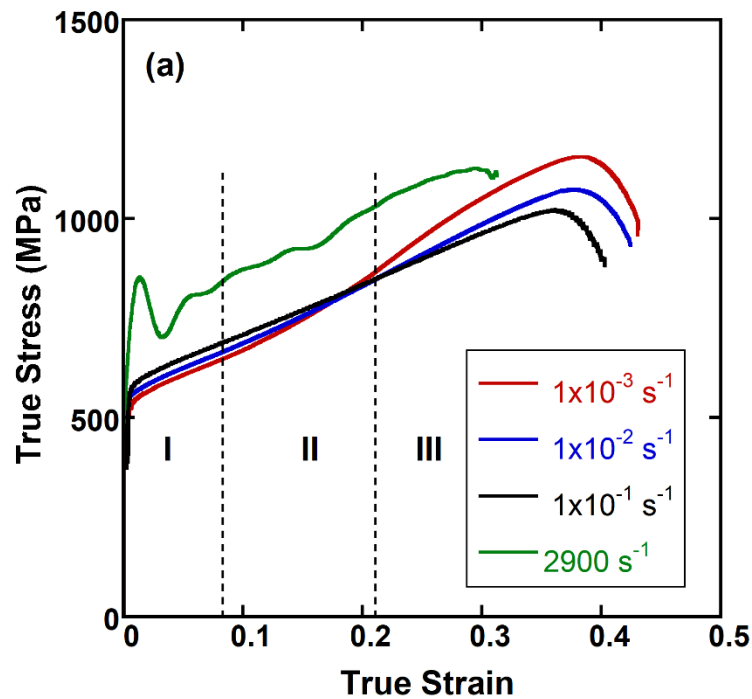
Figure 4.8.Typical (a) stress-strain and (b) work hardening-strain curves at 1x10-3, 1x10^{-2}, 1x10^{-1} and 2900 s^{-1}

Figure 4.8 (cont.)

High strain rate promotes the martensite formation by impeding the dislocation motion and it also increases the specimen heating due to prevailing adiabatic conditions. As is noted in Figure 4.8(b), the work hardening rate in the test at 2900 s^{-1} is higher than that of the test at 1×10^{-3} s^{-1} at low strains (Region I). The work hardening rates at 2900 s^{-1} and 1×10^{-3} s^{-1} are very much similar in the half part of the Region II while the deformation at 2900 s^{-1} switches into Region III at an earlier strain (marked as a in Figure 4.8(b)) than that of the test at 1×10^{-3} s^{-1}. This behaviour is ascribed to the adiabatic heating of the specimen tested at the highest strain rate, 2900 s^{-1}. With adiabatic heating, the SFE increases and the strain hardening curve will change earlier.

The JC flow stress equation ($A + B\varepsilon_{ep}^{n}$) was fitted with the average true stress-true plastic strain curves at 1×10^{-3}, 1×10^{-2}, 1×10^{-1} and 2900 s^{-1}. The resultant fitted curves and fitted parameters are shown in Figure 4.9. The MLR correction was then performed on these fitted equations by entering the average necking strains into the MLR equation at each strain rate. Figure 4.10 shows the fitted average stress-strain curves with those of the equivalent stress-strain curves determined by the MLR correction.

64
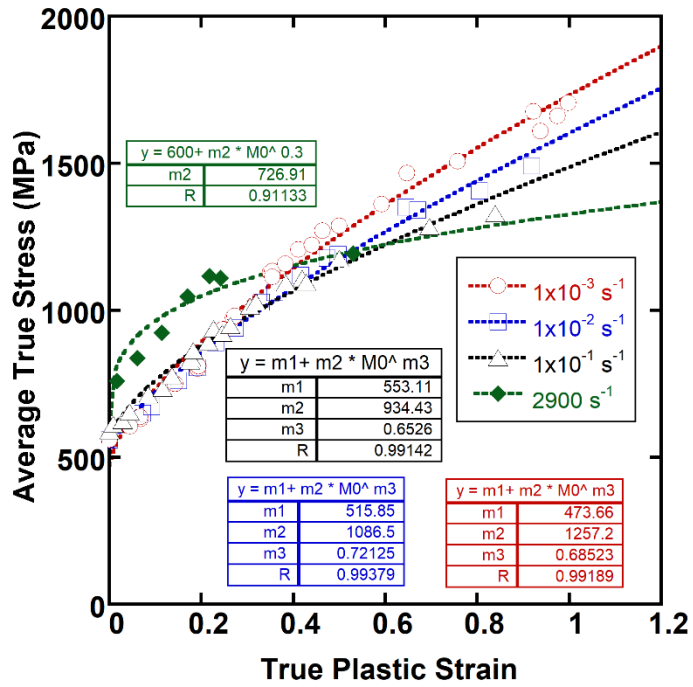
Figure 4.9.Average true stress-plastic strain curves at 10^{-3}, 10^{-2}, 10^{-1} and 2900 s^{-1}
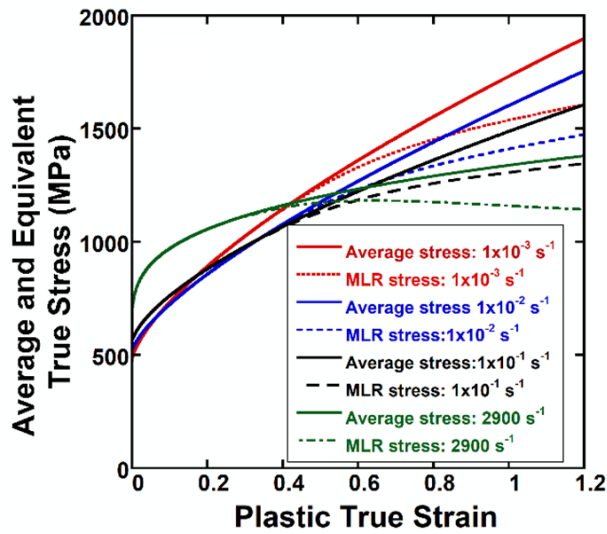
Figure 4.10.Average and equivalent true stress-plastic strain curves 1×10^{-3}, 1×10^{-2}, 1×10^{-1} and 2900 s^{-1}

4.4. Johnson and Cook Flow Stress Parameters

Figure 4.11 illustrates the results of fitting the equivalent stress-strain curve (MLR) with the Johnson-Cook (JC) flow stress equation at the reference strain rate of 10^{-}

^{3} s^{-1}. The fitting process yields the following optimized parameter values: A=300 MPa, B=1300 MPa and n=0.4728. In the same figure, several curves are displayed for comparison, including the experimental true stress-true plastic strain curve up to the necking point, the average true stress-true plastic strain curve, and the JC flow stress-strain curve fitted to the average stress-strain data. While the fitted MLR stress curve exhibits minor deviations from the experimental stress-strain data prior to necking, it demonstrates strong agreement with the average stress-strain curve beyond the necking region. This agreement indicates the effectiveness of the MLR fitting approach in capturing post-necking material behavior. The strain rate sensitivity parameter of the JC flow stress equation was determined by analyzing the flow stresses from both quasi-static and high strain rate tests at a strain level of 0.1. This strain level was specifically chosen because, at higher strains, adiabatic heating effects significantly influenced the flow stresses, while at lower strains, the SHTB results showed notable oscillations.

By focusing on a strain of 0.1, these confounding factors were minimized, ensuring a more accurate and reliable determination of the strain rate sensitivity parameter. This strain level was chosen specifically because it is less influenced by the adiabatic heating effects at higher strains and the oscillations observed at lower strains, which can distort the data. As a result, this approach provides a clearer representation of the material's intrinsic strain rate sensitivity. The results of the fitting process, shown in Figure 4.12, yield a calculated strain rate coefficient value of approximately 0.019. This value is in excellent agreement with a previous study, which reported a slightly higher value of 0.022 [35], providing further validation for the accuracy of the fitting procedure used in this study.

However, it is noteworthy that the calculated value is somewhat lower than the value of 0.0321[31] documented in another independent study. This discrepancy may arise from differences in material composition, experimental setup, or testing conditions between the studies. Variations in the alloying elements, heat treatment processes, or strain rates applied could all influence the strain rate sensitivity, contributing to the observed differences. These observations not only reinforce the necessity for precise control over experimental conditions but also highlight the importance of comprehensive material characterization when comparing constitutive model parameters across different studies. In this regard, further research is needed to refine the understanding of strain rate

sensitivity, particularly under high-strain rate conditions, to improve the accuracy of predictive models for various materials.
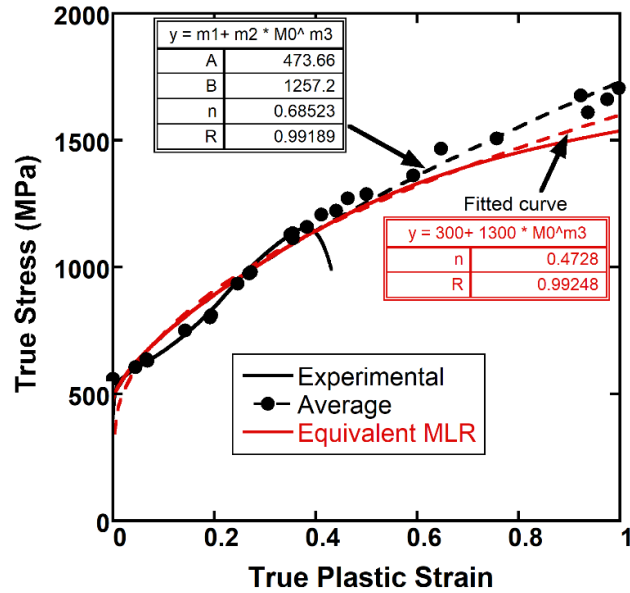
Figure 4.11. Equivalent stress-strain curve determined by the MLR together with the experimental and average stress-strain curves and fitted equivalent stress-strain curve with $A + B\varepsilon_{ep}^{n}$ at 10^{-3} s^{-1}
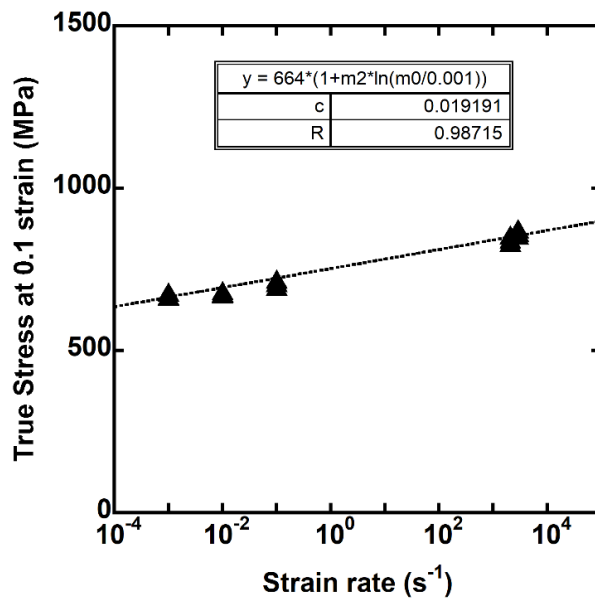
Figure 4.12. The strain rate sensitivity parameter determined from the flow stresses at 0.1 strain

4.5. Johnson and Cook Damage Parameters

Figure 4.13 (a) shows the variation of true plastic fracture strain with the stress triaxiality at 10^{-3} s^{-1} strain rate (reference strain rate), and at 25°C (reference temperature). The data in the same graph are fitted with $\varepsilon_f = [D_1 + D_2 \exp(D_3 \sigma^*)]$ to determine the values of D_1, D_2 and D_3 parameters. In the first fit, D_3 value is taken as 1.5 and the D_1 and D_2 values are determined and found 0.16798 and 1.2736, respectively. The simulations in LS DYNA using a mesh size of 0.2 mm and above damage parameters at the stress triaxialities of 0.33, 0.56 and 1.02 at 10^{-3} s^{-1}, give the true plastic fracture strains of 0.88, 0.66 and 0.41, respectively. The true plastic facture strains in the simulations were calculated using Equation 3.14.
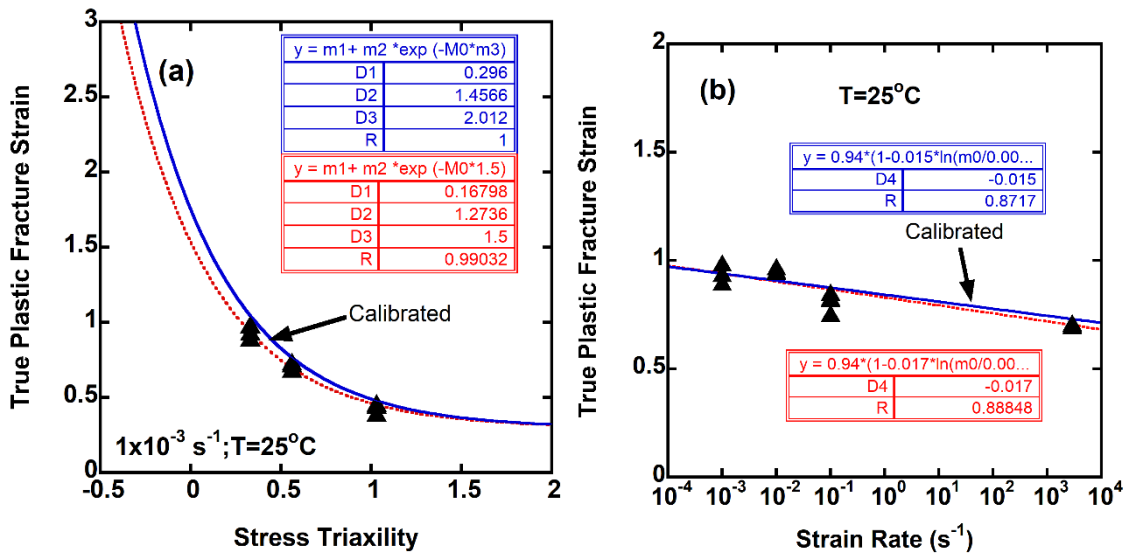
Figure 4.13. The predicted (a) D_1, D_2 and D_3 and (b) D_4 parameters in the damage model

The average experimental facture strains are however 0.94, 0.74 and 0.44 (see Table 4.1) at the stress triaxialities of 0.33, 0.56 and 1.02. The fitting process was re-done to match the experimental values (called *calibrated* in Figure 4.13(a)) and D_1, D_2 and D_3 values were determined 0.296, 1.4566 and 2.012, respectively. The numerical fracture strain values with these new parameters were found 0.96, 0.72, 0.47 at the stress triaxialities of 0.33, 0.56 and 1.02, respectively. Figure 4.13 (b) shows the variation of the true plastic fracture strain with the strain rate at 0.33 stress triaxiality and room temperature. The data in the same figure was fitted with $\varepsilon_f = [D_1 + D_2 \exp(D_3 \sigma^*)][1 +$

$D_4 \ln(\dot{\varepsilon}^*)$] to determine D_4 damage parameter and the D_4 damage parameter was determined -0.017737 by fitting. The value of D_4 parameter was also calibrated by the numeric simulations. Numerical calibration using a D_4 value of -0.015 (called *calibrated* in Figure 4.13(b)) gives the true plastic fracture strain nearest to the experimental true plastic fracture strains. The used damage parameters in the simulations are further tabulated in Table 4.2, marked with numbers. The DM-3 in the same table resulted in the fracture strains of 0.97, 0.731, 0.48 at the stress triaxialities of 0.33, 0.56 and 1.02, respectively. These are near to the experimental true plastic fracture strains at the stress triaxialities of 0.33, 0.56 and 1.02 (0.94, 0.74 and 0.44).

Table 4.3. Damage parameters of the JC damage model

Damage Parameters	D_1	D_2	D_3	D_4	D_5
DM-1	0.16798	1.2736	1.5	-0.017737	0
DM-2	0.296	1.4566	2.012	-0.017737	0
DM-3	0.296	1.4566	2.012	-0.015	0

4.6. Mesh Sensitivity Analysis and Calibration

Quasi-static simulations were implemented using the flow stress equation of $\sigma_y(MPa) = (300 + 1300\varepsilon_{eq}^{0.4728})$ and the damage parameters of DM-1 and DM-2 (Table 4.3). Since the D_4 parameter is not effective in the quasi-static simulations, the DM-2 and DM-3 give the same failure strains in the quasi-static simulations. The true plastic effective fracture strains were also calculated numerically for each simulation after the fracture.

The numerical engineering stress-strain curves of the specimens with σ^*=0.33 using different mesh sizes and the DM-1 and DM-2 are shown in Figures 4.14(a) and (b), respectively. Although the numerical engineering facture strains at all investigated mesh sizes are higher than those of experiments as seen in Figure 4.14(a), the DM-1 numerical effective plastic facture strains of all mesh sizes are determined smaller than the experimental average true plastic facture strain (0.94). The DM-1 model numerical effective plastic facture strains are 0.88, 0.886, 0888 and 0.895 for the mesh size of 0.2, 0.3, 0.4 and 0.5, respectively.

The use of DM-2 however increases both the numerical engineering fracture strains, as seen Figure 4.14(b), and the numerical effective plastic facture strains. The DM-2 numerical effective plastic facture strains increase to 0.96, 0.96723, 0.98123, and 0.98409 for the mesh size of 0.2, 0.3, 0.4 and 0.5, respectively. In both models, DM-1 and DM-2, the experimental necking regions (Figure 4.15(a)) are seen to be narrower than the numerical necking regions (Figures 4.15(b) and (c)). Note also in Figure 4.15(a) and (b) that the mesh size is merely effective in altering the fracture strains and has an insignificant effect on the flow stress values. As the mesh size increases, on the other side, the effective plastic fracture strain increases.
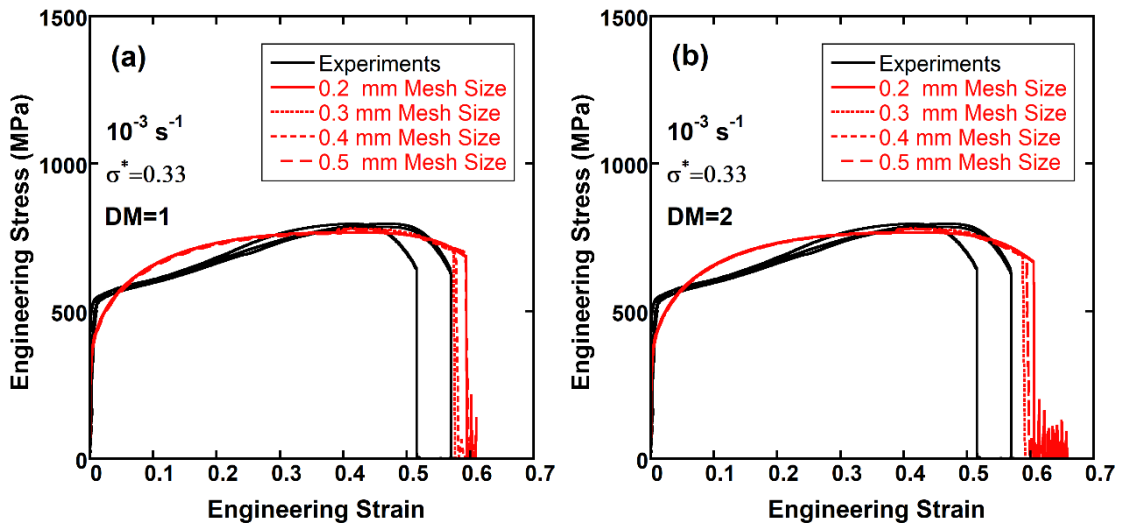
Figure 4.14. Quasi-static experimental and numerical engineering stress-strain curves of $\sigma^*=0.33$ with 0.2, 0.3, 0.4 and 0.5 mesh sizes: (a) DM-1 and (b) DM-2

The effect of mesh size is much more pronounced in the numerical engineering stress-displacement curves of the tension specimens with $\sigma^*=0.56$, as depicted in Figures 4.16(a) and (b). Increasing mesh size at this stress triaxiality increases both the displacements to fracture and the fracture stresses for both DM-1 and DM-2 models. The measured numerical effective plastic fracture strains of DM-1 model are 0.6592, 0.661, 0.663 and 0.667 for the 0.2, 0.3, 0.4, 0.5 mm mesh sizes, respectively. These values are lower than the average fracture strain value at the same triaxiality, 0.72. The use of DM-2 however increases the numerical effective plastic facture strains to 0.731, 0.76283, 0.78681 and 0.8012 for the 0.2, 0.3, 0.4 and 0.5 mesh sizes, respectively.
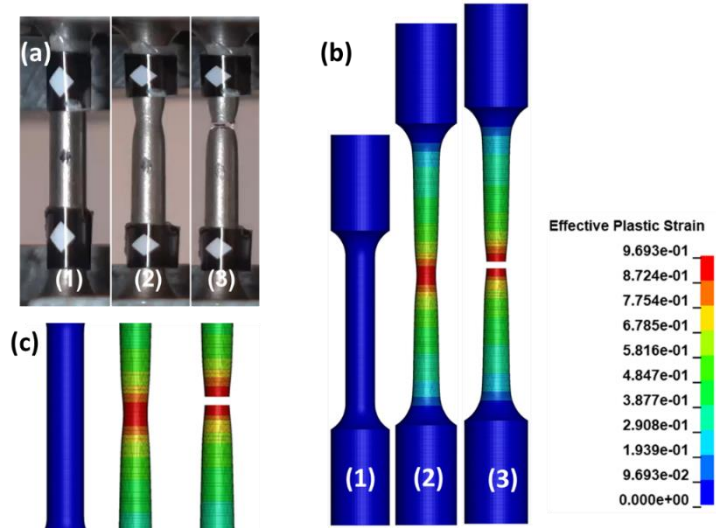
Figure 4.15. Quasi-static (a) experimental and (b and c) numerical deformation pictures of the test specimen of σ*=0.33 using the 0.2 mm mesh size and DM-2
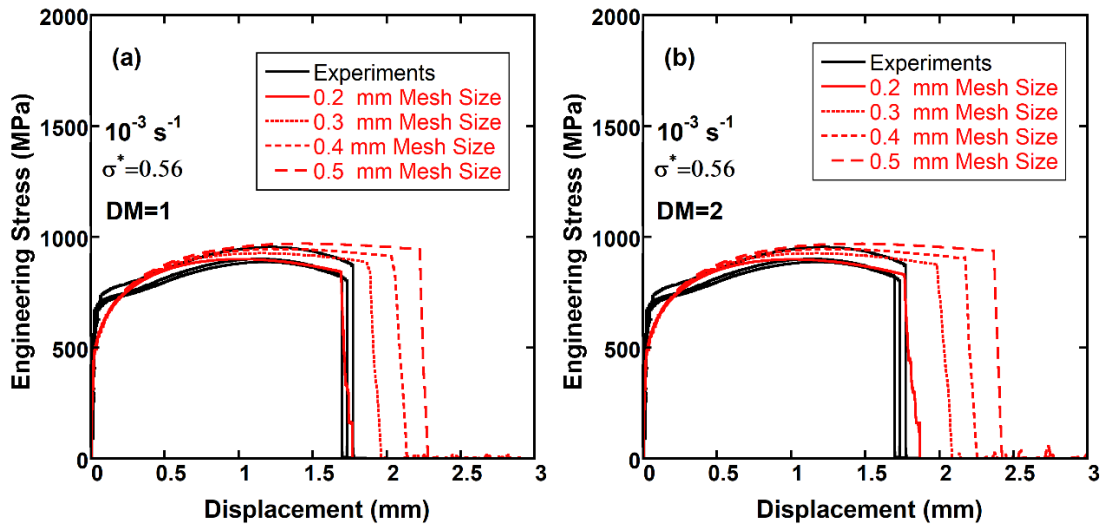
Figure 4.16. Quasi-static experimental and numerical engineering stress-displacement curves of σ*=0.56 using the 0.2, 0.3, 0.4 and 0.5 mesh sizes: (a) DM-1 and (b) DM-2

The experimental and numerical pictures of the tension test specimen (DM-2, 0.2 mm mesh) with σ*=0.56 at necking and after the facture confirm similar experimental and numerical deformation and fracture modes as shown sequentially in Figures 4.17(a-c). In

both, the specimen factures at the notched section and the maximum numerical effective plastic strain is about 0.74 as seen in the same figures.
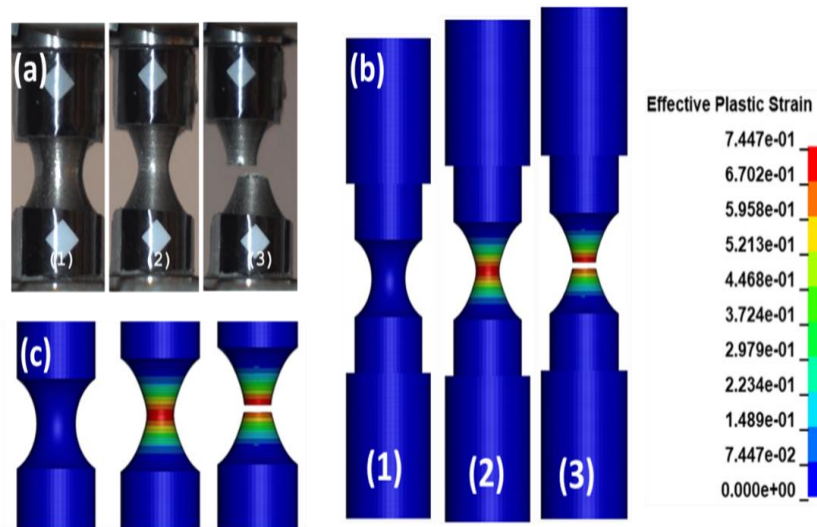
Figure 4.17. Quasi-static (a) experimental and (b and c) numerical deformation pictures of the test specimen with σ*=0.56 using the 0.2 mm size and DM-2

Somewhat a similar effect of mesh size is seen in the numerical engineering stress-displacement curves of the tension specimens of σ^*=1.02 as shown in Figure 4.18(a) and (b). Again, increasing mesh size increases both the displacements to fracture and fracture strains for both DM-1 and DM-2 models. The measured numerical effective plastic fracture strains of DM-1 model are 0.42, 0.4362, 0.4518 and 0.472 for the 0.2, 0.3, 0.4, 0.5 mm mesh sizes, respectively. These values are again lower than the average fracture strain value at the same triaxiality, 0.44. The use of DM-2 also increases the numerical effective plastic facture strains to 0.47, 0.489, 0.4926 and 0.5034 for the mesh size of 0.2, 0.3, 0.4 and 0.5 mm, respectively. The numerical engineering stresses at this stress triaxiality are much higher than those of experiments for both damage models as seen in Figure 4.18(a) and (b). The lowest numerical stresses comparable with those of the experiments are seen in the 0.2 mm mesh models. Also, the fracture strains nearest to experimental fracture strains are found using this mesh size. The experimental and numerical pictures of the tension specimen (DM-2, 0.2 mm mesh) with σ^*=1.02 at necking and after the facture are shown in Figure 4.19(a-c), respectively. In both, experimental and model, a more brittle behaviour at this triaxiality is clearly seen in the

same figures. Furthermore, the maximum effective plastic strain level of 0.453, seen in Figure 4.19(b), agrees well with the experimental average plastic fracture strain of 0.44.
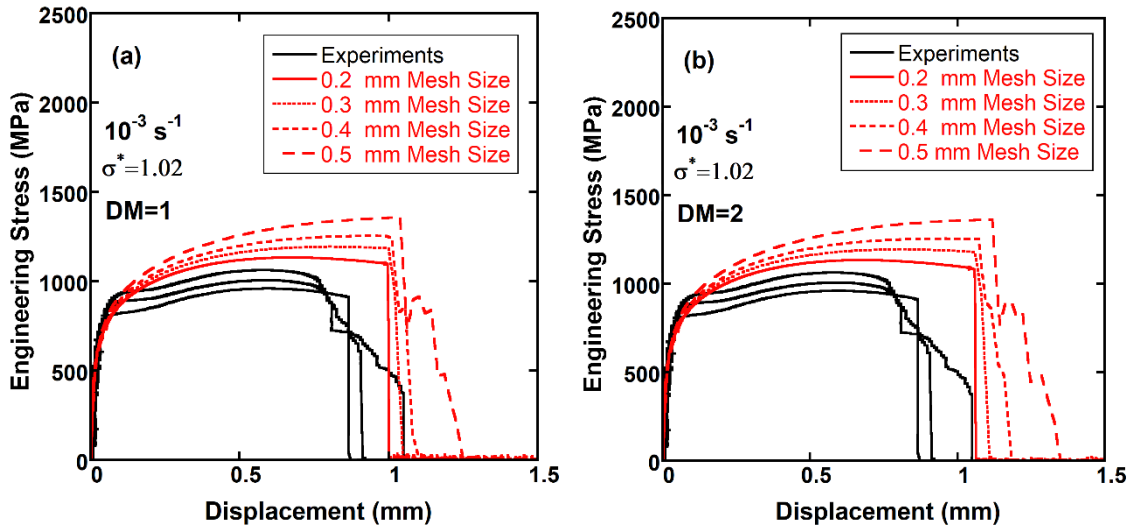

Figure 4.18. Quasi-static experimental and numerical engineering stress-displacement curves of σ*=1.02 using the 0.2, 0.3, 0.4 and 0.5 mesh sizes: (a) DM-1 and (b) DM-2
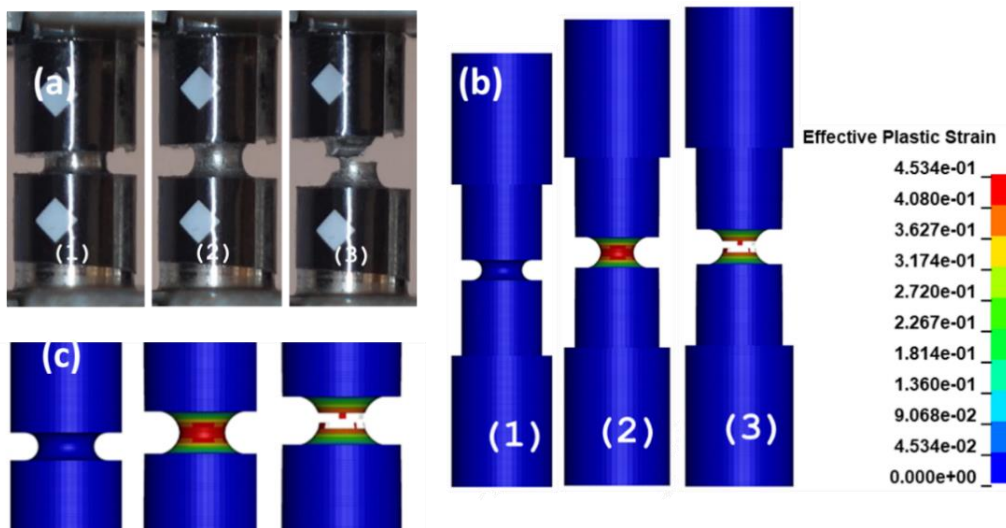


Figure 4.19. Quasi-static (a) experimental and (b and c) numerical deformation pictures of the test specimen of σ*=1.02 using the 0.2 mm mesh size and DM-2

Mesh size sensitivity analysis indicated that the selection of a 0.2 mm mesh size gives the numerical stresses and effective plastic fracture strains much nearer to those of experiments. It is also found that the use of DM-1 yield lower fracture strains than the experiments while DM-2 yields slightly higher fracture strains than the experiments. Based on above, the high strain rate models continued with the use of 0.2 mm mesh size.

4.7. Modelling High Strain Rate Tests: Selecting Appropriate *M* Value

In order to determine more precisely the *m* value of the JC stress equation and the D_4 value of the fracture strain equation, the constant speed high strain rate test model was initially simulated using the following flow stress parameters: *A*=300, *B*=1300, *n*=0.4728 and *c*=0.019 and the DM-2 parameters tabulated in Table 4.3. The test speed was 14.5 m s^{-1} corresponding to the test conducted at 2900 s^{-1} average strain rate. The *m* values were selected as 0, 0.6, 0.7 and 0.9. The numerical von Mises stress-equivalent plastic strain curves using different *m* values in constant speed high strain rate test models are shown in Figure 4.20. In the same figure, the reference strain rate JC flow stress-strain curve and the MLR stress at 2900 s^{-1} are also shown for comparison. The MLR stress at 2900 s^{-1} is assumed to be fully adiabatic as it is determined from the experimental stress-strain curve at 2900 s^{-1} average strain rate through the MLR correction. As seen in the same figure, the highest flow stresses are obtained when the *m*=0, corresponding to the isothermal high strain rate test. The stress-strain curve at this *m* value is nearly parallel to the reference strain rate JC stress-strain curve.
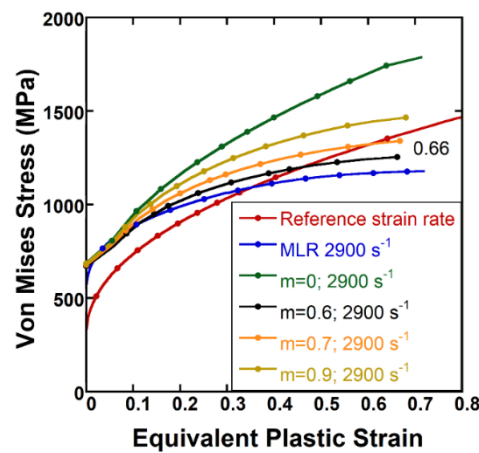
Figure 4.20. The numerical von Mises stress-equivalent plastic strain curves using different m values in the constant speed high strain rate test models

With decreasing the *m* value from 0.9 to 0.6, the stress values decrease and the stress-strain curves approach the adiabatic stress-strain curve. Even *m*=0.6, the model stresses are slightly higher than those of the adiabatic curve. The value of *m* is therefore predicted to be lower than 0.6. It is also note that the plastic fracture strain in these models (0.66, as shown in Figure 4.20) are lower than the experimental average fracture strain (0.7).

In order to determine an optimum *m* value in the constant speed high strain rate test models, the MLR stress at 2900 s^{-1} was imported into LS-OPT. The numerical models were solved by the LS-OPT by varying the *m* value between 0 and 1 and the objective function was set to converge to a tolerance value of 0.001. In these simulations, the DM-2 was used. By performing optimization with the Sequential with Domain Reduction method, the *m* value was converged to a certain area. Root Mean Square was calculated in LS-OPT between simulations and experimental data and optimum *m* values were calculated. The optimum *m* value was found 0.497.
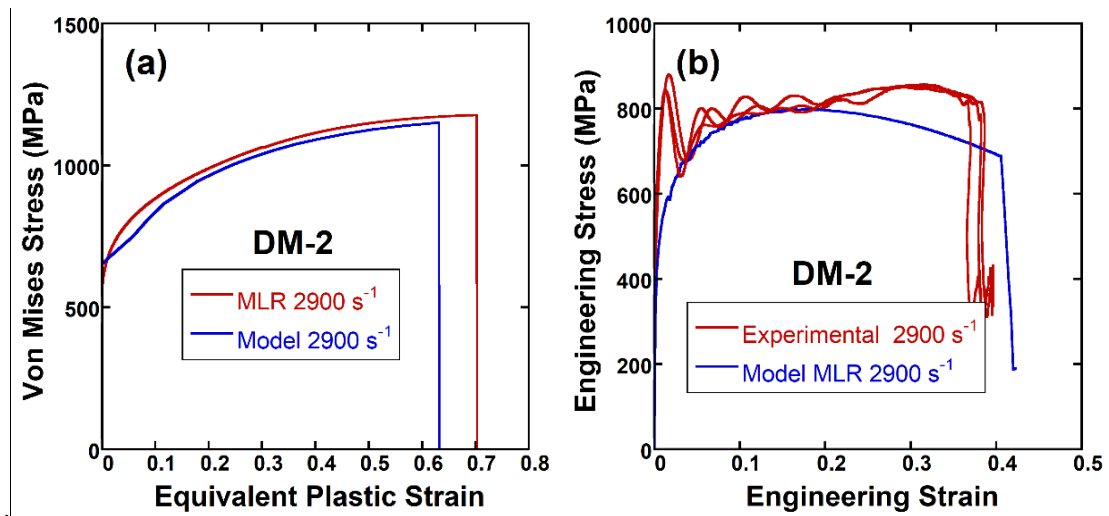
Figure 4.21. (a) numerical and experimental von Mises stress-strain and (b) engineering stress-strain curves using the DM-2 and m=0.4973 and (c) numerical and experimental Von Mises stress-strain and (d) engineering stress-strain curves using the DM-3 and m=0.4973
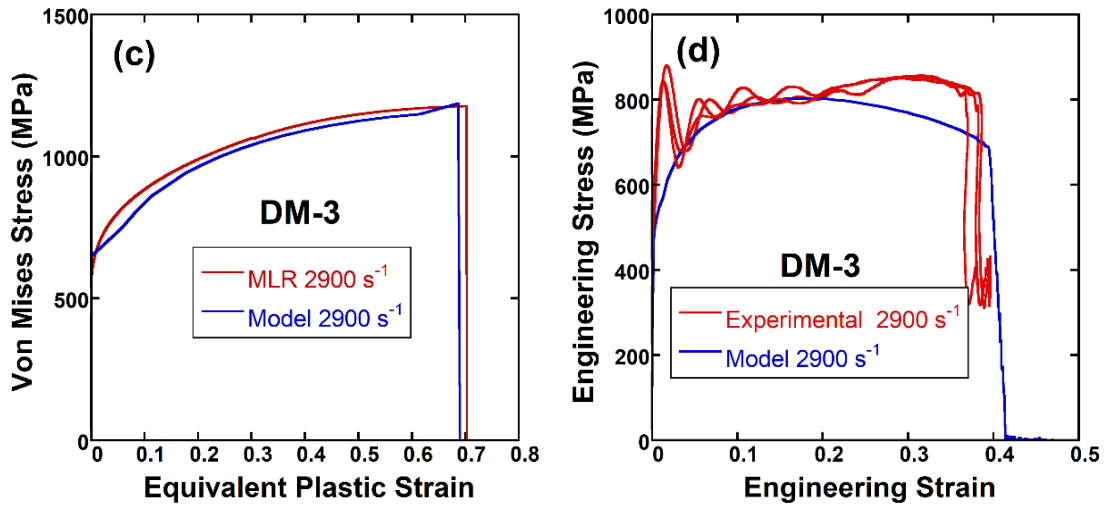
Figure 4.21 (cont.)
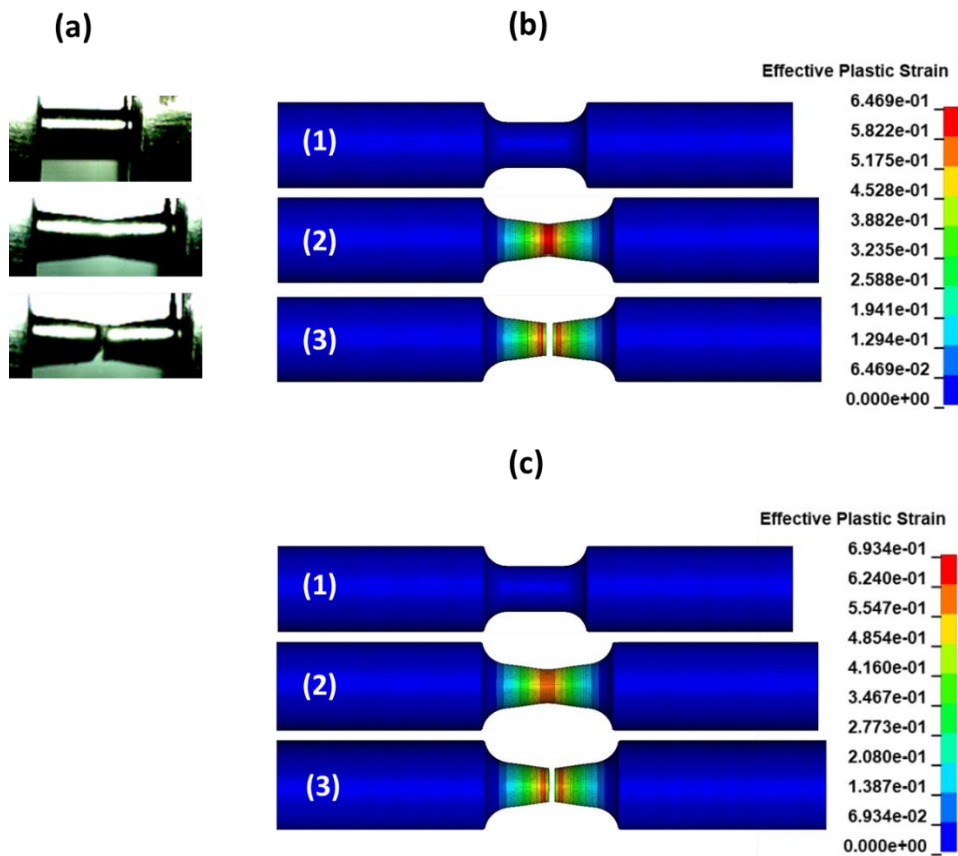
Figure 4.22. (a)Experimental and numerical (b)DM-2 and (c)DM-3 deformation pictures of the constant high strain rate tensile specimen with m=0.4973

The numerical equivalent stress-plastic strain and engineering stress-strain curves using DM-2 and m=0.497 are shown in Figures 4.20(a) and (b) together with the experimental curves. By changing the value of D_4 from -0.01773 to -0.0015, it was found that the numerical model fracture strains approached the experimental fracture strains. The DM-2 with this D_4 parameter is called DM-3 as tabulated in Table 4.2. Figures 4.20(c) and (d) show the numerical equivalent stress-plastic strain and engineering stress-strain curves using the DM-3 and m=0.497. The true plastic fracture strain with this damage model was numerically measured 0.691 which is found very much similar to experimental average fracture strain of 0.7. The experimental and numerical DM-2 and DM-3 deformation pictures of the constant high strain rate tensile specimen are further shown in Figures 4.21(a-c), respectively. As is seen in the same figures, the experimental and numerical facture of the test specimens are very much similar to each other. Note also that the specimen is continuously loaded in the constant high strain rate tensile specimen model until the fracture.

Table 4.4. The determined flow stress and damage parameters

JC Flow stress	A	B	n	C	m
	300	1300	0.4728	0.019	0.497304
Damage Parameters	D_1	D_2	D_3	D_4	D_5
	0.296	1.4566	2.012	-0.015	0

The determined flow stress and damage parameters of the investigated SS 304 alloy through calibration and optimization are tabulated in Table 4.4. The value of D_5 was taken zero in the simulations. The softening effect of high strain rate on the fracture strain is included to the fracture strain equation through the D_4 parameter. That is the D_5 and D_4 values are coupled as the experimentally determined dynamic fracture strains are also affected by the temperature indirectly through adiabatic heating.

4.8. Split Hopkinson Tension Bar Models

The SHTB test models were implemented using the 0.2 mm mesh and the flow stress and damage parameters listed in Table 4.4. Figure 4.23(a) shows the numerical reflected and transmitter bar stresses measured at the same location on the bars with the

strain gages in the SPTB test at 2900 s^{-1}, together with experimental bar stresses. As seen in the same figure, the numerical specimen fracture during second loading as with the experiment. The numerical and experimental reflected and transmitted bar stresses agree well with each other in the first loading, except the numerical reflected stresses are slightly higher and the numerical transmitted stresses are slightly lower than the experimental reflected and transmitter bar stresses, respectively. This discrepancy between the numerical study and the experimental results can partly be attributed to the use of the MLR-corrected equivalent stress in the simulations. This correction is based on the quasi-static strain rate stress-strain behavior, which inherently simplifies the complexities observed under dynamic loading conditions. In particular, during the second loading phase, the numerically predicted transmitted initial peak stress is noticeably higher than the corresponding experimentally observed transmitted stress initial peak stress, as illustrated in Figure 4.23(b). This discrepancy arises because, in the experimental setup, the specimen undergoes cooling during the unloading phase. In contrast, the numerical model operates under the assumption of fully adiabatic conditions, as it does not incorporate a thermal solver to account for heat dissipation or thermal gradients. The numerical engineering stress-strain curve derived from the simulations is presented alongside the experimental curve in Figure 4.23(b). This comparison reveals that the Split Hopkinson Tension Bar (SHTB) numerical model produces stress-strain behavior that closely aligns with the results obtained from high strain rate tests performed at a constant speed. This demonstrates the effectiveness of the SHTB model in replicating the material's response under dynamic loading conditions. Moreover, the deformation profiles of the specimen at three critical stages which are prior to testing, at the end of the first loading, and at fracture during the second loading are depicted in Figure 4.24. Both the numerical and experimental results indicate that fracture consistently occurs at the onset of the second loading phase. Specifically, the specimen fractures in the necked region located at the mid-section, where stress concentration is highest. This is evident in both the numerical and experimental images shown in the same figure. Additionally, the numerical model predicts a maximum plastic strain of 0.718 at the point of fracture. This value is remarkably close to the experimentally determined average fracture strain, further validating the accuracy of the numerical model in capturing the material's mechanical behavior under high strain rate loading.
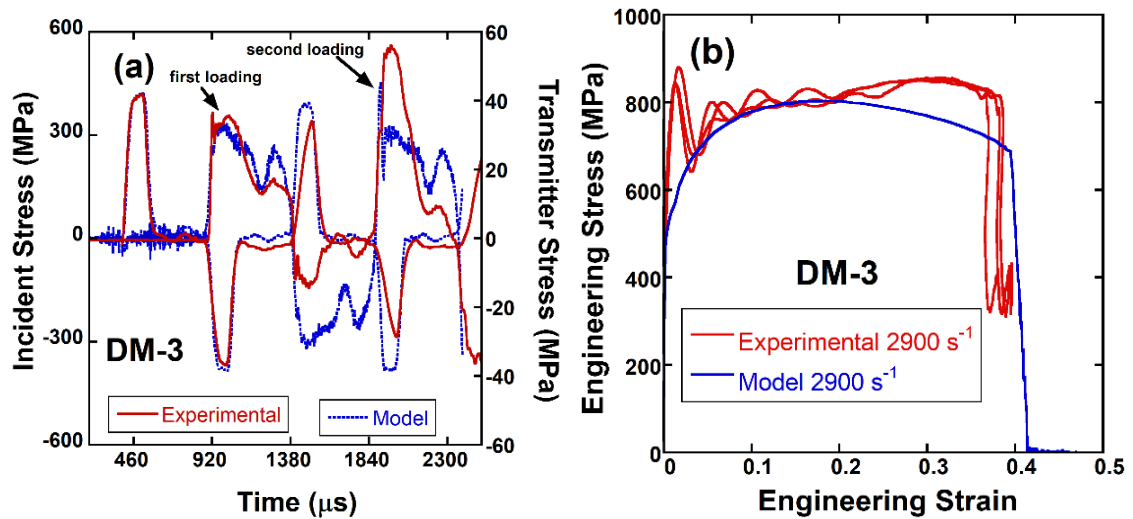
Figure 4.23. (a)Experimental and numerical SHTB bar stresses and (b)numerical and experimental engineering stress-strain curves
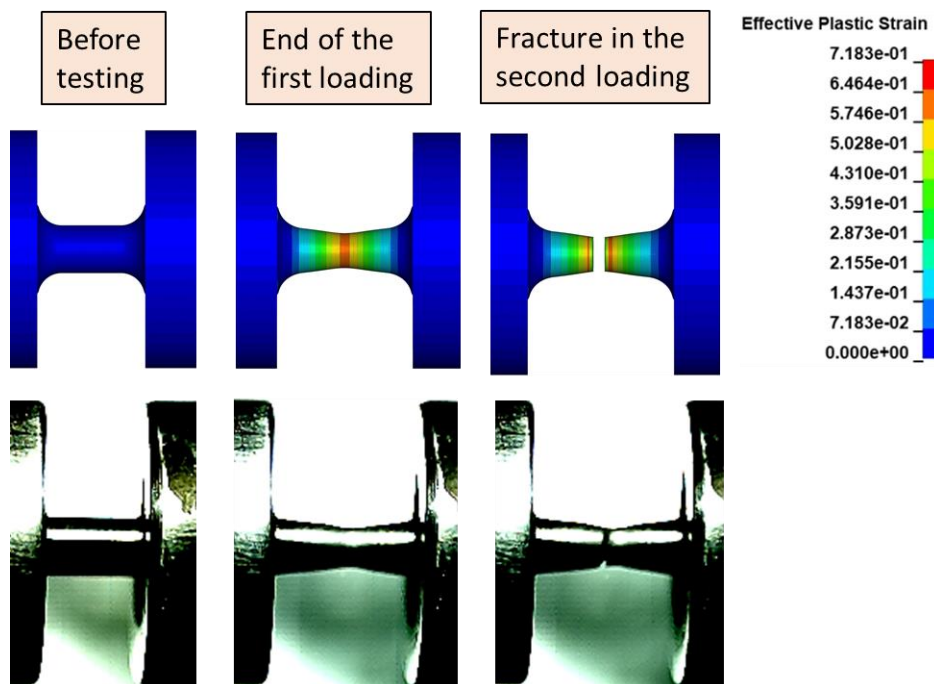
Figure 4.24. The numerical and experiment deformation pictures of the SHTB test at 2900 s^{-1} before testing, at the end of the first loading and fracture in the second loading

By providing detailed comparisons of stress-strain behavior, deformation profiles, and fracture characteristics, these results highlight the strengths and limitations of the

numerical model, particularly in terms of its ability to replicate complex physical phenomena such as thermal effects and dynamic material response.

4.9. Ballistics Tests and Simulations

The ballistic test models of SS 304 were constructed using flow stress and damage equations in Table 4.4. Figure 4.25(a) shows uncoated and Figure 4.25(b) B_4C-coated plate models. In both models, the bullet perforated the plates. Since the hardness of the plate surface increased with B_4C coating, the brass jacket part of the bullet was deformed much more in the B_4C-coated ballistic test model plate. The front surface stress profiles after bullet perforation, shown in the same figures, are not the same for uncoated and B_4C-coated plates. The impact of the bullet creates a compressive stress on the plate, through the thickness and surface of the plate. The surface stresses are returned back as tensile stress, leading to fracture of the brittle ceramic layer and forming multiple rings in the radial direction

Figures 4.26(a) and (b) show experimental and numerical APM2 bullet ballistic test damage and detailed view of the bullet hole on SS 304 and coated SS 304 plate, respectively. The highly deformed plastic deformation hinges are clearly seen on the coated plate in Figures 4.26(a). The plastic strain is seen in Figure 4.26(c) on the plate highest near the impact point. More, the damage parameter value is also highest in the impact point, showing the locations of the coated layer fracture.
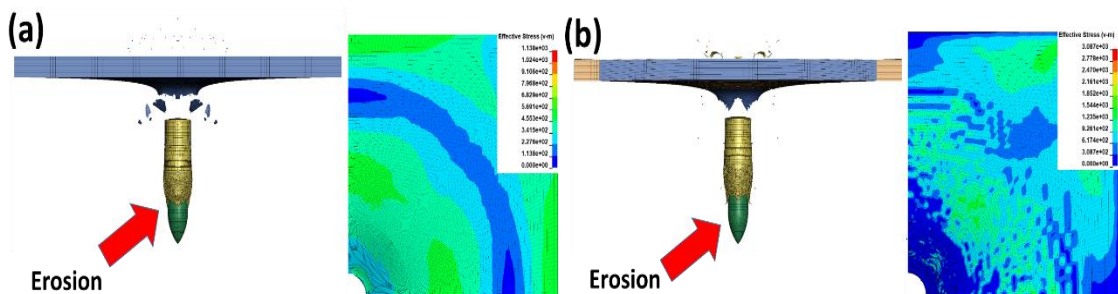
Figure 4.25. Model full and quarter pictures after bullet perforation (a) SS304 plate (b) coated plate, and surface stresses after perforation
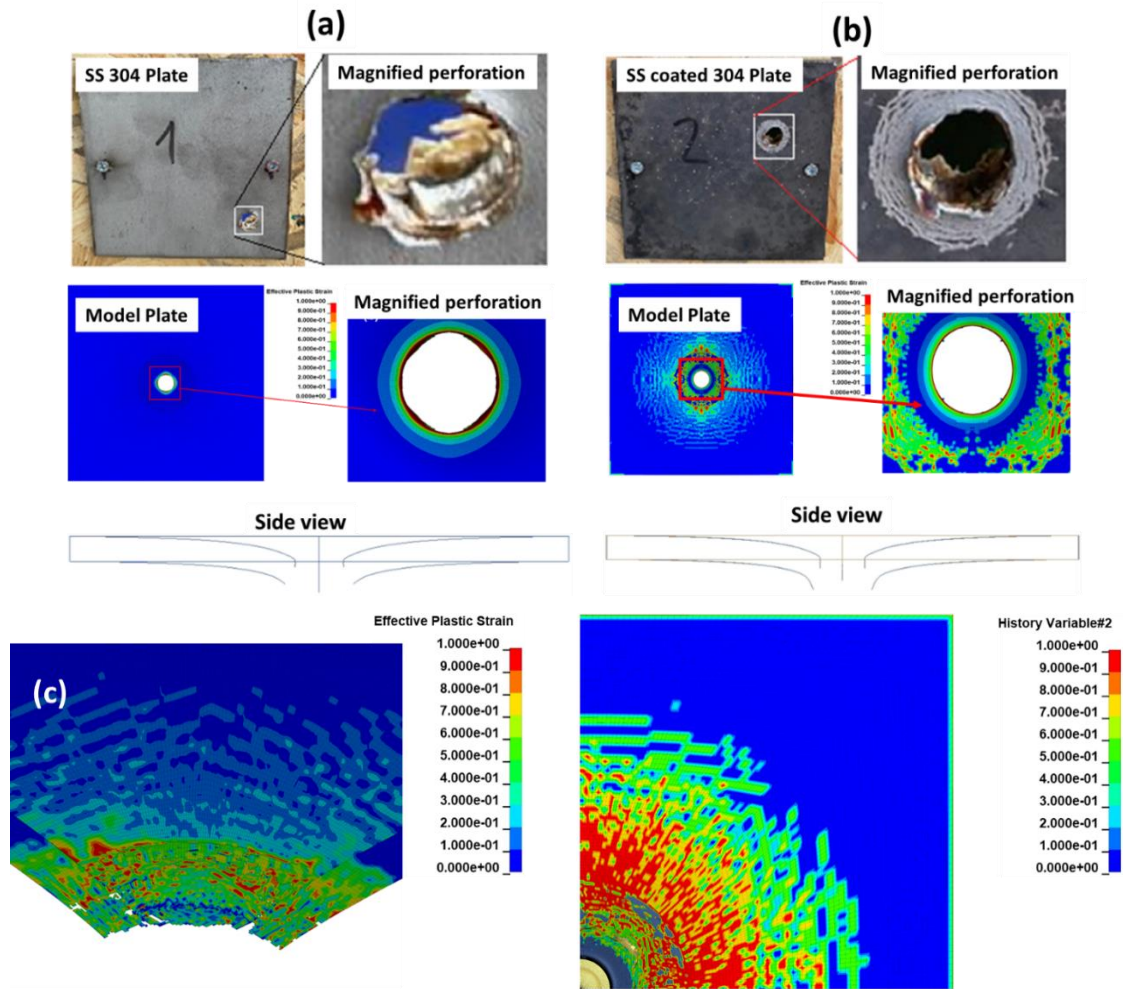
Figure 4.26. Experimental and numerical ballistic test damage and detailed view of the bullet hole on (a) uncoated SS 304 plate and (b) coated plate and (c) plastic strain and damage distribution in the coated plate
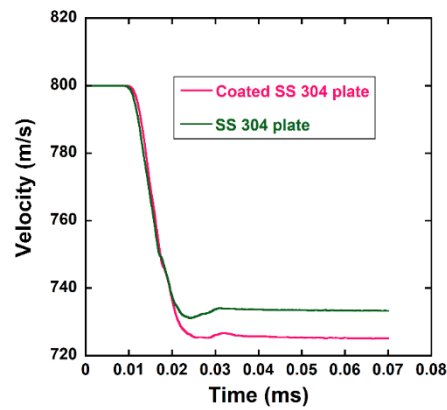
Figure 4.27. Change of bullet velocity for SS 304 plate and coated SS 304 plate.

As a result of the impact test at 800 m s^{-1}, there was a loss of energy in the speed of the bullet after perforation. The numerical velocity of the bullet after perforation is 733.31 m s^{-1} for the uncoated SS 304 plate and 725.12 m s^{-1} for the coated plate (Figure 4.27). This proves an enhancement in the ballistic performance of the coated plates.

4.10. Microscopic Analysis of Tested SS 304 Specimens

The tensile test specimens were split into two after testing using a diamond cutter. The surface of the cut-sections was then polished and etched after mounting. The hardness tests were conducted on the surface of the polished specimens in two distinct regions: 1) outside of the necking (homogenously deformed region) and 2) in the necked region near the fracture side (deformation localized region) as schematically shown and marked as 1 and 2 in Figure 4.28(a). The necking strain for the specimen tested at 1x10^{-3} s^{-1} is 0.39, as shown in the same figure, and before this strain the deformation is homogeneous and above it the deformation is localized.
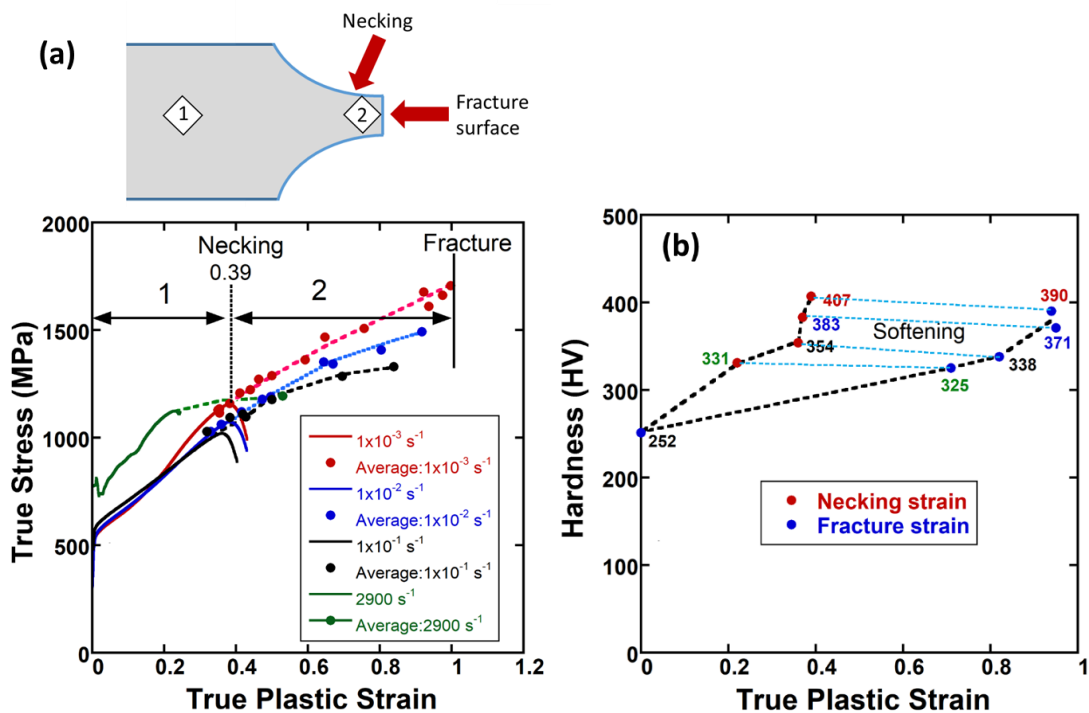
Figure 4.28. (a) The regions of hardness tests on the stress-strain curves and schematic of tensile test specimen after testing and (b) HV numbers at the necking and fracture strains.

The corresponding HV numbers at the necking strain (Region 1) and fracture strain (Region 2) are tabulated in Table 4.5 for the specimens tested at 4 different strain rates. In Figure 4.28(b), the average hardness numbers are shown at the necking and fracture strains for 4 different strain rates. For homogeneous and localized deformations, the HV number decreases as the strain rate increases, proving a higher fraction of the martensite formation and a higher deformation strain at lower strain rates. The HV numbers corresponding to the fracture strain are however found to be lower than those corresponding to the necking strain, although, the fracture strains are more than two times the necking strains (Figure 4.28(b)). This indicates a softening during the specimen extension in the necking until the facture. The flow stresses at 1×10^{-3} s^{-1} are divided by three in order to determine the hardness values corresponding to the yield strengths.

Table 4.5. The hardness values (HV) at the necking and fracture strain

Rate	10^{-3} s^{-1}		10^{-2} s^{-1}		10^{-1} s^{-1}		2900 s^{-1}		Untested
Points	HV	Fract.	HV	Fract.	HV	Fract.	HV	Fract.	
1	397.24	385.3	389.12	374.44	369.48	331.13	341.02	329.47	246.36
2	407.33	369.43	386.25	386.25	357.87	372.84	327.96	318.91	249.20
3	417.08	386.30	391.03	368.92	348.26	352.12	327.60	320.91	249.14
4	409.79	398.05	371.76	357.68	362.02	310.14	322.40	323.72	256.51
5	403.24	413.15	376.61	363.49	332.23	325.43	337.99	332.24	258.41
Ave.	406.93	390.45	382.954	370.75	354.166	338.32	331.394	325.050	251.924
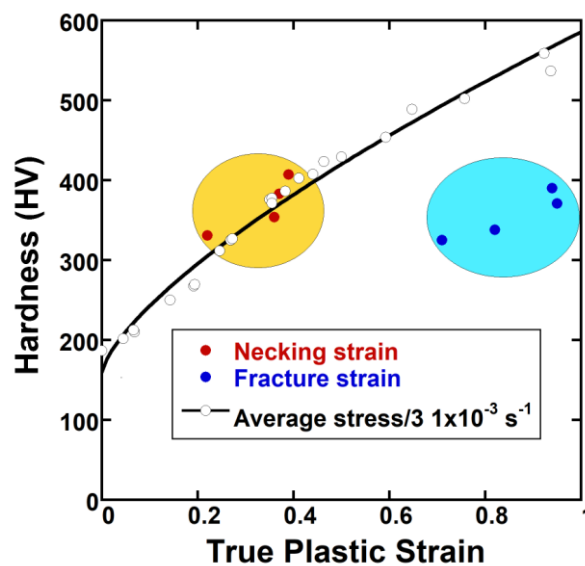
Figure 4.29. Flow stress/3 at 1×10^{-3} s^{-1} and hardness values versus plastic strain

The results are drawn together with the hardness numbers in Figure 4.29. The hardness values at the necking strain agree with the flow stress/3 curve while the hardness values at the fracture strain are much lower than those of the flow stress/3 as depicted in Figure 4.29. The reduced hardness may be due to the texture development in the transverse direction since the hardness values were obtained normal to the loading direction.

The SEM micrographs of untested specimen and the specimens tested at 10^{-3}, 10^{-1} and 2900 s^{-1} in homogeneously deformed regions are shown in Figures 4.30(a-d), respectively. The untested material contains also martensite, mainly induced during rolling. The martensite containing localized regions in the untested specimen seen in Figure 4.30(a) are aligned parallel to the rolling direction. A magnification of the region seen in the inset of the same picture show shear bands and etch pits. These etch pits occur in the regions containing shear bands and/or martensite. As the martensite phase is harder than the austenite, a dislocation network is expected to occur at the interface due to difference in the elongations between the phases, leading to a higher rate of reaction with the etching solution
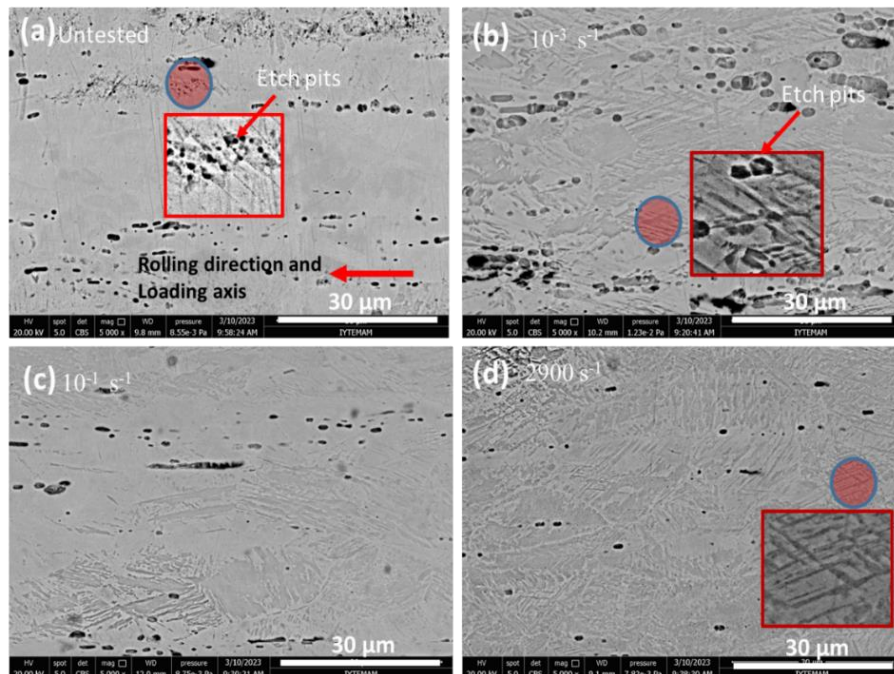
Figure 4.30.The SEM micrographs of homogenous deformation regions of the specimens (a) untested and tested at (b)10^{-3}, (b)10^{-1} and (d)2900 s^{-1}

Furthermore, the initially existing shear banded regions formed through the rolling direction also act as nuclei for the martensite transformation during testing. The regions of heavily accumulated shear bands with and without martensite are also seen in the tensile tested specimens at three different strains rates. These regions are magnified and shown in the inset of Figures 4.30(b) and (d) for the specimen tested at 1×10^{-3} and $2900\ s^{-1}$, respectively. A higher number etch pits in the specimen tested at 1×10^{-3} than the specimens tested at 1×10^{-1} and $2900\ s^{-1}$ also indicate a higher fraction of martensite formation at $1\times10^{-3}\ s^{-1}$, as seen in Figures 4.30(b-d), respectively

In the necking region, the strains are higher, hence, the martensite fraction is also higher. As seen in Figure 4.31(a), the number etch pits increases significantly in the specimen tested at $1\times10^{-3}\ s^{-1}$ in necked region near the fracture surface. The etch pits also extend through the loading and rolling direction. The number etch pits and their sizes are significantly reduced in the specimen tested at $2900\ s^{-1}$ as shown in Figure 4.31(b), proving a lower fraction of martensite at this strain rate.
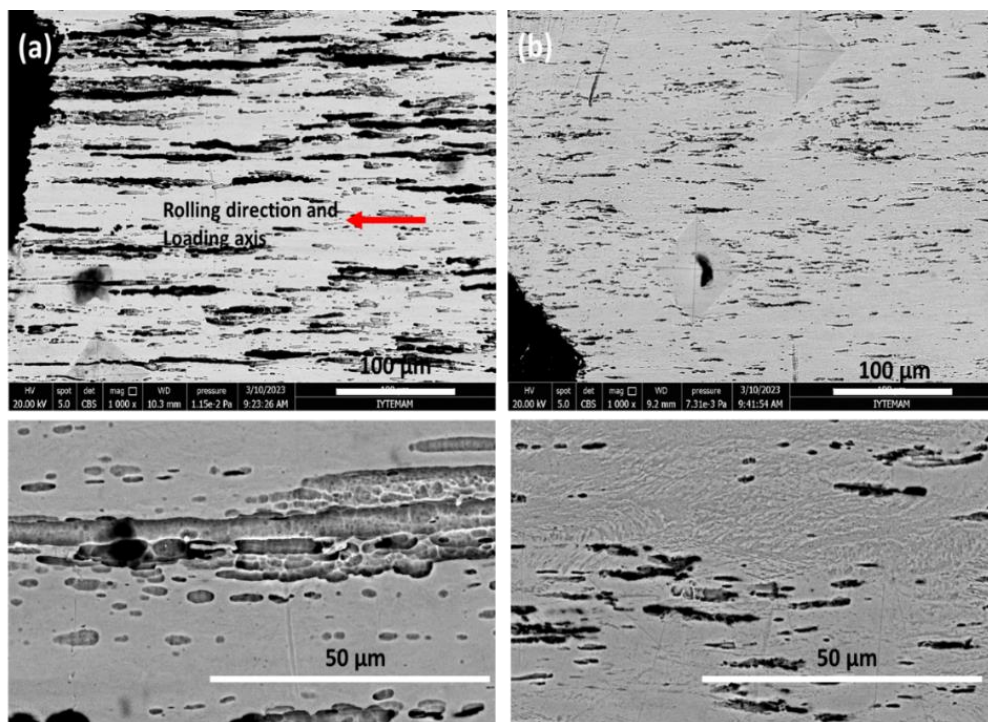
Figure 4.31. The SEM micrographs near the fracture the specimens tested at (a)10^{-3} and (b)$2900\ s^{-1}$
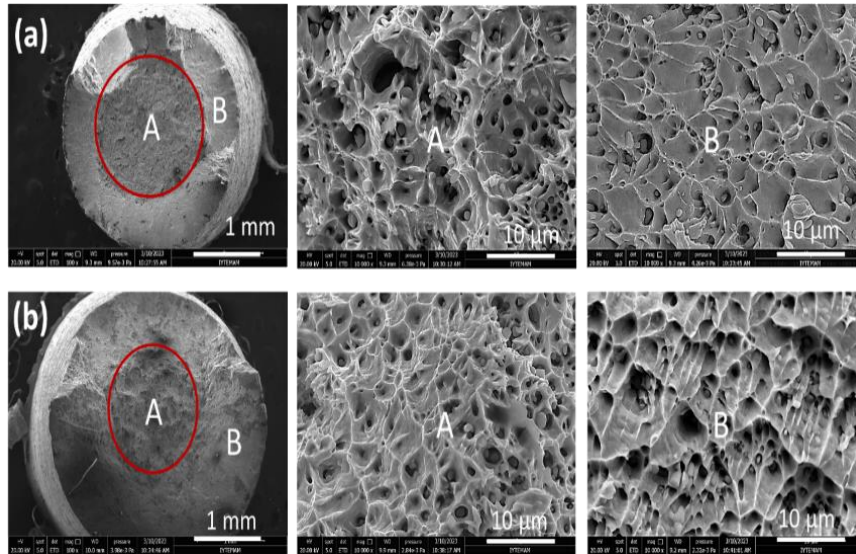
Figure 4.32. The SEM micrographs of the fracture surfaces of the specimens tested at (a)10^{-3} and (b)2900 s^{-1}

The SEM micrographs the fracture surfaces of the specimens tested at 10^{-3} and 2900 s^{-1} are shown in Figures 4.32(a) and (b), respectively. At both strain rate, the fracture region is composed of two distinct regions, a highly dimpled ductile fracture region marked as A and a sheared region marked as B in the same figures. The void formation and growth occur in region A and after that the crack propagates quickly to the region B forming a shear type of facture and complete separation of the specimen in the necked region, a well-known characteristic of the fracture of ductile metals. The dimples are smaller and deeper in the specimen tested at 10^{-3} s^{-1} than the specimen tested at 2900 s^{-1}, conforming a higher fracture strain of the quasi-static tested specimen.

4.11. Comparison with Previous Studies

Song and Sanborn [30] previously determined the modified JC flow equation (Equation 2.18) parameters between 10^{-3} and 3000 s^{-1}. The determined parameters are tabulated in Figure 2.16. Seo et al. [35] determined the modified JC model parameters as tabulated in Figure 2.22. Li et al. [33] determined the JC parameters between 20 and 600 °C and between 0.001 and 3000 s^{-1} as tabulated in Figure 2.19. Jia et al. [34] determined the JC parameters between 0.001 and 39000 s^{-1} and between 77 and 1073 K as shown in Figure 2.20.
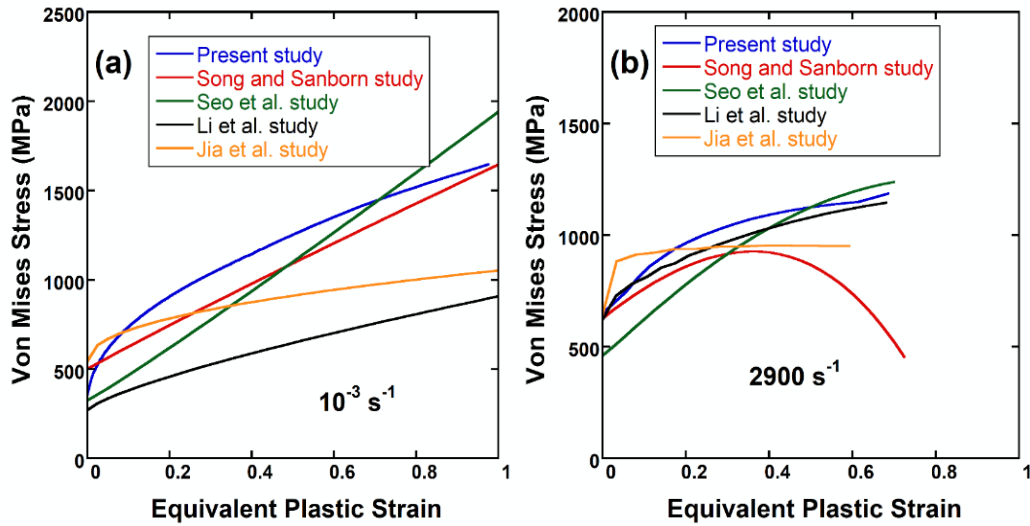
Figure 4.33. Comparison of the equivalent plastic strain curves of the present and previous studies at (a) 10^{-3} and (b) 2900 s^{-1}

The flow stress-strain curves at 1×10^{-3} and 2900 s^{-1} was directly calculated in the Song and Sanborn and Seo et al. models. While the flow stress-strain curves at 2900 s^{-1} in the Seo et al. and Li et al. studies were determined through simulations. For that, the parameters of the JC equations of the Seo et al. and Li et al. were used to in the constant high strain rate model simulations. The *m* and *c* values in Li et al. [33] were taken 0.43738 and 0.091 s^{-1} by applying interpolations to the *m* and *c* values given in Figure 2.19 at the different and temperature ranges, respectively. In the high strain rate models, the DM-3 of the present work was used as the damage model. After the simulation, the equivalent stress strain curve at 2900 s^{-1} were determined for comparison with the present model curves.

As shown in Figure 4.33(a), Song and Sanborn study shows similar quasi-static stress-strain behaviour with the present study. Seo et al. study shows lower stresses at low strains abut higher stresses at increasing strains. Li et al. and Jia et al. studies also show lower stresses than the present study. At 2900 s^{-1}, Li et. study exhibits similar stresses with the present study as depicted in Figure 4.33(b) until about fracture. In the models with the DM-3, Jia et al. stress model gives a plastic failure strain of 0.6 as seen in Figure 4.34(a) while Li et al. study and the present study stress model give very similar failure strains, sequentially 0.7 and 0.691 as seen in Figure 4.34(b) and (c), respectively.

87
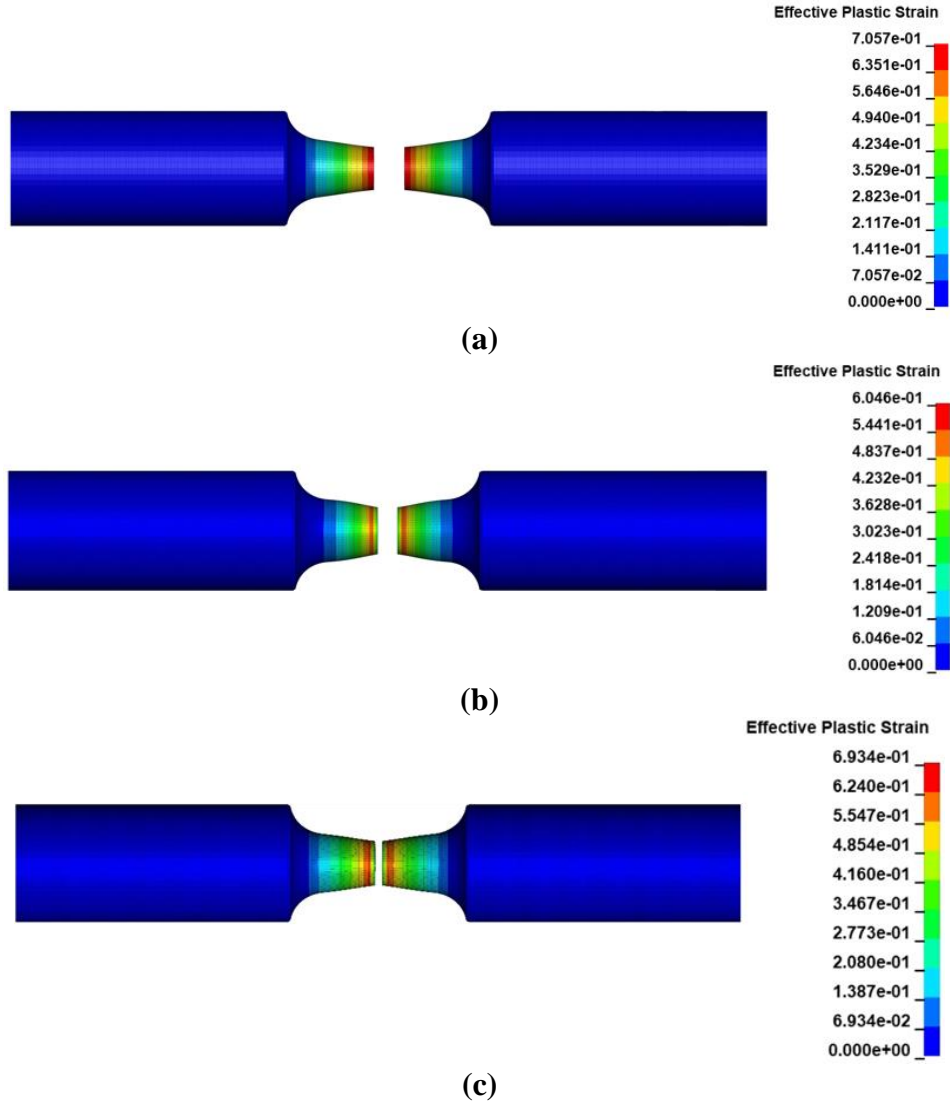
Figure 4.34. Numerical deformation pictures of the constant high strain rate model at strain rate of 2900 s^{-1} (a) Li et al., (b) Jia et al. and (c) present study

Table 4.6. The JC equation parameters of presents and previous studies of SS 304

Ref	A (MPa)	B (MPa)	n	c (s^{-1})	M	$\dot{\varepsilon}_0$ (s^{-1})
Present study	300	1300	0.4728	0.019	0.497304	10^{-3}
Seo et al.	325	1616	1.06	0.022	0	10^{-3}
Li et al.	270	637	0.7587	0.0749: 1000 s^{-1} 0.0921: 2000 s^{-1} 0.100: 33000 s^{-1}	0.538: 200 ºC 0.653:400 ºC 0.808: 600 ºC	10^{-3}
Jia et al.	544.2	507.2	0.4673	0.0321	0.4546	10^{-3}

The JC parameters of the present and previous studies are tabulated in Table 4.6. The strain rate parameter of Seo et al., 0.022, is comparable with while the c parameter of Ja et al. study (0.0321) slightly higher than the parameter of the present study (0.019). The *m* parameter of the present study, 0.497304, and the *m* parameter of Jia et al. study, 0.4546, are comparable as tabulated in the same table. As seen in the same table Li et al. reported a higher *m* value, 0.532, until about 200°C.

4.12. Prediction of the Martensite Content

The martensite volume fraction was predicted using the equivalent stresses at different strain rates. The martensite volume fraction was calculated based on the work of Pagen et al.[28] given in Section 2.1. The fraction of martensite is given by the following modified Olson-Cohen Model

$$f_m = 1 - \exp\left\{-\beta_0 \left(\frac{\dot{\varepsilon}}{\dot{\varepsilon}_0}\right)^{q_3} \left[1 - \exp\left(-(\alpha_0 + q_1\Delta T)\left(\frac{\dot{\varepsilon}}{\dot{\varepsilon}_0}\right)^{q_2}\overline{\varepsilon^p}\right)\right]^n\right\} \qquad (4.1)$$

In the calculation, the temperature increase term ΔT was taken zero for the quasi-static tests, 10^{-3}, 10^{-2} and 10^{-1} s^{-1} and numerically calculated from the constant strain tension test model of SS 304 for 2900 s^{-1}. The values of the parameters of Equation 4.1 are further tabulated in Table 4.7.

Table 4.7. Parameters of volume fraction of martensite for a SS 304 L

(Source: Peng et al.[28])

Parameter	α_0 (MPa)	β_0 (MPa)	q_1	q_2	q_3	ρ (kg m^{-3})	c_p (J kg^{-1} °C^{-1})	N
Pagen et al.	286.6	1642.7	278.4	74.43	9.91	8030	500	0.45

The stress of SS 304 is given by the following rule of mixture equation

$$\sigma = (1 - f_m)\sigma_\gamma + f_m\sigma_{\alpha'} \qquad (4.2)$$

where σ_γ is the stress of austenite and $\sigma_{\alpha'}$ is the stress of martensite, which are calculated sequentially by using the following relations

$$\sigma_\gamma = \{\sigma_{0\gamma} + Q_\gamma[1 - \exp(-b_\gamma\overline{\varepsilon^p})]\}\left[1 + C_\gamma\ln\left(\frac{\dot{\varepsilon}}{\dot{\varepsilon}_0}\right)\right]\left[1 - \left(\frac{T - T_0}{T_{m\gamma} - T_0}\right)^{m\gamma}\right] \quad (4.2)$$

$$\sigma_{\alpha'} = \{\sigma_{0\alpha'} + Q_{\alpha'}[1 - \exp(-b_{\alpha'}\overline{\varepsilon^p})]\}\left[1 + C_{\alpha'}\ln\left(\frac{\dot{\varepsilon}}{\dot{\varepsilon}_0}\right)\right]\left[1 - \left(\frac{T - T_0}{T_{m\alpha'} - T_0}\right)^{m\alpha'}\right] \quad (4.3)$$

The values of the parameters of above equations are further tabulated in Table 4.8. In the calculations, the values of C_γ and $C_{\alpha'}$ were taken 0.019, the average of the strain rate sensitivity of SS 304. The values of $m\gamma$ and $m\alpha'$ were taken 1.1, typical for metallic structures. The martensite volume fraction was then calculated using the following relation,

$$f_m = \frac{\sigma - \sigma_\gamma}{\sigma_{\alpha'} - \sigma_\gamma} \quad (4.4)$$
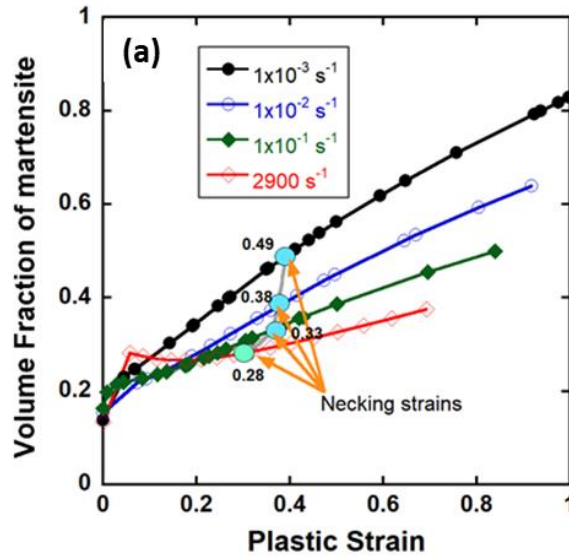
(cont. on the next page)

Figure 4.35. (a) Predicted martensite volume fraction of the tested SS 304 at different strain rates and (b) the stress-strain curves of austenite and martensite together with the experimental average stress-strain curves at different strain rates
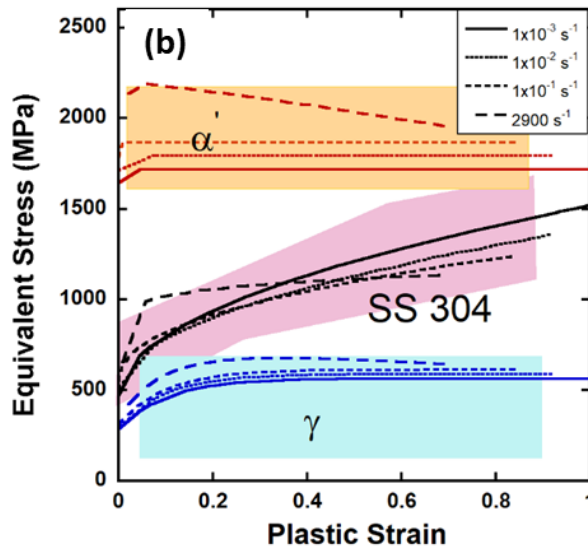
Figure 4.35 (cont.)

Table 4.8. Parameters of JC flow curve for SS 304 L

(Source: Peng et al.[28])

Parameter	$\sigma_{0\gamma}$ (MPa)	$\sigma_{0\alpha'}$ (MPa)	Q_γ (MPa)	$Q_{\alpha'}$ (MPa)	b_γ	$b_{\alpha'}$	C_γ	$C_{\alpha'}$	m	$\dot{\varepsilon}_0$ (s⁻¹)
Pagen et al. [28]	286.6	1642.7	278.4	74.43	9.91	500	0.0148	10^{-4}	0	10^{-3}
Present Study	286.6	1642.7	278.4	74.43	9.91	500	0.019	0.019	1.1	10^{-3}

The predicted martensite fractions of the tested SS 304 at different strain rates are shown in Figure 4.35(a).   As seen in Figure 4.35(a), the used material model predicted an initial martensitic fraction of 0.15-02 in the tested SS 304. This results agrees with the microscopic observations on the untested specimen in Figure 4.30(a) in which martensite containing localized regions are detected, mainly induced during rolling. As is noted the martensite fraction is higher in the high strain rate tested specimen at low strains; thereafter, the rate of formation decreases significantly with the adiabatic heating. The final fraction of martensite, at the fracture strain, increases to about 0.84, 0.64, 0.5 and 0.37 in the specimens tested at 10^{-3}, 10^{-2}, 10^{-1} and 2900 s⁻¹, respectively. The stress-strain curves of austenite and martensite together with the equivalent stress-strain curves of SS 304 at different strain rates are shown in Figure 4.35(b). In the calculations, both austenite

and martensite were taken strain rate sensitive. At the necking strains (Figure 4.35(a)), the fraction martensite fractions are 0.49, 0.38, 0.33 and 0.28 for the specimens at 10^{-3}, 10^{-2}, 10^{-1} and 2900 s^{-1}, respectively. These fractions also agree well with the measured average hardness values, sequentially 407, 383, 354 and 331 HV.

CHAPTER 5

CONCLUSIONS

This thesis focused on the development of material flow stress and damage models for a SS 304, particularly at a high strain rate. The primary goal was to determine the Johnson-Cook (JC) material model parameters for both flow stress and damage, which are critical for accurately predicting the material's behaviour under different loading conditions. Through extensive experimental work, the flow and damage parameters were extracted and validated with the experimental data. One of the significant findings of this research was the influence of martensitic transformation on the stress-strain behaviour of SS 304. The study confirmed that under plastic deformation, especially at low strain rates, the material undergoes a phase transformation from austenite to martensite. This transformation significantly affects the material's mechanical properties, particularly in the plastic region, where the stress-strain curve exhibits distinct changes. At higher strain rates, the study observed that adiabatic heating limits the formation of martensite, thus altering the stress-strain relationship. This is crucial for industries that rely on the use of SS 304 in dynamic loading environments, as it provides deeper insights into how the material will perform under different conditions. The equivalent stress-strain curves obtained from experiments conducted at various strain rates served as the foundation for calibrating the JC model parameters. The successful application of these parameters in the LS-DYNA simulation environment further validated their accuracy. By comparing the newly derived parameters with those found in existing literature, this study highlighted both the consistencies and discrepancies, offering explanations rooted in the unique experimental conditions, material batches, and strain rate effects observed during testing. Furthermore, the work conducted in this thesis extends beyond just parameter identification. It provides a comprehensive understanding of how the microstructural evolution, particularly the austenite to martensite transformation, influences the macroscopic mechanical response of SS 304. This understanding is vital for the design and analysis of components made from SS 304, especially in applications where the material is subjected to high strain rates, such as in automotive, defence, and aerospace industries. The successful validation of the JC model parameters using experimental data

reinforces the reliability of the findings. The comparison with existing literature not only ensures the robustness of the derived parameters but also contributes new insights into the behaviour of SS 304 under varying strain rates. This comparison is particularly important as it helps to contextualize the results within the broader scope of material science and engineering, where variations in experimental methods and conditions often lead to different conclusions. The insights gained from this study regarding martensitic transformation and its impact on material behaviour under different strain rates will undoubtedly benefit future research and industrial applications, ensuring safer and more efficient use of SS 304 in critical components.

REFERENCES

1. Cottrell, A. H., Theory of dislocations. *Progress in Metal Physics* **1953,** *4*, 205-264. https://doi.org/10.1016/0502-8205(53)90018-5

2. Woo, W.; Jeong, J. S.; Kim, D. K.; Lee, C. M.; Choi, S. H.; Suh, J. Y.; Lee, S. Y.; Harjo, S.; Kawasaki, T., Stacking Fault Energy Analyses of Additively Manufactured Stainless Steel 316L and CrCoNi Medium Entropy Alloy Using In Situ Neutron Diffraction. *Sci Rep* **2020,** *10* (1), 15. https://doi.org/10.1038/s41598-020-58273-3 1

3. Rémy, L.; Pineau, A., Twinning and strain-induced f.c.c. → h.c.p. transformation on the mechanical properties of Co☐Ni☐Cr☐Mo alloys. *Materials Science and Engineering* **1976,** *26* (1), 123-132. https://doi.org/10.1016/0025-5416(76)90234-2

4. Olson, G. B.; Cohen, M., A general mechanism of martensitic nucleation: Part I. General concepts and the FCC → HCP transformation. *Metallurgical Transactions A* **1976,** *7* (12), 1897-1904. https://doi.org/10.1007/BF02659822

5. Bogers, A. J.; Burgers, W. G., Partial dislocations on the {110} planes in the B.C.C. lattice and the transition of the F.C.C. into the B.C.C. lattice. *Acta Metallurgica* **1964,** *12* (2), 255-261. https://doi.org/10.1016/0001-6160(64)90194-4

6. Olson, G. B.; Cohen, M., A general mechanism of martensitic nucleation: Part II. FCC → BCC and other martensitic transformations. *Metallurgical Transactions A* **1976,** *7* (12), 1905-1914. https://doi.org/10.1007/BF02659823

7. Olson, G. B.; Cohen, M., A general mechanism of martensitic nucleation: Part III. Kinetics of martensitic nucleation. *Metallurgical Transactions A* **1976,** *7* (12), 1915-1923. https://doi.org/10.1007/BF02659824

8.   Güden, M.; Yavaş, H.; Tanrıkulu, A. A.; Taşdemirci, A.; Akın, B.; Enser, S.; Karakuş, A.; Hamat, B. A., Orientation dependent tensile properties of a selective-laser-melt 316L stainless steel. *Materials Science and Engineering: A* **2021,** *824*, 141808. https://doi.org/10.1016/j.msea.2021.141808

9.   Hecker, S. S.; Stout, M. G.; Staudhammer, K. P.; Smith, J. L., Effects of Strain State and Strain Rate on Deformation-Induced Transformation in 304 Stainless Steel: Part I. Magnetic Measurements and Mechanical Behavior. *Metallurgical Transactions A* **1982,** *13* (4), 619-626. https://doi.org/10.1007/BF02644427

10.   Enser, S. The deformation rate sensitivities of additively and conventionally fabricated 316L alloys. Izmir Institute of Technology (Turkey), 2021.

11.   He, Y.; Gao, J.; He, Y.; Shin, K., The mechanisms of γ (fcc)→ ε (hcp)→ α′(bcc) and direct γ (fcc)→ α′(bcc) martensitic transformation in a gradient austenitic stainless steel. *Journal of Materials Science* **2022,** *57* (8), 5230-5240. https://doi.org/10.1007/s10853-022-06936-z

12.   Venables, J., The martensite transformation in stainless steel. *The Philosophical Magazine: A Journal of Theoretical Experimental and Applied Physics* **1962,** *7* (73), 35-44. https://doi.org/10.1080/14786436208201856

13.   De, A. K.; Murdock, D. C.; Mataya, M. C.; Speer, J. G.; Matlock, D. K., Quantitative measurement of deformation-induced martensite in 304 stainless steel by X-ray diffraction. *Scripta Materialia* **2004,** *50* (12), 1445-1449. https://doi.org/10.1016/j.scriptamat.2004.03.011

14.   Olson, G. B.; Cohen, M., Kinetics of strain-induced martensitic nucleation. *Metallurgical Transactions A* **1975,** *6* (4), 791-795.https://doi.org/10.1007/BF02672301

15. Murr, L.; Staudhammer, K.; Hecker, S., Effects of strain state and strain rate on deformation-induced transformation in 304 stainless steel: Part II. Microstructural study. *Metallurgical Transactions A* **1982,** *13*, 627-635. https://doi.org/10.1007/BF02644427

16. Ramirez, J. A. C.; Tsuta, T.; Mitani, Y.; Osakada, K., Flow stress and phase transformation analyses in the austenitic stainless steel under cold working: part 1, phase transformation characteristics and constitutive formulation by energetic criterion. *JSME international journal. Ser. 1, Solid mechanics, strength of materials* **1992,** *35* (2), 201-209. https://doi.org/10.1299/jsmea1988.35.2_201

17. Stringfellow, R.; Parks, D.; Olson, G., A constitutive model for transformation plasticity accompanying strain-induced martensitic transformations in metastable austenitic steels. *Acta metallurgica et materialia* **1992,** *40* (7), 1703-1716. https://doi.org/10.1016/0956-7151(92)90114-T

18. Tomita, Y.; Iwamoto, T., Constitutive modeling of TRIP steel and its application to the improvement of mechanical properties. *International Journal of Mechanical Sciences* **1995,** *37* (12), 1295-1305. https://doi.org/10.1016/0020-7403(95)00039-Z

19. Iwamoto, T.; Tsuta, T.; Tomita, Y., Investigation on deformation mode dependence of strain-induced martensitic transformation in trip steels and modelling of transformation kinetics. *International Journal of Mechanical Sciences* **1998,** *40* (2-3), 173-182. https://doi.org/10.1016/S0020-7403(97)00047-7

20. Diani, J.; Parks, D., Effects of strain state on the kinetics of strain-induced martensite in steels. *Journal of the Mechanics and Physics of Solids* **1998,** *46* (9), 1613-1635. https://doi.org/10.1016/S0022-5096(98)00001-5

21. Song, S.-c.; Gui-bao, D.; Zu-ping, D., Martensitic transformation under impact with high strain rate. *International journal of impact engineering* **2001,** *25* (8), 755-765. https://doi.org/10.1016/S0734-743X(01)00016-1

22.   Dan, W.; Zhang, W.; Li, S.; Lin, Z., A model for strain-induced martensitic transformation of TRIP steel with strain rate. *Computational Materials Science* **2007,** *40* (1), 101-107. https://doi.org/10.1016/j.commatsci.2006.11.006

23.   Lichtenfeld, J. A.; Van Tyne, C. J.; Mataya, M. C., Effect of strain rate on stress-strain behavior of alloy 309 and 304L austenitic stainless steel. *Metallurgical and Materials Transactions A* **2006,** *37*, 147-161. https://doi.org/10.1007/s11661-006-0160-5

24.   Talonen, J.; Hänninen, H., Formation of shear bands and strain-induced martensite during plastic deformation of metastable austenitic stainless steels. *Acta materialia* **2007,** *55* (18), 6108-6118. https://doi.org/10.1016/j.actamat.2007.07.015

25.   Rusinek, A.; Rodríguez-Martínez, J. A.; Pesci, R.; Capelle, J., Experimental characterisation and modelling of the thermo-viscoplastic behaviour of steel AISI 304 within wide ranges of strain rate at room temperature. **2010**.

26.   Yoo, S.-W.; Lee, C.-S.; Park, W.-S.; Kim, M.-H.; Lee, J.-M., Temperature and strain rate dependent constitutive model of TRIP steels for low-temperature applications. *Computational Materials Science* **2011,** *50* (7), 2014-2027. https://doi.org/10.1016/j.commatsci.2011.02.002

27.   Zaera, R.; Rodríguez-Martínez, J. A.; Casado, A.; Fernandez-Saez, J.; Rusinek, A.; Pesci, R., A constitutive model for analyzing martensite formation in austenitic steels deforming at high strain rates. *International Journal of Plasticity* **2012,** *29*, 77-101. https://doi.org/10.1016/j.ijplas.2011.08.003

28.   Peng, F.; Dong, X.-h.; Liu, K.; Xie, H.-y., Effects of strain rate and plastic work on martensitic transformation kinetics of austenitic stainless steel 304. *Journal of Iron and Steel Research International* **2015,** *22* (10), 931-936. https://doi.org/10.1016/S1006-706X(15)30092-3

29.   Jia, B.; Rusinek, A.; Pesci, R.; Bahi, S.; Bernier, R., Thermo-viscoplastic behavior of 304 austenitic stainless steel at various strain rates and temperatures: Testing, modeling and validation. *International Journal of Mechanical Sciences* **2020,** *170*, 105356. https://doi.org/10.1016/j.ijmecsci.2019.105356

30.   Song, B.; Sanborn, B., A modified Johnson–Cook model for dynamic response of metals with an explicit strain-and strain-rate-dependent adiabatic thermosoftening effect. *Journal of Dynamic Behavior of Materials* **2019,** *5*, 212-220. https://doi.org/10.1007/s40870-019-00203-0

31.   Jia, B.; Rusinek, A.; Pesci, R.; Bernier, R.; Bahi, S.; Bendarma, A.; Wood, P., Simple shear behavior and constitutive modeling of 304 stainless steel over a wide range of strain rates and temperatures. *International Journal of Impact Engineering* **2021,** *154*, 103896. https://doi.org/10.1016/j.ijimpeng.2021.103896

32.   Kishore, K.; Kumar, R. G.; Chandan, A. K., Critical assessment of the strain-rate dependent work hardening behaviour of AISI 304 stainless steel. *Materials Science and Engineering: A* **2021,** *803*, 140675. https://doi.org/10.1016/j.msea.2020.140675

33.   Li, L.; Wang, R.; Zhao, H.; Zhang, H.; Yan, R. In *Combined effects of elevated temperatures and high strain rates on compressive performance of S30408 austenitic stainless steel*, Structures, Elsevier: 2021; pp 1-9. https://doi.org/10.1016/j.istruc.2021.07.063

34.   Jia, B.; Zhang, Y.; Rusinek, A.; Xiao, X.; Chai, R.; Gu, G., Thermo-viscoplastic behavior and constitutive relations for 304 austenitic stainless steel over a wide range of strain rates covering quasi-static, medium, high and very high regimes. *International Journal of Impact Engineering* **2022,** *164*, 104208. https://doi.org/10.1016/j.ijimpeng.2022.104208

35. Seo, J.-M.; Jeong, S.-S.; Kim, Y.-J.; Kim, J.-W.; Oh, C.-Y.; Tokunaga, H.; Kumagai, T.; Miura, N., Modification of the Johnson–Cook model for the strain rate effect on tensile properties of 304/316 austenitic stainless steels. *Journal of Pressure Vessel Technology* **2022,** *144* (1), 011501. https://doi.org/10.1115/1.4050833

36. Johnson, G. R.; Cook, W. H., Fracture characteristics of three metals subjected to various strains, strain rates, temperatures and pressures. *Engineering fracture mechanics* **1985,** *21* (1), 31-48. https://doi.org/10.1016/0013-7944(85)90052-9

37. Hancock, J.; Mackenzie, A., On the mechanisms of ductile failure in high-strength steels subjected to multi-axial stress-states. *Journal of the Mechanics and Physics of Solids* **1976,** *24* (2-3), 147-160. https://doi.org/10.1016/0022-5096(76)90024-7

38. Gkolfinopoulos, I.; Chijiwa, N., Determination of Johnson–Cook material and failure model constants for high-tensile-strength tendon steel in post-tensioned concrete members. *Applied Sciences* **2022,** *12* (15), 7774. https://doi.org/10.3390/app12157774

39. Dey, S.; Børvik, T.; Hopperstad, O.; Langseth, M., On the influence of constitutive relation in projectile impact of steel plates. *International Journal of Impact Engineering* **2007,** *34* (3), 464-486. https://doi.org/10.1016/j.ijimpeng.2005.10.003

40. Cockcroft, M., Ductility and workability of metals. *J. of Metals* **1968,** *96*, 2444.

41. Johnson, G. R.; Holmquist, T. J., Response of boron carbide subjected to large strains, high strain rates, and high pressures. *Journal of applied physics* **1999,** *85* (12), 8060-8073. https://doi.org/10.1063/1.370643

42. Rao, C. L.; Narayanamurthy, V.; Simha, K., *Applied impact mechanics*. John Wiley & Sons: 2016.

43. ASTM Standard E8/E8M (2016) Standard test methods for tension testing of metallic materials.

44. Bridgman, P., The stress distribution at the neck of a tension specimen. *Trans. ASM* **1944,** *32*, 553-574.

45. Mirone, G.; Corallo, D., A local viewpoint for evaluating the influence of stress triaxiality and Lode angle on ductile failure and hardening. *International Journal of Plasticity* **2010,** *26* (3), 348-371. https://doi.org/10.1016/j.ijplas.2009.07.006

46. Mirone, G., Approximate model of the necking behaviour and application to the void growth prediction. *International Journal of Damage Mechanics* **2004,** *13* (3), 241-261. https://doi.org/10.1177/1056789504042592

47. Çakırcalı, M.; Kılıçaslan, C.; Güden, M.; Kıranlı, E.; Shchukin, V. Y.; Petronko, V. V., Cross wedge rolling of a Ti6Al4V (ELI) alloy: the experimental studies and the finite element simulation of the deformation and failure. *The International Journal of Advanced Manufacturing Technology* **2013,** *65*, 1273-1287. https://doi.org/10.1007/s00170-012-4256-3

48. Sarıkaya, M.; Güden, M.; Kambur, Ç.; Özbek, S. Ç.; Taşdemirci, A., Development of the Johnson-Cook flow stress and damage parameters for the impact response of polycarbonate: Experimental and numerical approach. *International Journal of Impact Engineering* **2023,** *179*, 104674. https://doi.org/10.1016/j.ijimpeng.2023.104674

49. Küçük, Y.; Çelik, B. K., KOMPOZİT ZIRH TASARIMI VE BALİSTİK DİRENCİNİN İNCELENMESİ. *Bartın University International Journal of Natural and Applied Sciences 6* (1), 12-20.

50. Flores-Johnson, E.; Saleh, M.; Edwards, L., Ballistic performance of multi-layered metallic plates impacted by a 7.62-mm APM2 projectile. *International Journal of Impact Engineering* **2011,** *38* (12), 1022-1032. https://doi.org/10.1016/j.ijimpeng.2011.08.005

51.   Holmquist, T.; Johnson, G., Response of boron carbide subjected to high-velocity impact. *International Journal of Impact Engineering* **2008,** *35* (8), 742-752. https://doi.org/10.1016/j.ijimpeng.2007.08.003